

Numerical and Observational Study of Stealth and Consecutive Coronal Mass Ejections

Dana-Camelia Tălpeanu

Supervisors:
Prof. dr. Stefaan Poedts
Dr. Elke D'Huys
(Royal Observatory of Belgium)

Dissertation presented in partial
fulfillment of the requirements for the
degree of Doctor of Science (PhD):
Mathematics

June 2022

Numerical and Observational Study of Stealth and Consecutive Coronal Mass Ejections

Dana-Camelia TĂLPEANU

Examination committee:

Prof. dr. Wim Schoutens, chair

Prof. dr. Stefaan Poedts, supervisor

Dr. Elke D’Huys, supervisor

(Royal Observatory of Belgium)

Prof. dr. Jasmina Magdalenic Zhukov

Prof. dr. Jon O. Sundqvist

Prof. dr. Tom Van Doorselaere

Dr. Marilena Mierla

(Royal Observatory of Belgium; Institute of Geodynamics of the Romanian Academy)

Dr. Ian G. Richardson

(University of Maryland; NASA)

Dissertation presented in partial fulfillment of the requirements for the degree of Doctor of Science (PhD): Mathematics

June 2022

© 2022 KU Leuven – Faculty of Science
Uitgegeven in eigen beheer, Dana-Camelia Tălpeanu, Celestijnenlaan 200B, B-3001 Leuven (Belgium)

Alle rechten voorbehouden. Niets uit deze uitgave mag worden vermenigvuldigd en/of openbaar gemaakt worden door middel van druk, fotokopie, microfilm, elektronisch of op welke andere wijze ook zonder voorafgaande schriftelijke toestemming van de uitgever.

All rights reserved. No part of the publication may be reproduced in any form by print, photoprint, microfilm, electronic or any other means without written permission from the publisher.

Preface

These past five years have been an amazing journey, difficult, but extremely rewarding and one that helped me grow and evolve, scientifically and personally. I managed to reach the end of it thanks to many people that helped me throughout the process, either directly work-related, or with a small chat and an evening of boardgames.

First of all, I would like to thank my promoter, prof. Stefaan Poedts, for taking me as a PhD student and for believing in me and in my judgment, that helped form the independent scientist I am today. I also have immense gratitude for my supervisor, Elke D’Huys, who was always there for me and listened to my rants patiently and giving me advice, but also pushing me to be a better researcher and a better person. Your support was, and still is, invaluable! I am extremely grateful to Marilena Mierla, who contacted me about the PhD position and without whom I would not be where I am now. She taught me about CME reconstructions and incredible patience (I still don’t know how you manage this), but also helped me with IDL and chats whenever I needed it. I truly admire you! Many thanks to Ian Richardson, who jumped in to the rescue as my assessor in the final year, and critically read my manuscripts and provided valuable corrections and comments. You’re an incredible scientist, and an amazing person, I will strive to be like you!

Even though they are not on the thesis, Francesco Zuccarello, Emmanuel Chané and Ilia Roussev helped me tremendously by initiating me into the code at the time when I needed it most, advising with the analysis and giving indispensable suggestions.

Jenny and Emil... I cannot thank you enough for all you’ve done. You were always there for me when things took a bad turn, but also in all the good times, from the first cooking evenings, to boardgames, trips and many more. Thank you from the bottom of my heart and I love you guys. Matt... come back, we miss you!

Being a joint PhD project, I had the chance of working with two amazing groups of people, at CmPA and ROB. It was always fun to interact with the other PhD students at KU Leuven, especially during Briscola lunches in the aquarium with Dimis, Kostas, Skralan, Jo, Camilla, Bieke&Brecht, Christine, Lia, Norbert, and many others. Extra thanks to Nicolas for the fun chats, but also for all the help with occasional equation issues. To my sweet old wizard Julia (aka Elza), arigato gozaimasu! You introduced me to the wonderful world of DnD and I am grateful for that. To many more campaigns!

When it comes to ROB people, I should thank the entire department of solar physics, whom I annoyed with countless questions! It was always a pleasure to nerd out about Japanese culture and anime with you, Alexandros! Chris (or Immanuel?), thanks for delighting us with delicious Indian food and chats. Dina&Lawrence, I am so happy you came to the observatory, you're awesome people! Koen, I can never get enough of talking to you and trying to uncover whether you're saying things seriously or joking, I have learned from you the art of sarcasm! Many thanks to Sarah and Marie for introducing me to climbing, which I am loving, especially the after-drinks, now also with Manu and Judith. I am grateful to literally everyone at ROB who made me feel welcomed and at home, especially Laurent (for boardgames and pancakes!), Thanassis, Jan, Christophe (also for keeping my plants alive!), Cis (for the lovely meteor chats), David, Hilde, Olivier (both), Sergei, Fabian, and many many others! And especially, Anne, we will always remember your kind, giving and helpful nature and you will forever be in our hearts.

Leaving Romania was not easy, and bits of me are still there left with my childhood friends, Costin, Ionut and Alex, with whom I hope to do many more mountains hikes and Perseids observations. The discussions about philosophy, books, movies, and any random things that come to mind were heart-warming and made me feel back home. Many thanks to my first ever boss, Diana, who became my dear friend and listened to me whenever I needed a chat.

And of course, my sweet Stijn. Climbing brought us together and actually the pandemic kept us unseparated for almost two years now. I love living, playing boardgames, going on trips, cooking and hiking with you, basically doing everything with you. Thank you for all the support and love you've given me, especially in my extra-annoying times. I hope we visit the world together!

Lastly, a little message for the people I love most in the world, my parents, who were there for me all these years: Va pup, va iubesc enorm si va multumesc pentru tot sprijinul acordat in acesti ani dificili, departe de voi. Sunteti cei mai importanti oameni pentru mine si am avut si o sa am nevoie de voi intotdeauna.

Thank you all! ♥

Abstract

The Sun has a profound influence on our planet, not only through the day/night cycle, but also through its activity, which is strongly related to coronal mass ejections (CMEs). They are massive blowouts of solar plasma and magnetic field that may reach Earth and produce perturbations of our planet's magnetic field (geomagnetic storms), affecting electrical systems, radio communications, satellites and the health of astronauts. One way of mitigating the risks to human health and infrastructure is by forecasting the arrival of these CMEs at Earth. The forecast can improve by a more profound understanding of how CMEs are triggered, how they erupt and propagate into interplanetary space, and how they interact and change during their journey away from the Sun.

There are some particular classes of eruptions that already make this forecast more difficult. The decision whether a CME is headed towards or away from Earth is based on its source location on the Sun, which is indicated by solar features associated with the CME, usually seen shortly before or after its expulsion. If those are not present on the visible side of the Sun, the CME is assumed to erupt from the back side of the Sun, as seen from Earth, and propagate away from Earth, and thus is excluded from forecasting. This well defined criterion can be misleading in the case of 'stealth' CMEs, which lack these usual signatures, and can therefore trigger a geomagnetic storm without them even being considered as possible candidates. The forecast of a potential upcoming geomagnetic storm is challenging also in the case of consecutive CMEs, which erupt in close time spans one after the other. If multiple CMEs are directed towards Earth, they are prone to interact with each other and with the environment, changing their structure significantly and making their effect on our planet challenging to predict.

This study aims to combine observational and numerical methods to investigate stealth and consecutive CMEs and determine the processes that trigger them. We analyze their evolution during propagation in interplanetary space and their geomagnetic effects, in order to improve the forecast.

The manuscript begins with an introduction to the solar-terrestrial environment in Chapter 1, describing the structure of the Sun, coronal mass ejections and the ways in which they affect our planet. Chapter 2 gives an overview of the numerical methods used to simulate CMEs and the theory that lies at their foundation. We present the MPI-AMRVAC code we use in our simulations, as well as the basis for the analysis of forces performed on them.

We begin our study in Chapter 3 where we numerically investigate the influence of different triggering motions on the initiation of two consecutive CMEs. We find that changes within 1% in the shearing speed result in three different scenarios for the second CME, although the preceding eruption seems unaffected by such small variations. We thus obtain as second ejection a failed eruption, a stealth ejecta, or a CME driven by the imposed shear. We also compare all simulated eruptions with an observed event and achieve a good correlation for two of the cases (with a stealth and without). Lastly, we use Poynting flux analysis to reveal the temporal variation of the important eruption.

In Chapter 4 we simulate the CMEs propagating into a faster background solar wind as compared to that presented in Chapter 3, which is a slow wind. In the cases of Chapter 3, plasma blobs arise in the trail of eruptions, but not in the faster wind. The two previously mentioned cases (one with a stealth and one without) also fit the observed event at 1 AU, highlighting the important contribution of the interactions CMEs are subjected to during their propagation in the interplanetary space. We also calculate the *Dst* index of the simulated eruptions, which is a good indication of their effect on Earth. The *Dst* computation results in a reduced geoeffectiveness in the case of consecutive CMEs when the flux ropes arrive with a leading positive B_z . When B_z is reversed, the geoeffectiveness increases, meaning that the magnetic reconnections with the trailing blobs and eruptions strongly affect the impact of the arriving interplanetary CME.

Chapter 5 provides a thorough analysis of the forces governing the dynamics of the previously simulated eruptions. We explain the formation of the stealth ejecta and of the plasma blobs occurring in the aftermath of solar eruptions. We also address the dynamical differences between two CMEs obtained through the same triggering boundary motions, which we attribute to the slightly modified magnetic configuration obtained by changing the background solar wind. The thermal pressure gradient revealed a shock in front of all these slow eruptions, formed during their propagation to 1 AU. A double peaked magnetic pressure gradient indicates that the triggering method affects the structure of the CMEs, and that a part of the adjacent coronal structure is ejected along with the CME.

Finally, in Chapter 6 we present some concluding remarks and a summary of the results obtained in this thesis.

Beknopte samenvatting

De zon heeft een diepgaande invloed op onze planeet, niet alleen via de dag/nacht cyclus, maar ook door haar activiteit, die sterk samenhangt met coronale massa-uitbarstingen (CMEs). Dat zijn enorme wolken van zonneplasma en magnetisch veld die de aarde kunnen bereiken en haar magnetische veld verstoren (geomagnetische stormen), met impact op elektrische systemen, radiocommunicatie, satellieten en de gezondheid van astronauten. De risico's voor onze gezondheid en infrastructuur kunnen we beperken door de aankomst van CMEs te voorspellen. Deze voorspellingen kunnen verbeteren door een diepgaander begrip van hoe CMEs ontstaan, uitbarsten en zich voortbewegen door de interplanetaire ruimte, en hoe ze met elkaar interageren en veranderen op hun reis weg van de zon.

Speciale uitbarstingen maken de voorspellingen nog moeilijker. Uitmaken of een CME naar de aarde toe of ervan weg beweegt, is gebaseerd op de locatie waar hij ontstaat, bepaald door waarnemingen van zonneactiviteit gelinkt aan de CME, kort voor of na de uitbarsting. Zonder tekenen aan de zichtbare kant van de zon, wordt aangenomen dat de CME aan de achterkant is uitgebarsten, zich wegbeweegt van de aarde, en dus niet moet worden opgenomen in de voorspellingen. Dit duidelijk criterium kan misleidend zijn in het geval van 'stealth' CMEs, waar deze tekenen op het zonsoppervlak ontbreken, en die zo een geo-magnetische storm kunnen ontketenen terwijl ze daar niet eens voor in aanmerking lijken te komen. Het voorspellen van een geo-magnetische storm is ook uitdagend in het geval van CMEs die elkaar in een korte tijdsspanne opvolgen. Indien meerdere CMEs richting aarde gaan, is het waarschijnlijk dat ze met elkaar en hun omgeving interageren, waardoor hun structuur grondig kan wijzigen en hun effect op onze planeet moeilijk te voorspellen valt.

Dit onderzoek combineert observationele en numerieke methodes om stealth en opeenvolgende CMEs te bestuderen en de processen te bepalen die een uitbarsting op gang brengen. We analyseren hun evolutie terwijl ze door de interplanetaire ruimte razen alsook hun geo-magnetische effecten, om zo de voorspellingen te verbeteren.

Na een inleiding op het systeem zon-aarde in Hoofdstuk 1 - waarin de structuur van de zon, CMEs en hun invloed op aarde aan bod komen -, beschrijft Hoofdstuk 2 numerieke methodes waarmee we CMEs modelleren en de theorie aan de basis ervan. We stellen de MPI-AMRVAC code voor die we gebruiken voor onze simulaties, en ook de theorie van de krachtenanalyse die we erop uitvoerden.

In Hoofdstuk 3 onderzoeken we eerst numeriek de invloed van verschillende bewegingen op het uitlokken van twee opeenvolgende CMEs. We vinden dat variaties binnen 1% van de snelheid van de schuivende bewegingen, drie verschillende scenario's voor de tweede CME opleveren, ook al lijkt de eerste ongevoelig voor deze kleine verandering. We bekomen zo als tweede CME een mislukte uitbarsting, een stealth ejecta, of een CME aangedreven door de opgelegde schuifbeweging. We vergelijken ook alle gemodelleerde CMEs met een waargenomen uitbarsting en vinden een goede correlatie voor twee van de gevallen (met een stealth, en zonder). In een laatste stap analyseren we via de Poynting flux de tijdsvariatie van de belangrijkste fases van de uitbarstingen.

In Hoofdstuk 4 simuleren we de CMEs terwijl ze door een snellere zonnwind dan in Hoofdstuk 3 razen. In de scenario's van Hoofdstuk 3 vormen zich plasma-ophopingen in het kielzog van de CMEs, maar niet bij de snellere wind. De scenario's met en zonder stealth stemmen ook overeen met de waargenomen CME op een afstand van 1 AU, wat het belang benadrukt van de interacties die CMEs ondergaan tijdens hun reis door de interplanetaire ruimte. We berekenen ook de *Dst* index van de gesimuleerde CMEs, een maatstaf voor hun effect op aarde. De *Dst* toont verminderde geo-magnetische effecten bij opeenvolgende CMEs wanneer de magnetische structuur toekomt met een positieve B_z vooraan. Wanneer we het teken van B_z omdraaien, nemen de geo-magnetische effecten toe, wat toont dat de magnetische reconfiguratie met de achtervolgende plasma-ophopingen en uitbarstingen een sterke invloed heeft op de impact van interplanetaire CMEs.

Hoofdstuk 5 brengt een doorgedreven analyse van de krachten die de dynamica van de gesimuleerde CMEs beheersen. We verklaren hoe stealth ejecta en plasma-ophopingen in het kielzog van CMEs ontstaan. We illustreren ook de verschillende dynamica van twee CMEs, aangedreven door identieke bewegingen, aan de hand van hun iets andere magnetische configuratie die werd bekomen door de zonnwind in de achtergrond te wijzigen. De gradiënt van de thermische druk vertoont een schok aan de voorkant van al deze trage CMEs op weg naar 1 AU. Een dubbele piek in de gradient van de magnetische druk wijst erop dat de manier van ontstaan de structuur van de CME beïnvloedt, en dat een deel van de naburige coronaal structuur samen met de CME is uitgebarsten.

We eindigen in Hoofdstuk 6 met afsluitende opmerkingen en een samenvatting van de resultaten van deze thesis.

Contents

Abstract	iii
Beknopte samenvatting	v
Contents	vii
List of Abbreviations	ix
1 Introduction to the Sun-Earth system	1
1.1 Structure of the Sun	2
1.1.1 Solar interior	2
1.1.2 Solar atmosphere	4
1.1.3 Solar wind	10
1.2 Coronal mass ejections and associated phenomena	15
1.2.1 Definition and description	15
1.2.2 Spacecraft observing the Sun and CMEs	18
1.2.3 CME eruption mechanisms	21
1.2.4 Stealth coronal mass ejections	28
1.2.5 Interplanetary coronal mass ejections	31
1.3 Space weather and geo-effectiveness	33
1.4 Motivation and thesis goals	38
2 CME modeling	40
2.1 Introduction to plasma physics	40
2.2 Ideal magnetohydrodynamics theory	42
2.3 Forces governing the dynamics of CMEs	45
2.4 MPI-AMRVAC code	47
3 Numerical simulations of shear-induced consecutive CMEs	51
3.1 Introduction	52
3.2 Observations	54

3.3	Simulations set-up and method	61
3.4	Results	65
3.5	Analysis of the simulations	70
3.6	Summary	74
4	Study of the propagation, in situ signatures, and geoeffectiveness of shear-induced CMEs in different solar winds	77
4.1	Introduction	78
4.2	Observations	80
4.3	Numerical MHD code and methods	80
4.4	Simulated eruptions and solar winds	83
4.5	Comparison with in situ signatures	93
4.6	Geoeffectiveness	102
4.7	Summary and Discussion	108
5	Interaction of coronal mass ejections and the solar wind. A force analysis	111
5.1	Introduction	112
5.2	Numerical MHD code, methods and simulations	114
	5.2.1 Numerical setup	114
	5.2.2 Simulated eruptions	114
5.3	Force analysis	115
	5.3.1 Different CME eruption times for the two background solar winds	116
	5.3.2 Formation of the stealth ejecta	120
	5.3.3 Formation of plasma blobs	123
	5.3.4 Propagation and interaction of CMEs	127
5.4	Summary	135
6	Conclusions	137
	Bibliography	143
	Curriculum Vitae	157

List of Abbreviations

<i>Dst</i>	Disturbance storm time
AIA	Atmospheric Imaging Assembly
AMR	Adaptive Mesh Refinement
AR	Active Region
AU	Astronomical Unit
CFL	Courant-Friedrichs-Lewy
CME	Coronal Mass Ejection
DKIST	Daniel K. Inouye Solar Telescope
EIT	Extreme-ultraviolet Imaging Telescope
ESA	European Space Agency
EUV	Extreme UltraViolet
EUVI	Extreme UltraViolet Imager
FR	Flux Rope
GCS	Graduated Cylindrical Shell
GLM	Generalised Lagrange Multiplier
GSM	Geocentric Solar Magnetospheric
HCS	Heliospheric Current Sheet
HMI	Helioseismic and Magnetic Imager

ICME	Interplanetary Coronal Mass Ejection
IMF	Interplanetary Magnetic Field
IPS	InterPlanetary Scintillation
LYRA	Large Yield Radiometer
MCME	Multiple Coronal Mass Ejection
MHD	Magnetohydrodynamics
MPI	Message Passing Interface
MPI-AMRVAC	Message Passing Interface - Adaptive Mesh Refinement - Versatile Advection Code
NASA	National Aeronautics and Space Administration
PFSS	Potential Field Source Surface
PIL	Polarity Inversion Line
PROBA2	Project for Onboard Autonomy 2
PSP	Parker Solar Probe
SDO	Solar Dynamics Observatory
SECCHI	Sun Earth Connection Coronal and Heliospheric Investigation
SEP	Solar Energetic Particle
SOHO	Solar and Heliospheric Observatory
Solo	SOLar Orbiter
SSC	Storm Sudden Commencement
SSN	SunSpot Number
SSW	SolarSoftWare
STCE	Solar-Terrestrial Centre of Excellence
STEREO	Solar TERrestrial RELations Observatory
SWAP	Sun Watcher with Active Pixels and Image Processing
SWOOPS	Solar Wind Observations Over the Poles of the Sun
TVDLF	Total Variation Diminishing Lax-Friedrichs

VAC Versatile Advection Code

Chapter 1

Introduction to the Sun-Earth system

*“I must not fear.
Fear is the mind-killer.
Fear is the little-death that brings total obliteration.
I will face my fear.
I will permit it to pass over me and through me.
And when it has gone past
I will turn the inner eye to see its path.
Where the fear has gone there will be nothing.
Only I will remain.”*
– Bene Gesserit Litany Against Fear, Dune

Summary

This Chapter provides an introduction to the solar-terrestrial environment and the key concepts lying at its basis. We begin our journey with a description of the Sun and its structure, from the interior all the way to its atmosphere in the interplanetary space and the solar wind. We continue by presenting the important solar transients that erupt from the Sun and travel through the solar wind medium, called coronal mass ejections. Their drivers, formation of the associated flux rope, eruption and propagation are discussed, as well as their potential effects on Earth’s magnetosphere and on our infrastructure.

1.1 Structure of the Sun

The Sun is the star that lies in one of the focal points of our planet's orbit, not only fueling life, but making it thrive. Despite being the only known star with critters running around it, it is a rather common and average G2V-type star, close to the middle of the main sequence of the Hertzsprung–Russell diagram. This location also implies that the Sun has an absolute magnitude of 4.74 (apparent magnitude of -26.7), and a surface temperature of 5778 ± 3 K (Stix 2002). Considered a yellow dwarf due to its dominant emission in the visible spectrum, it has a mean density of 1.408 g cm^{-3} and a mass of $M_{\odot} = 1.9889 \pm 0.0003 \times 10^{30}$ kg, accounting for 99.86% of the mass of the solar system. The Sun also has a radius of $R_{\odot} = 6.957 \times 10^8$ m, which is 109 times larger than that of Earth. The mean distance to our planet is 149597870 ± 2 km or one Astronomical Unit (AU), taking light approximately 8.3 min to reach us (e.g. Stix 2002; Cox 2002).

The non-solid nature of the Sun imposes uneven rotational periods depending on the latitude. The equator takes 25 days to make a full rotation, while the poles rotate slower, over 35 days. This fluid property is called differential rotation.

Our star is composed of two main regions, the interior and the atmosphere, which will be described in more detail in the following subsections.

1.1.1 Solar interior

Inside this giant yellow, almost perfect ball of plasma, there is a three-layer structure, starting from the center: the *core*, the *radiative zone*, and the *convection zone* (Figure 1.1).

The light that takes a few minutes to reach our planet once it escapes the Sun is created inside the core, where thermonuclear fusion takes place. Here, the extreme temperature (15 million K) and density (151 g cm^{-3}) combine hydrogen nuclei (protons) into helium, releasing massive amounts of energy in the process, in the form of gamma rays, positrons, neutrinos and kinetic energy. Even though this mechanism burns up the Sun's hydrogen, which now represents 92% of the solar mass, it is still expected to have enough fuel for ~ 5 more billion years, until its full exhaustion. The high-energy radiation (gamma rays) is transported outwards through the next layer, the *radiative zone*, which extends from $0.25 R_{\odot}$ to $0.7 R_{\odot}$. The high density of this zone makes the radiation created in the core follow a 'drunkard's walk' ('random walk'), hitting the surrounding medium and changing direction every centimeter, or even less. In this process,

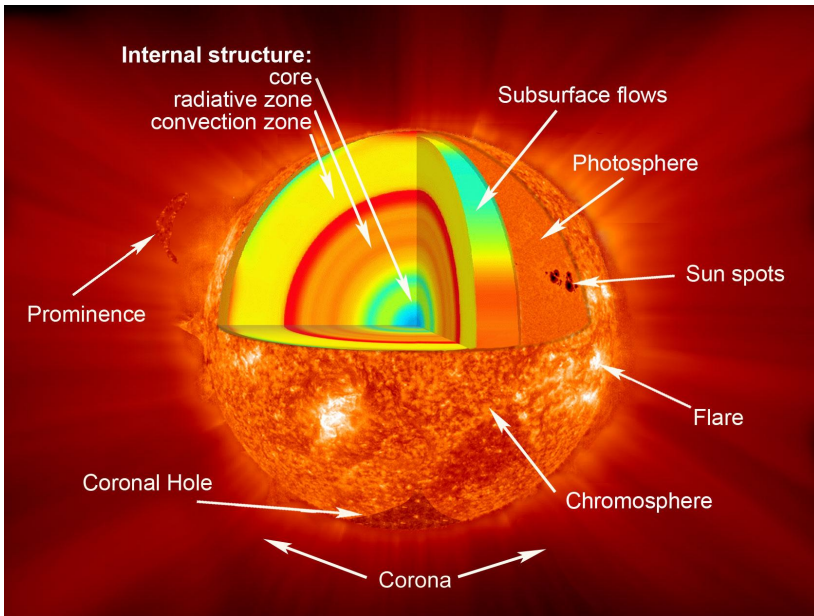


Figure 1.1: The solar structure (interior and atmosphere) from the core to the corona. Credits: National Aeronautics and Space Administration (NASA).

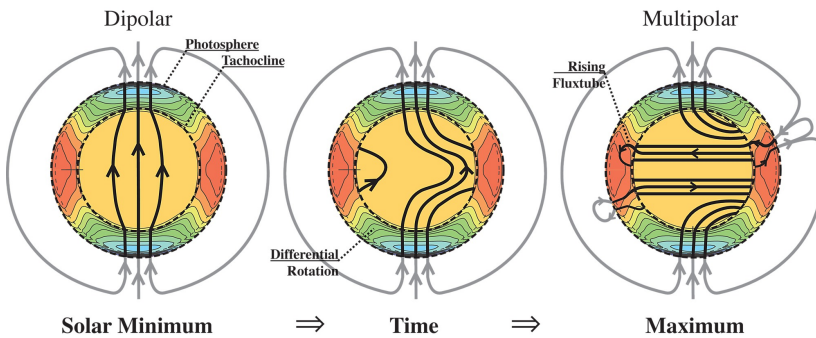


Figure 1.2: Diagram of the evolution in time of the Sun's magnetic field due to the solar dynamo. It evolves from poloidal field during solar minimum (left panel) to multipolar toroidal field during solar maximum (right panel). Credits: Higgins (2012).

the gamma rays created in the core are absorbed by the surrounding atoms and re-emitted, transforming into lower-energy photons.

The thin spherical shell between the radiative zone and the convection zone is called the *tachocline*, where the energy transport method switches due to the sudden drop in density and temperature. Intuitively, the dominant process in this final layer of the solar interior becomes convection, as opposed to radiation in the deeper layers of the Sun. Within the last $0.3 R_{\odot}$, the convection zone cools down from a few million K to $\sim 6000\text{K}$ at the surface of the Sun. The hot plasma at the bottom of this layer becomes buoyant and rises to the surface, where it decreases its temperature. As it cools down, it becomes denser and begins to descend towards the bottom of the layer. The process is repeated, creating convection cells and transporting the energy to the surface. The top of these convection cells can be observed on the Sun's surface and are called *granules*. They usually have a diameter of about 1500 km and can last from 8 to 20 minutes before dissipating. The grainy appearance of the Sun provides a solid confirmation of the fact that these convective motions do take place in the outer layer of the Sun. The 8 minute journey of the photons towards our planet can finally begin, almost 1 million years after their creation in the core of the Sun, due to their random walk inside the Sun.

These convective motions in combination with the differential rotation comprise the solar dynamo, which is the currently accepted model for the physical process that creates the Sun's magnetic field. Initially, a bipolar poloidal field is created, just like that of a magnet, and this configuration roughly represents the magnetic structure of the Sun depicted at minimum of solar activity (left panel of Figure 1.2). Over time, the faster rotating equator drags the magnetic field with it, twisting it and creating at maximum of solar activity the multipolar structure seen in the right panel of Figure 1.2. This toroidal magnetic field continues to reconfigure and to create local dipoles, until the polarity of the pole in one hemisphere is no longer dominant. This leads to a global switch of the magnetic polarity, as well as a relaxation to the initial poloidal configuration. One of these polarity reversals defines the 11-year solar activity cycle, and two of them form a full magnetic cycle of the Sun.

1.1.2 Solar atmosphere

The solar atmosphere consists of four very different layers (Figure 1.1): the *photosphere*, the *chromosphere*, the *transition region* (the location varies and is therefore not shown in the figure) and the *corona*, starting from the visible surface of the Sun. The main differences lie in two physical properties, temperature and density, as seen in Figure 1.3.

The first and the only visible layer of the solar atmosphere in white-light is the photosphere (left panel of Figure 1.4). It represents the surface of the Sun because of its opacity that blocks the solar interior from view, and it is only ~ 400 km thick. The dark areas seen on the disk of the Sun on the left panel of Figure 1.4 are called *sunspots*, and are regions where strong magnetic field emerges on the solar surface. This inhibits the convective process, preventing hot plasma to rise and keeping the top part cooler (~ 4500 K), which is why sunspots look darker in comparison with the rest of the photosphere. The number of sunspots is also strongly correlated with the solar activity cycle, since they lie at the base of large loops of strong magnetic field that, taken as an entire system, create *active regions* (ARs, see below). The loops emerging from the convection zone are bipolar (right panel of Figure 1.2), therefore sunspots usually appear in pairs of two, carrying a north and a south magnetic pole respectively, similar to a bar magnet. This is, of course, the simplest magnetic configuration, but other more complicated ones are also present and quite frequently encountered, especially during maximum of solar activity.

The sunspot number (SSN, Clette & Lefèvre 2016) is defined as $k(10 \times G + S)$, with G being the number of sunspot groups, and S the number of individual sunspots. The variable k is a factor that accounts for differences that occur due to the observations being made by different persons or with different instrumentation and in varying atmospheric conditions. The sunspot number was initially introduced by Rudolf Wolf in 1848 (Wolf 1848), and his original measurements are archived in the database of the heritage group of the Swiss Rudolf Wolf Society ¹. Currently, the international sunspot number is recorded and provided by the World Data Center for the International Sunspot Number, located at the Royal Observatory of Belgium ².

The temperature increases slowly in the next layer of the solar atmosphere from ~ 6000 K at the edge of the photosphere, to about 20 000 K at the top of the *chromosphere*. Because the density continues to drop, as seen in Figure 1.3, this layer is very faint, almost transparent. Thus, it can only be seen during total solar eclipses when the Moon blocks the huge amount of photospheric light or with special filters. Then it appears as a red narrow band around the Sun, hence its name (from Ancient Greek, ‘ball of color’). Some features and phenomena observed in this layer are *filaments*, *prominences*, *plages* and *flares*. Prominences are structures that can be observed as huge arches rising above the solar disk and are made of cool and dense plasma, an example being shown in the top right edge of the Sun in Figure 1.4 (middle panel). Filaments and prominences represent the same phenomena, the difference being solely visual. If the background on which they are projected is the solar disk, they are labeled

¹<https://www.wolfinstitute.ch/>

²<https://www.sidc.be/silso/>

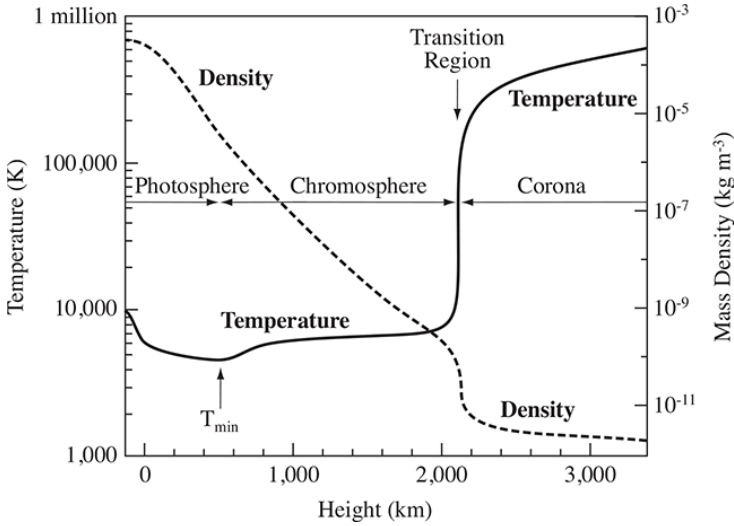


Figure 1.3: Schematic of the mean temperature and density variation with the increasing height above the solar surface, simulated with the Vernazza-Avrett-Loeser model (Vernazza et al. 1981). Credits: Priest (2014).

filaments and they are seen through absorption. If they are projected off-limb, they are called prominences and are seen in emission. Filaments are seen as long, thin and dark threads, and one of them is visible to the right of the center of the Sun in the middle panel of Figure 1.4. They usually lie at the boundary between two large regions of opposite magnetic polarity, called a *neutral line*. Filaments and prominences can remain in a quiet state for days or even weeks, but if the equilibrium is broken, they can erupt over the course of minutes or hours.

The *transition region* is located between the relatively cool chromosphere and the very hot corona and is an extremely thin layer. This region exhibits sudden changes in temperature and density, as seen in Figure 1.3, but it is also a highly dynamic and non-uniform layer. Going outwards, the density decreases continuously through the photosphere and the chromosphere, while the temperature first drops then rises again. In the transition region, on the other hand, the density drops suddenly and the temperature rises abruptly from the 20 000 K of the chromosphere up to the several millions K of the corona. The light emitted by this region is in ultraviolet, which can be seen only from outside Earth's atmosphere, because it is absorbed by the ozone, water vapors, oxygen and carbon dioxide in our atmosphere.

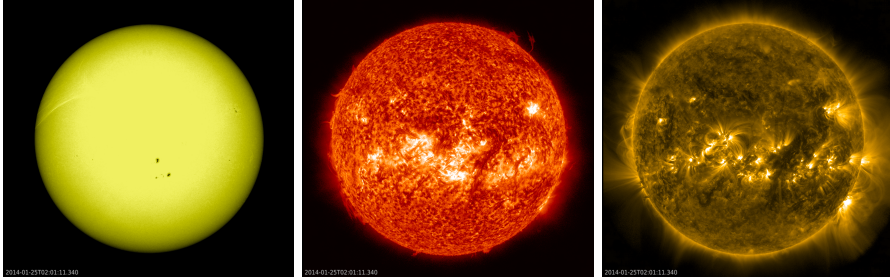


Figure 1.4: Observations of the solar atmosphere taken on 25 January 2014 by the Atmospheric Imaging Assembly (AIA) instrument onboard Solar Dynamics Observatory (SDO). The imaged layers of the solar atmosphere are the following, from left to right: photosphere (4500 \AA , 6000 K), chromosphere (304 \AA , 50 000 K), and quiet corona (171 \AA , 1 million K).

The solar *corona* (Latin for ‘crown’) is the fourth and final layer of the solar atmosphere, the hottest, and because of this, it is also the most intriguing and controversial. The temperature of this region can vary from one to two million K and can even reach temperatures of 10 million Kelvin in ARs. This layer is dominated in the lower regions by the magnetic field and the plasma is frozen to the field lines, and not the other way around as will be discussed later on. The white light corona can be seen during total solar eclipses or by using an instrument called a coronagraph, which blocks the photospheric light, enabling us to see the much fainter corona. The coronagraph was invented in 1930 and ever since we can observe the corona without the need of an eclipse (Lyot 1939). During the 11 years solar activity cycle, the appearance and the structure of the corona change drastically. At minimum of solar activity (left panel, Figure 1.5), when the number of sunspots is small, the corona has an organized plasma structure that reflects the magnetic field configuration. There are numerous radial open structures over the poles and loops at low latitudes below a denser ‘streamer belt’, which is stretched along the equator. On the other hand, at maximum solar activity (right panel, Figure 1.5), this atmospheric layer presents multiple streamers and lack of clear regions of open field over the poles.

The search for the explanation of the high coronal temperature led the scientific community to propose two main classes of mechanisms. The first involves magnetic waves formed in the highly turbulent convection zone. As they propagate outwards, they get damped and transfer their energy to the environment (the corona) by heating it. The second mechanism is *magnetic reconnection* in a multitude of current sheets. The notion of magnetic reconnection was initially introduced by Peter Alan Sweet in 1958 as a process which facilitates the release of magnetic energy through changes in field

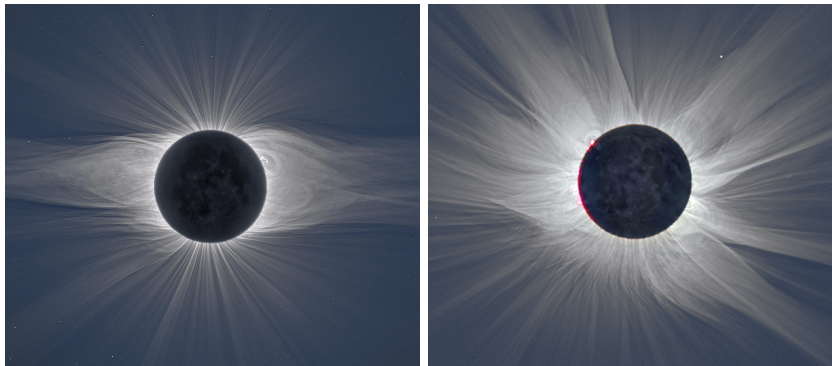


Figure 1.5: Photographs of the solar corona and of the Moon during total solar eclipses, on 2 July 2019 (solar minimum, left panel) and on 20 March 2015 (solar maximum, right panel). The polar plasma captured in the nearly radial magnetic field can be clearly seen in the left panel (*polar plumes*), as well as the *equatorial streamer belts*, due to the neatly organized solar corona. Credits: M. Druckmüller and P. Aniol. On the right side, the corona is omnidirectional and not as structured around poles and equator. Several prominences can be seen in the top left corner, just outside the edge of the Moon. Credits: M. Druckmüller, S. Habbal, P. Aniol and P. Štarha.

connectivity (Sweet 1958). When two regions of oppositely oriented magnetic field are pushed together, the nearly parallel field lines break and recombine with their counterparts at so called *X-type null points*, or simply *X-points* (where the magnetic field is approximately zero). Magnetic energy is converted into kinetic and thermal energy, accelerating plasma in the perpendicular direction to the original motion of the field lines and heating up the ambient solar atmosphere. These are just two of the suggested mechanisms, but a comprehensive list of coronal heating theories has been compiled by Cranmer & Winebarger (2019).

The solar corona has three components:

- K corona (Continuum corona, white-light) – it is caused by scattering of the light emitted in the photosphere by free electrons in the corona (Thomson scattering); there is a strong correlation between the structure of the K corona and the magnetic field of the Sun, therefore this component of the layer differs with the change of solar activity (Stix 2002). It is dominant within $2.3 R_{\odot}$, and its intensity is proportional to the electron density (Priest 2014);
- F corona (Fraunhofer corona, white-light) – it is caused by the scattering of the sunlight on dust particles in space and it dominates the white-light

signal beyond $2.5 R_{\odot}$;

- E corona (Emission corona) – it spans a very wide spectrum (from radio waves to X-rays) and it is composed of solar corona emission lines.

Coronal holes, coronal loops, coronal streamers, active regions, and coronal mass ejections represent some of the most important features observed in this extremely hot layer.

Coronal holes (seen at the South pole in Figure 1.1) are among the most ‘quiet’ regions of the Sun and also the darkest, being cooler (‘only’ 1 million K, Cox 2002) and less dense than the ambient corona. They are correlated with the expanding open magnetic field lines and they represent the commonly accepted origin of the *fast solar wind* (Subsection 1.1.3). The magnetic field in coronal holes is usually unipolar and more uniform than in other solar regions. Their size, number and location vary depending on the solar cycle (Cranmer 2009). During solar minimum, they are larger and mostly located in polar regions due to the well organized bipolar structure of the Sun. At maximum solar activity they are found mainly at lower latitudes, and a recent study of their evolution over three solar cycles showed that they also exhibit differential rotation, contrary to their previously observed rigid rotation (Hewins et al. 2020).

Active regions represent the extended magnetic field structures from the photosphere up to the corona, emitting in a wide variety of wavelengths from γ -rays to radio. They are usually associated with strong magnetic flux (kG) and can be seen as the coronal counterpart to sunspots (e.g., van Driel-Gesztelyi & Green 2015). Active regions are hotter than the surrounding corona and they have a high concentration of magnetic field, with large amounts of stored magnetic energy created from shearing motions and flux emergence. In the photosphere, the manifestations of ARs and therefore of strong magnetic field are represented by sunspots. Going up into the chromosphere, the evidence of ARs are bright areas called plages. In the final layers of the solar atmosphere, the transition region and the corona, these features can be observed under the form of *coronal loops* which connect the opposite magnetic polarity regions, but can also contain open field structures. Active regions are fairly unstable features and are the origin of most eruptive solar events such as *coronal mass ejections* and *flares*, which are discussed further on in Section 1.2.

Coronal streamers (e.g., Rachmeler et al. 2014) are bright, white-light extended radial structures with a helmet like-shape in the inner part. They usually overlie coronal loops anchored in two regions of opposite magnetic polarity, that are being dragged outwards by the constant outflow of solar plasma (solar wind). Because of their closed nature at the base, plasma trapped in those underlying loops can be released into the heliosphere when reconnection with the nearby

open field lines occurs (Kallenrode 2004). This process gives rise to the *slow solar wind*, as compared to the plasma from coronal holes that can freely escape into the interplanetary space due to the open magnetic configuration, giving rise to the fast solar wind. During solar minimum, coronal streamers can be seen mostly around the equatorial plane (left panel of Figure 1.5), since the magnetic poles are more clearly delimited and organized in this period. During maximum solar activity, they can be seen at almost any latitude, even at the poles (right panel of Figure 1.5). Pseudo-streamers are very similar structures, formed of closed loops in the lower corona that overlie two (or an even number of) polarity inversion lines, the extended magnetic domains having the same polarity.

1.1.3 Solar wind

The tremendous temperatures of the solar corona create a non-equilibrium state and make it expand outwards, forming the *solar wind*. This represents a continuous, yet variable in space and time, flow of particles from the Sun into the interplanetary space. The Sun loses $2 \times 10^{-14} M_{\odot} \text{yr}^{-1}$ through this process (Cohen 2011). The extension of the solar magnetic field into the interplanetary space bears the name of *interplanetary magnetic field* (IMF), and carries the sign of the photospheric polarity. It is highly dependent on the solar activity cycle, and at minimum it presents as an organized bipolar structure overlying the equatorial streamer belt and a global neutral line (where the polarity changes sign). The interplanetary extended boundary between the open field lines of opposite magnetic signs creates the *heliospheric current sheet* (HCS), seen in Figure 1.6. It is also present during solar maximum, but it has a more irregular shape due to the large number of coronal streamers and active regions appearing on the solar disk. The HCS is said to resemble a ballerina skirt because of the magnetic field that gets dragged along with the rotating Sun, and due to the misalignment of the magnetic and rotating axes (left panel, Figure 1.6).

Historically, in 1691 the interplanetary medium was thought by the scientist Robert Boyle to be some sort of vacuum called *æther*, which was filling all space and was transmitting light and heat without interfering with the motion of bodies through it. This notion was challenged in 1955 by Ludwig Biermann, who proposed a continuous stream of charged particles ("continuous corpuscular emission") being emitted from the Sun, in order to explain changes in the orientation of comet tails (Biermann 1952, 1955). Only three years later, Eugene Parker proposed the first mathematical description of the solar wind (Parker 1958) based on Biermann's theory of a radial, continuous, outward stream. The key components were outward flows of non-rotating and isothermal plasma from the Sun, which accelerated to supersonic speeds within a few R_{\odot} .

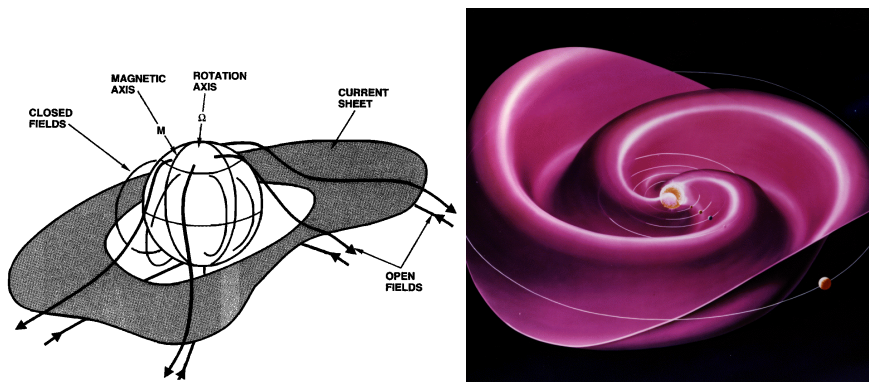


Figure 1.6: Left: The shaded area is the heliospheric current sheet, lying between open field lines of opposite magnetic polarity. Underneath it there are closed magnetic loops anchored on both ends on the Sun. The rotation axis of the Sun does not match the magnetic N-S axis. From Smith (2001). Right: 3D visualization of the heliospheric current sheet resembling a rotating ballerina skirt, extending throughout the solar system.

In 1959, just one year after Parker's theory, the Soviet satellite *Luna 1* proved the existence of the solar wind by taking *in situ* measurements during its journey to the vicinity of the Moon. As opposed to remote-sensing images, *in situ* data are taken at the location of the spacecraft, measuring the parameters of the environment through which the instruments pass. Throughout the following decades, several other spacecraft have been launched in the search for more information regarding the interplanetary medium. Parker's supersonic expansion of the corona was proven in the early 1960's by the measurements taken by two NASA spacecraft, *Explorer 10* and *Mariner 2* (Bonetti et al. 1963; Heppner et al. 1963; Neugebauer 1997). In 1963, Snyder et al. (1963) noted from Mariner 2 observations that the solar wind (at minimum) was organized into corotating streams of fast and slow solar wind.

During this time, theories expanding Parker's hydrodynamic solution were being developed, in which the magnetic field was also included. These theories introduced new notions and three other critical points (apart from the sonic one) which are the locations where the solar wind speed exceeds the characteristic speeds at which disturbances propagate through magnetized plasma. These three characteristic speeds were formulated by Weber & Davis (1967) and by Alfvén (1942), and are the *slow magnetosonic*, *fast magnetosonic* and *Alfvén* speeds. At distances larger than the furthest critical point, waves cannot travel towards the Sun anymore, as the medium in which they propagate sweeps them outwards.

Consequently, if a perturbation travels faster than these characteristic wave speeds, it induces shocks in the system. Shocks are formed when information from the disturbance cannot travel ahead of the wave, in the medium in front of it, and as such non-linear effects become important. This happens when the amplitude of the wave becomes large enough such that the crest propagates faster than the leading or trailing edge, steepening the front and creating a *shock wave* or a *turbulence*. These are correlated with discontinuities in the hydrodynamic and magnetic parameters of the plasma (Priest 2014). Shocks were first identified in the solar wind in Mariner 2 data by Sonett et al. (1964), and they defined the event as a *hydromagnetic shock*, and described it as a *rapid, apparently irreversible change in the interplanetary plasma and magnetic field*.

Important milestones regarding the exploration of the solar wind within 1 AU were achieved by the twin spacecraft *Helios 1* and *Helios 2*, which were launched in December 1974 and January 1976, respectively. They provided information on solar plasma, the solar wind, cosmic rays, and cosmic dust, performed magnetic field and electrical field experiments, and also observed the dust and ion tails of at least three comets. The exploration of the solar wind beyond 1 AU was aided by the two *Pioneer 10* and *11* spacecraft which were launched in March 1972 and April 1973, and whose instruments were used to study the asteroid belt, the environment around Jupiter, the solar wind, cosmic rays, and eventually the outer regions of the Solar System and heliosphere. In the summer of 1977, the twin *Voyager 1* and *2* spacecraft were launched, and nearly 40 years later they made their historic entry into interstellar space, still sending valuable scientific information back to Earth.

Another important step was achieved along with the discovery of the dual nature of the solar wind as a function of latitude (Kojima & Kakinuma 1990; Rickett & Coles 1991), using the interplanetary scintillation (IPS, Hewish et al. 1964) method. The joint NASA/ESA *Ulysses* mission was launched in 1990 and carried out extensive in situ measurements over the poles of the Sun (McComas et al. 1998). The Solar Wind Observations Over the Poles of the Sun (SWOOPS, Bame et al. 1992) instrument recorded the solar wind speed, temperature and density as it passed through it, and confirmed their latitudinal dependency. This can be more easily seen in the top left panel of Fig. 1.7, which shows a faster solar wind measured at high latitudes as compared to the low equatorial values corresponding to helmet streamers (McComas et al. 2003, 2008). The faster solar wind originates from coronal holes, regions of open magnetic field where plasma can easily escape and accelerate. The latitudinal delimitation is more clear during solar minimum, as compared to the solar maximum when active regions, sunspots, streamers and CMEs are omnipresent, thus influencing the overall structure of the solar wind. The evolution in time of the sunspot number

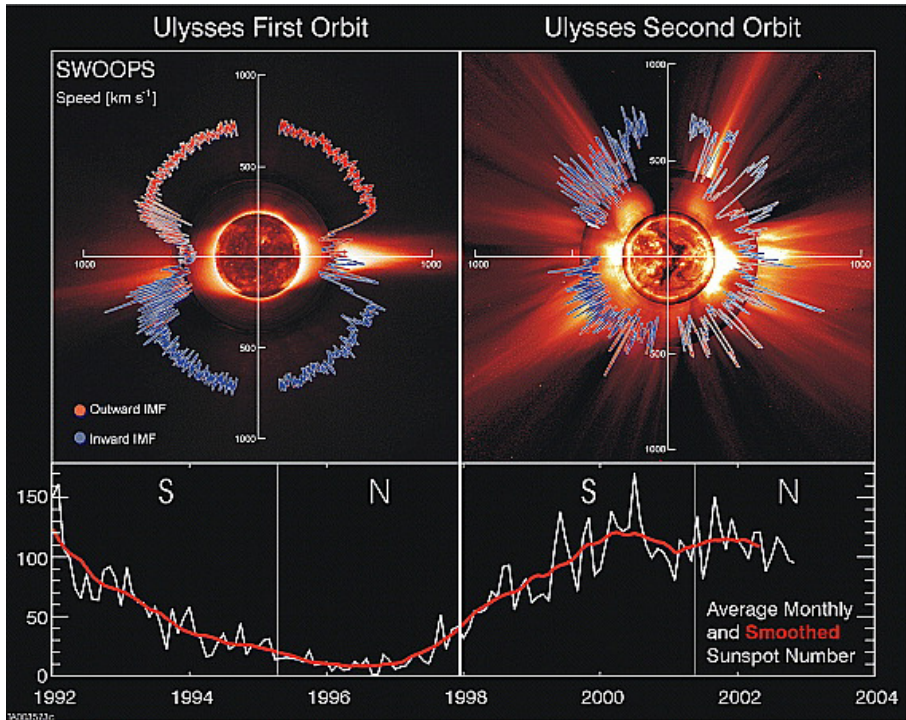


Figure 1.7: Top: Polar plots of solar wind speed as a function of latitude for Ulysses' first two orbits. They are plotted over solar images characteristic of solar minimum (image taken on 17 August 1996) and maximum periods (image taken on 07 December 2000) observed by: Solar and Heliospheric Observatory (SOHO) Extreme ultraviolet Imaging Telescope (195 \AA), the Mauna Loa K-coronameter (700-950 nm), and the SOHO C2 Large Angle Spectrometric Coronagraph (white light). The telescopes are listed from center outwards. Bottom: Average monthly (white line) and smoothed (red line) sunspot number, showing that the first orbit occurred through the solar cycle declining phase and minimum while the second orbit spanned solar maximum. From: McComas et al. (2003).

is shown in the bottom panel of Figure 1.7, indicating the previously mentioned correlation with the solar activity cycle. Average speeds were measured for the fast wind to be $700\text{--}800 \text{ km s}^{-1}$, and for the slow wind between $300\text{--}500 \text{ km s}^{-1}$, in their 'steady' state around minimum solar activity.

The main constituents of the solar wind are charged particles, i.e. protons and electrons, but a small portion of α particles (3-4% in number density) is also

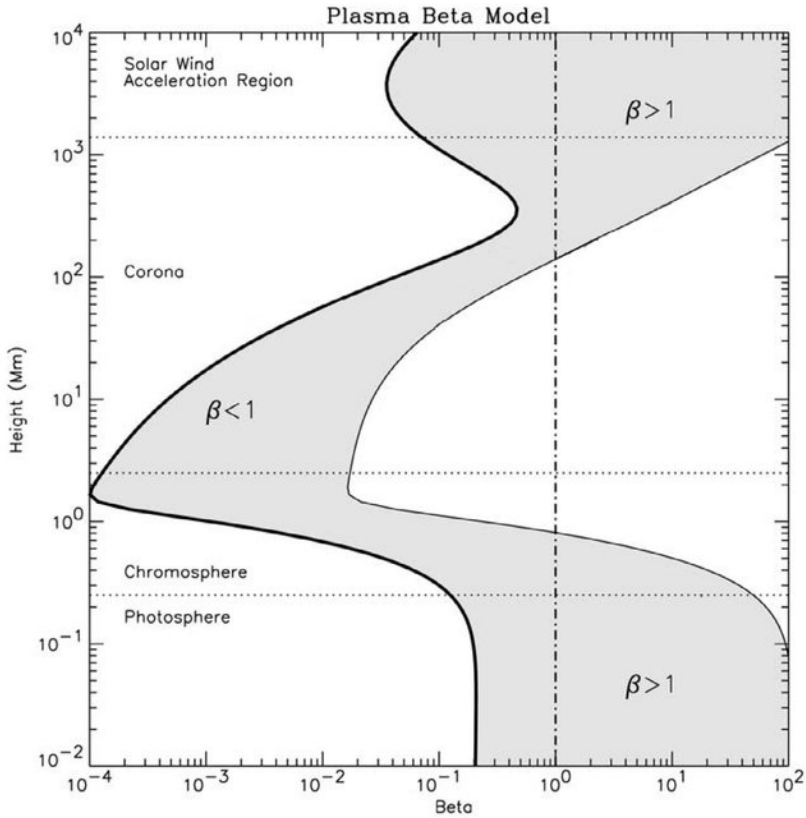


Figure 1.8: Model of plasma β above an active region. Values of plasma β are shown in the gray area as a function of height, delimited by a sunspot of strong 2500 G magnetic field (thick boundary) and a region of only 150 G (thin boundary). The vertical dot-dashed line indicates locations of $\beta = 1$, where plasma and magnetic field have equal dynamic contributions. Credits: Gary (2001).

found. Other ionized heavy elements are present in even smaller proportions, such as carbon, nitrogen, oxygen, iron, and others (e.g., Zurbuchen et al. 2002). Differences other than speed do exist between the two solar wind latitudinal components, the slow wind being denser than the faster one, but also cooler. The proton temperature is lower for the slow wind, but the electron temperature is the same for both winds. The average electron density in the slow wind is $7 \times 10^6 \text{ m}^{-3}$, while in the fast one is $2.5 \times 10^6 \text{ m}^{-3}$ (Priest 2014; Owens 2020). In terms of composition, the fast wind resembles more the photospheric environment, with low $\text{O}^{7+}/\text{O}^{6+}$ charge-state ratios, whereas this ratio is higher in the slow wind, indicating its coronal origin for which the temperature increases the level of ionization (Cranmer et al. 2017).

We mentioned earlier that plasma and magnetic field move as one system, and this property is called the *frozen-in condition*. Whether plasma or the magnetic field is the dominant component can be assessed via a parameter that represents the ratio between the thermal pressure (p) and magnetic pressure (p_{mag}), plasma β :

$$\beta = \frac{p}{p_{mag}} = \frac{2\mu_0 n k_B T}{B^2}, \quad (1.1)$$

where μ_0 is the vacuum permeability, n is the number density, k_B is the Boltzmann constant, T is the temperature, and B the magnetic field.

In the solar wind $\beta \gg 1$, which results in plasma dominating the movement of the system, due to the radial dependencies of the thermal and magnetic pressures at high distances. In active regions, the chromosphere and the corona, $\beta \ll 1$ due to strong magnetic field being the dominant component and dictating the motion of the plasma. Figure 1.8 shows the evolution of plasma β with distance above an active region, as computed by the model of Gary (2001).

1.2 Coronal mass ejections and associated phenomena

1.2.1 Definition and description

Coronal mass ejections (CMEs) are defined as *an observable change in coronal structure that 1) occurs on a time scale of a few minutes to several hours and 2) involves the appearance (and outward motion) of a new, discrete, bright, white light feature in the coronagraph field of view* (Hundhausen et al. 1984; Schwenn

2006). CMEs have been observed extensively for nearly 50 years now, but the first documented observation, if it can be called so, was the fortuitous drawing of G. Tempel of the corona during the total solar eclipse in 1860 (Figure 1.9). It depicted the radial streamers, prominences close to the disk, as well as a spiraling structure, which is believed to have been a CME. Ever since, they have been observed more intensively and accurately, their description evolving greatly from just a white spiral near the Sun. CMEs are one of the most powerful and dynamic events of the solar system and of the solar eruptive activity, which may severely influence the space environment around our planet.

CMEs are enormous in size, spanning millions of kilometers, and weighing on average 3×10^{12} kg. They account for 5-10% of the solar wind mass-loss, depending on at which time during the solar activity cycle they occur (Priest 2014). CMEs are often associated with eruptions from solar active regions. Consequently, the frequency of these ejections depends greatly on the phase of the solar cycle, from 2-3 per week during solar minimum, up to 5-6 per day during solar maximum activity (Lugaz et al. 2017b). Their speed range also covers a wide spectrum, from 20 km s^{-1} up to 3500 km s^{-1} , with an average of $300\text{-}500 \text{ km s}^{-1}$ (Priest 2014). These values are only lower limits because coronagraph measurements provide only two-dimensional images projected on

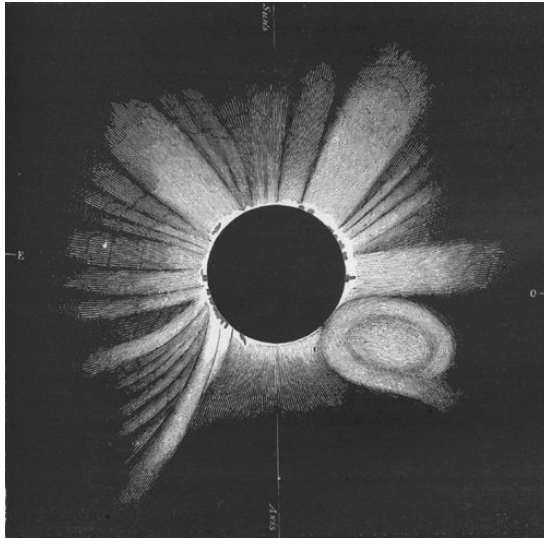


Figure 1.9: Drawing by G. Tempel of the 1860 eclipse depicting coronal streamers, but also what is believed to be the very first observation of a CME. Credits: Vaquero & Malville (2014).

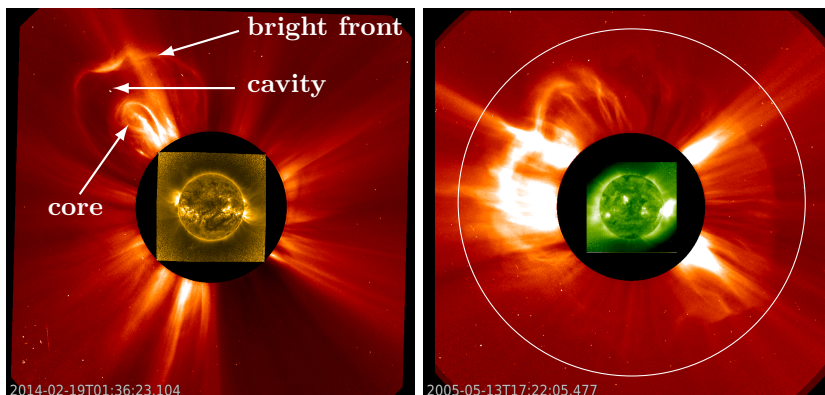


Figure 1.10: Left: Images of a three-part structure CME, observed by PROBA2/SWAP (interior) in EUV (174 \AA) and by SOHO/LASCO C2 coronagraph (exterior) in white-light, taken on 19 February 2014. Right: Images of a full halo CME, observed by Extreme-Ultraviolet Imaging Telescope (EIT, in 195 \AA) and LASCO C2 onboard the SOHO spacecraft, taken on 13 May 2005. The white circle encompasses the bright front of the halo CME.

the plane of the sky. The angle between the sides of a CME and the center of the Sun is called apparent *angular width*, which also varies during the solar cycle, with median values between 47° and 61° (Yashiro et al. 2004). If this angle becomes 360° , the eruption is called a *full halo CME*. This parameter is relative with respect to the view point, since a CME directed towards the observer can appear as a full halo, whereas if seen from a lateral side, it can have a lower angular width value. An example of a full halo CME can be seen in the right panel of Figure 1.10, with the white circle approximately delimiting the edges. Such eruptions represent $\approx 3\%$ of all CMEs (Gopalswamy et al. 2015), and they are of particular interest to forecasters since they usually bear a component directed towards or away from the observer. The effects of Earth-directed CMEs will be discussed in Section 1.3.

Statistical analysis of coronagraph observations also showed that many CMEs have a three-part structure, as seen in the left panel of Figure 1.10: a bright leading front, a dark cavity and an inner bright core (Illing & Hundhausen 1985; Gibson & Low 1998; Vourlidis et al. 2013). The bright front is created by the accumulation of coronal plasma at the top of the expanding CME. The cavity is usually believed to be a magnetic flux rope, which is a helical structure composed of magnetic field lines winding around a common axis. The bright core of a CME is thought to be filament (or prominence) matter that is suspended in magnetic dips of a flux rope configuration. The flux rope structure has been

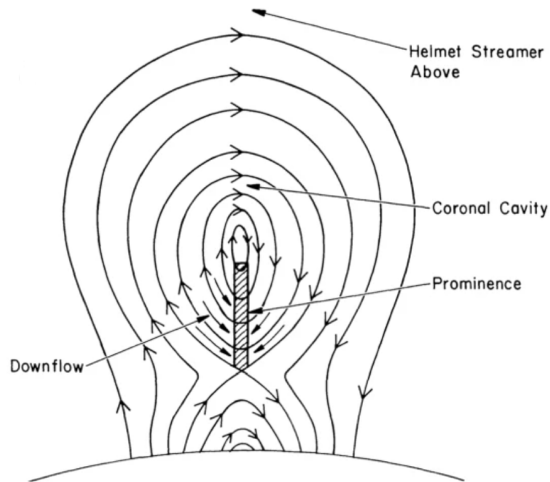


Figure 1.11: A cross-section through a 2.5D model of a flux rope. Adapted from Gibson (2018).

revealed by Faraday rotation that can measure CME magnetic field (Wood et al. 2020). A cross-section of such a prominence sitting at the bottom of a flux rope can be seen in Figure 1.11.

1.2.2 Spacecraft observing the Sun and CMEs

All of the above parameters could be determined as a result of the many spacecraft that have been launched with the goal of studying these eruptions and the solar environment. Coronagraphs have been an amazing asset in this process, especially the ones onboard the Solar and Heliospheric Observatory (SOHO). Launched in 1995, SOHO, along many other spacecraft, is slowly orbiting around Lagrange point 1 (L1), where the gravitational pull between Earth and Sun and the centrifugal force are equal, making it a good location for satellites. The Large Angle and Spectrometric Coronagraph (LASCO, Brueckner et al. 1995) onboard SOHO is the suite of three coronagraphs with increasingly large fields of view, out of which two are still functional (C2 and C3). Two examples of observations taken by LASCO C2 coronagraph can be seen in Figure 1.10.

Later on, in 2006, the twin Solar TERrestrial RELations Observatory (STEREO, Kaiser et al. 2008) spacecraft were launched, one orbiting ahead of the Earth (STEREO-A) and the other one behind (STEREO-B). Their mission was to

obtain data in order to analyze the 3D structure of CMEs and other solar transients, as well as to obtain a full coverage of the solar surface. Each carries onboard two white-light coronagraphs with two fields of view, COR1 and COR2 (Thompson et al. 2003), as well as an Extreme Ultraviolet Imager (EUVI, Wuelser et al. 2004) and two Heliospheric Imagers (HI-1 and HI-2), as part of the Sun Earth Connection Coronal and Heliospheric Investigation (SECCHI, Howard et al. 2008) experiment. Unfortunately, the contact with STEREO-B was lost on the 1st of October 2014, during practice operations with the purpose of preparing the spacecraft for the loss of signal that it would have experienced when behind the Sun.

At the end of 2009, the Project for Onboard Autonomy (PROBA2) spacecraft was launched, and has been observing the Sun (e.g. left panel of Figure 1.10) from an orbit around the Earth ever since, even though the nominal mission was planned for only two years. It hosts two important instruments, an extreme ultraviolet (EUV) imager with a large field of view, the Sun Watcher with Active Pixels and Image Processing telescope (SWAP, Seaton et al. 2013), and a radiometer observing from soft X-ray to mid-ultraviolet, called Large Yield Radiometer (LYRA, Dominique et al. 2013). Initially, they were projects mainly for technology demonstration, but they also contribute scientifically to topics related to CMEs, EUV features and solar flares.

Only several months later, at the beginning of 2010, the Solar Dynamics Observatory (SDO) was launched from Cape Canaveral, carrying onboard two main experiments, the Helioseismic and Magnetic Imager (HMI, Schou et al. 2012) and the Atmospheric Imaging Assembly (AIA, Lemen et al. 2012). HMI is an instrument that provides data on photospheric movements and magnetic field, using the Doppler shift of the Fe I 6173 Å spectral line. AIA is a suite of four telescopes, imaging the Sun in a total of ten different wavelengths, out of which seven are in EUV, two in UV, and one in visible light. Their goal is to reveal key aspects of solar activity (Pesnell et al. 2012). An overview of the Sun viewed in all different SDO wavelengths can be seen in Figure 1.12, along with an indication of the regions of the solar atmosphere that are imaged.

More recently, two other spacecraft have been deployed that are already revolutionizing our way of understanding the Sun. The Parker Solar Probe (PSP, Fox et al. 2016) was launched in 2018 and is revolving around the Sun in a highly elliptical orbit. At its minimum perihelion it will reach closer to the Sun than any man-made object ever did, and it will probe the solar corona from a distance of only 5.6 million km (less than 10 R_{\odot}) above the Sun's surface. PSP carries four instrument suites that image the solar wind and take in situ data to study magnetic fields, plasma and energetic particles. In 2020, Solar Orbiter (SolO, Müller et al. 2013) was launched with the goal of understanding the origins of the solar wind and probing the polar regions, reaching up to

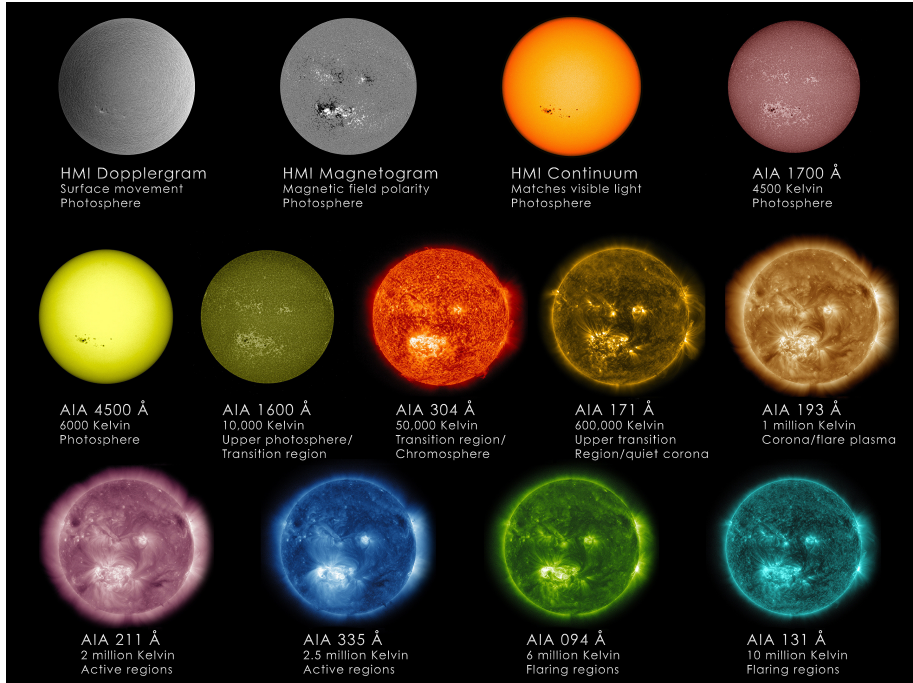


Figure 1.12: The Sun viewed in all wavelengths of HMI and AIA onboard SDO spacecraft. Below each image are specified the instrument and wavelength, the associated temperature, and the region of the solar atmosphere that is observed or measured. Credits: NASA/SDO.

$\sim 33^\circ$ latitude. It has 10 instruments onboard that are taking both in situ measurements and remote sensing observations from a plane out of the ecliptic and close to the Sun. At its minimum distance, it will reach as close as 0.28 AU ($\sim 60 R_\odot$). The data from PSP and SolO will be used in combination with other remote-sensing and in situ instrumentation to determine the evolution and origins of solar wind plasma flows, streamers, and energetic particles. A 3D distribution of the solar wind and CMEs will also be obtained by simultaneously using measurements from all these separate vantage points, promising new results in understanding the fundamental physical processes involved (Velli et al. 2020).

1.2.3 CME eruption mechanisms

Even though thousands of observations of CMEs are available, the physical mechanisms that generate them and their propagation throughout space remain, in many aspects, unclear. However, there is some observational consensus regarding the nature of the CME trigger. The computation of energetics during eruptions indicates that the magnetic energy density is far more dominant than the kinetic, thermal and gravitational ones, making it the only possible source for solar eruptions (Forbes 2000). On the other hand, magnetic energy does not impose any movement of the structures involved, and CMEs are highly dynamic events. Therefore, an additional mechanism is required for the magnetic energy to be converted into motion and heat for the ejecta to be created and accelerated, which is magnetic reconnection. This leads to a generally accepted scenario of CMEs, which contains magnetic arcades that overlie areas of opposite magnetic signs. The thin regions where the magnetic field changes sign are called *polarity inversion lines* (PILs), or *neutral lines*. The stable arcades are subject to photospheric movements, either vertical or horizontal, that increases the magnetic stress in the corona and results in a loss of equilibrium and eventually eruption. There are several mechanisms proposed to be involved in this evolution towards instability, and a comprehensive list can be found in Chen (2011). We will discuss in this Chapter some of the most important types of triggers: *shearing motions*, the *magnetic breakout model* and *flux emergence*.

Shearing motions are an efficient way of building up free energy in the corona (Low 1977). They are ubiquitous in the solar atmosphere, due to the differential rotation of the Sun (large time-scales), but also due to the localized motions of granular and super-granular structures (smaller time-scales). Shearing motions involve anti-parallel movements of the photosphere, usually along a polarity inversion line and onto an arcade connecting two regions of opposite magnetic sign (Figure 1.13a). Due to the frozen-in condition, motion of the plasma drags the footpoints (the location of magnetic field lines entering the solar surface) along with it, shearing the arcade and making the field lines more aligned to the neutral line. Observations show that in active regions, the horizontal velocities are $\approx 0.1 \text{ km s}^{-1}$ and can produce displacements of $\approx 10^4 \text{ km}$ in only one day, as compared to quiescent regions where the displacements are generally smaller and are caused by differential rotation of the Sun. These horizontal movements bring together the twisted field lines and induce reconnection, as shown in Figure 1.13. Here, shearing motions are presented in combination with *flux cancellation*, produced by the flows towards the PIL. Flux cancellation represents the physical explanation for disappearance of magnetic flux from the photosphere, experienced by the submerging loops CB and GF in Figure 1.13. This is possible due to the downward magnetic tension of the overlapping

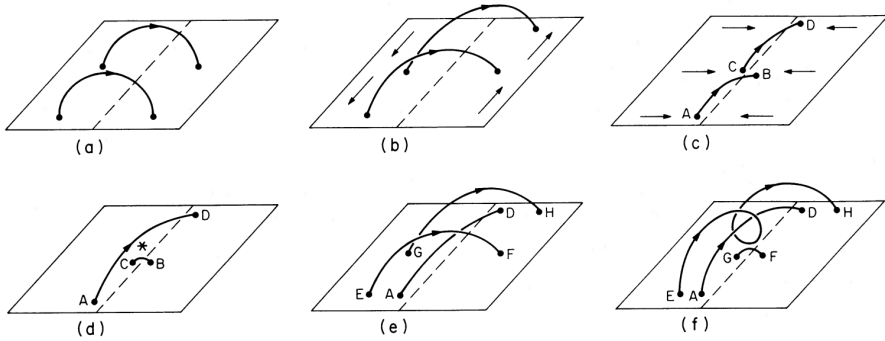


Figure 1.13: Schematic of the effect of shearing motions and flux cancellation on a magnetic arcade, and formation of a flux rope. The rectangle represents the photosphere, and the dashed line the PIL. (a) initial magnetic arcade overlying a PIL; (b) sheared magnetic field due to anti-parallel motions along the PIL; (c) flows towards the PIL increase even more the magnetic shear; (d) reconnection between the two sheared field lines creates the large loop AD and a smaller one, CB, which submerges; (e) more overlying field lines (EF and GH) are pushed together and sheared; (f) the reconnection process in (d) is repeated and a helical flux rope (EH) is formed, along with another small underlying loop GF that submerges. Credits: van Ballegoijen & Martens (1989).

loops becoming larger than the upward magnetic buoyancy (Parker 1955) of the much smaller loops. The result of these repetitive combined processes is the formation of a twisted flux rope, seen in the final panel of the same Figure. The cold plasma of filaments and prominences discussed earlier usually resides inside, at the bottom of these flux ropes, but may also not accumulate at all. If the shearing flows continue to act on the footpoints of the arcade, they increase the magnetic pressure in the coronal environment, potentially reaching a critical threshold from where the flux rope along with the prominence material (if any) expands (Barnes & Sturrock 1972) and erupts (Mikic & Linker 1994). Such a scenario has been numerically simulated by, for instance, Jacobs et al. (2006), who investigated the effect of different shearing profiles on the subsequent eruptions. This mechanism is also important for this thesis since it is the basis of our simulations and the triggering method used to obtain CMEs.

The *magnetic breakout model* (Antiochos et al. 1999) can be used to explain the eruptions occurring from a particular type of magnetic structure, but which is commonly encountered in the solar atmosphere. The initial state can be seen in the left panel of Figure 1.14 and consists of a quadrupolar magnetic configuration with three arcades and three neutral lines, overlapped by a helmet

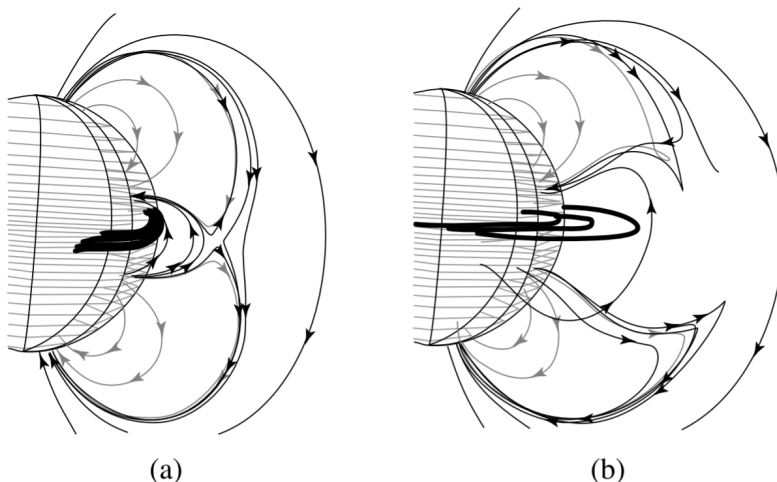


Figure 1.14: Evolution of the magnetic field during an eruption following the breakout model in an early (a) and late stage (b). The sheared arcade field (thick lines) expands outwards and reconnects with the upper magnetic field lines, removing the overlying constraints and allowing the CME to occur. Credits: Lin et al. (2015).

streamer. When the middle smaller arcade is sheared due to photospheric motions or magnetically stressed by other means, it starts expanding as in the previously described mechanism. This pushes together the top of the middle arcade and the overlying streamer field lines which are oppositely directed, thus inducing reconnection, also known as external *tether-cutting* or *breakout reconnection*. The right panel of Figure 1.14 shows the evolved state of this process, through which the downward magnetic tension is reduced, along with the breaking of the streamer field lines. This allows the arcade to expand even more and continue to reconnect, opening up the overlying streamer similar to peeling the layers of an onion. This positive feedback effect allows the arcade to escape the constraining coronal magnetic field and to create a CME. In their study, Ugarte-Urra et al. (2007) found that the eruption of 7 CMEs from their selection of 26 events could be explained through the mechanisms of the breakout model.

Flux emergence is another type of mechanism through which new magnetic flux appears on the photospheric boundary. Flux emergence has been observed in magnetograms in the pre-eruptive phase of many CMEs (Feynman & Martin 1995), when their polarity orientation was favorable for reconnection processes

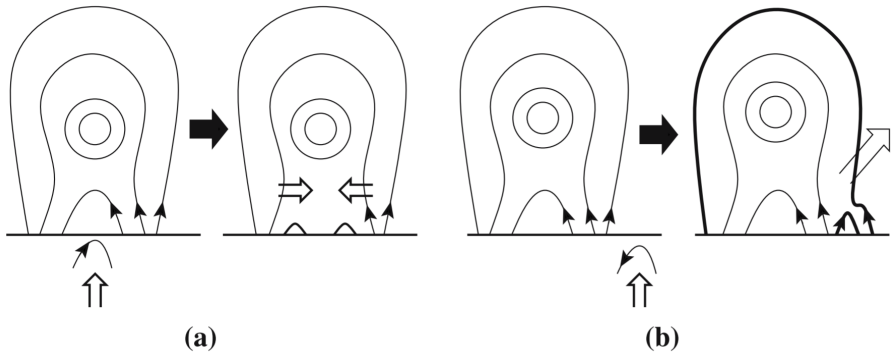


Figure 1.15: Schematic diagram of flux emergence as a trigger mechanism for CMEs. The new magnetic loop emerges from below the photosphere either (a) inside or (b) outside the filament channel, reconnecting with the nearby (thick black) field lines. Credits: Chen (2008).

with the filament structure (*filament channel*). Therefore, it was proposed as a possible triggering mechanism for CMEs by Chen & Shibata (2000), in the two ways described in Figure 1.15. If the new arcade surfaces from below the photosphere under the filament channel, it reconnects with the small loop that was already present, canceling it out and creating two other small loops of opposite magnetic orientation. This process is shown in panel (a) of Figure 1.15. As a result, the magnetic pressure decreases locally and the sides of the large overlying arcade are drawn together, due to the reduced pressure underneath the filament channel. This creates a current sheet under the flux rope, pushing it slightly outwards, which may be enough to trigger the eruption. The second option involves emergence of the sub-photospheric arcade outside the filament channel. If its orientation is magnetically favorable for reconnection with the large overlying field lines (thick black lines in panel (b)), it removes some of the confining field and decreases the downward magnetic tension. This allows the flux rope to slightly rise, form a current sheet, and also in this case, potentially erupt.

In reality, the solar corona is more complex than the simple cartoons depicted here, therefore the reasons for CMEs initiation are very often a combination of the described processes.

Standard CSHKP model and source signatures

Regardless of the triggering mechanism, once they overcome the instability threshold and erupt, CMEs generally form according to the *standard CSHKP (flare) model* (e.g., Carmichael 1964; Sturrock 1966; Hirayama 1974; Kopp & Pneuman 1976), depicted in Figure 1.16. The erupting ejecta (potentially a filament or prominence, seen in the bottom right panel of Figure 1.17) has a typical magnetic structure of a flux rope, that by one or more of the above-mentioned mechanisms, became unstable and started rising. The magnetic reconnection in the current sheet above the PIL fully detaches the expanding arcade and creates the *plasmoid*. This process is called *flare reconnection* and converts even more magnetic energy into kinetic energy, accelerating the ejecta away from the Sun. If this process takes place on short time-scales and in regions of strong magnetic field, the thermal energy also created through the reconnection is observed in many wavelengths as a sudden increase in brightness.

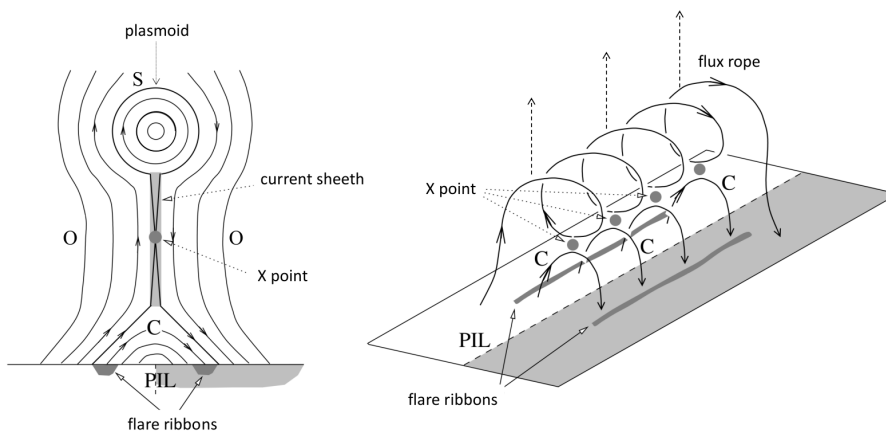


Figure 1.16: Schematic of the standard CSHKP model viewed in 2D (left) and in 3D (right). In 2D, open field lines (O) of opposite polarity form a current sheet (grayed out vertical region). They reconnect at a magnetic X-point to create closed field lines (C) and a plasmoid. The energy released by magnetic reconnection creates chromospheric flare ribbons on either side of the PIL, just inside the separatrix (S). In the 3D version, magnetic reconnection occurs at several sites (X-points) to create closed field lines (C) and a twisted flux rope instead of a plasmoid. The PIL separates regions of opposite photospheric magnetic flux. The 2D image is basically a cross-section perpendicular to the PIL through the 3D image. Adapted from Longcope & Beveridge (2007).

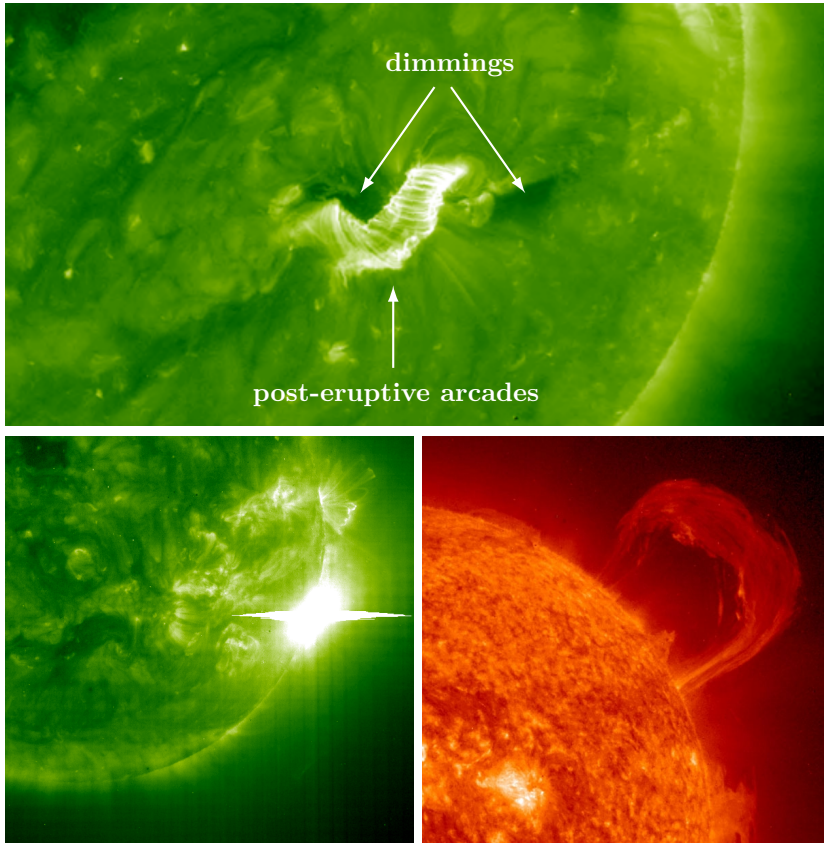


Figure 1.17: Phenomena associated with CMEs. Top: Dark dimmings caused by coronal mass evacuated along with the CME. Bottom: Large flare (left) and prominence eruption (right). Credits: NASA, European Space Agency (ESA), Solar-Terrestrial Centre of Excellence (STCE).

Such an event is called a *flare* and an example can be seen in the bottom left panel of Figure 1.17.

Flares

Flares are the most violent phenomena in the solar system and they can release energies of up to 6×10^{25} J (6×10^{32} erg). They are very efficient mechanisms of accelerating particles, which can also be present during eruptive events, to high energies (Priest 2014). Flares are observed mostly in X-ray and EUV

wavelengths, but strong ones can be seen even in visible light. Depending on their X-ray flux measured near Earth, flares are classified as A, B, C, M or X (from weakest to strongest), the intensity of each level being 10 times greater than that of the previous one. The correlation between flares and CMEs increases along with the strength of the flare (Yashiro et al. 2006): up to 90% of X-class flares is associated with a CME, whereas flares without CMEs are predominantly below C-class. CMEs associated with flares are usually faster than those without, and are impulsive and more energetic (Gosling et al. 1976; Zhang et al. 2001; Lin 2004). In the majority of cases where a correlation can be made, CMEs occur before the flare (Zhang et al. 2002). Even though they are fairly uncommon, flares without associated CMEs do occur, and they are called *confined flares*. The main generally accepted mechanism for their non-eruptive behavior involves the presence of high altitude overlying arcades of strong magnetic field above the flaring region, that prevent solar material to be ejected and to create a CME (e.g., Thalmann et al. 2015; Li et al. 2022).

Other source signatures

As the current sheet undergoes reconnection and the CME lifts off, new closed magnetic loops (loops *C* in Figure 1.16) are created under the expanding flux rope, during which particles are accelerated towards the solar surface. When they collide, they heat up the plasma at the footpoints of the arcades, creating *flare ribbons* that can also be seen in Figure 1.16. This evaporation process makes the material rise and follow the newly created loops, lighting them up and visualizing them in observations as *post-eruptive arcades* (top panel of Figure 1.17). The reconnection point in the current sheet (X-point) keeps increasing in height along with the expulsion of the CME, thus creating higher altitude magnetic loops whose footpoints are more spread out from each other. Since the chromospheric evaporation continues to take place with each newly formed loop, this makes the flare ribbons appear as if they distance away from each other and from the PIL. Another consequence is that the post-eruptive arcades seem to grow and increase in size.

At the same time, the coronal response in EUV and X-ray wavelengths to these strong eruptions are *coronal dimmings*, seen in the top panel of Figure 1.17 on the sides of the post-eruptive arcades. They are observed as darker areas in the footpoints locations of the magnetic loops as a result of the mass depletion caused by the plasma being dragged out with the CME (e.g. Hudson et al. 1996; Sterling & Hudson 1997; Dissauer et al. 2018).

Another phenomenon that can be observed during CME events is called an *EIT wave* or *EUV wave*. They are large quasi-circular wave fronts propagating

away from the eruption site, in the coronal environment. Their name originates from the first instrument that observed them, the Extreme-ultraviolet Imaging Telescope (EIT, Delaboudinière et al. 1995) onboard the SOHO spacecraft, being reported for the first time by Thompson et al. (1998). They were soon associated with CMEs (Plunkett et al. 1998), and proven to be truly correlated with them statistically by Biesecker et al. (2002). There are several possible explanations for their appearance after CMEs, including fast and slow MHD waves, but also pseudo-waves caused by the reconfiguration of the magnetic field in front of the CME, as its front compresses the corona.

A by-product of solar eruptive events are solar energetic particles (SEPs, Ryan et al. 2000; Klein & Dalla 2017), which are predominantly protons and electrons that are accelerated to tens of MeV energies. Occasionally, they can even be accelerated to quasi-relativistic speeds, with energies reaching up to several GeV. They can reach such speeds either during the reconnection processes at the site of the eruption, or due to acceleration at interplanetary shocks, which can be created by the propagating CME. The energetic particles travel through the interplanetary space predominantly along the magnetic field lines of the Parker spiral, and can reach Earth in only a few minutes, up to several hours. SEPs are extremely important since they can endanger the lives of astronauts, as well as damage the instrumentation in space.

All of the above described solar phenomena, i.e. filaments, flares, flare ribbons, post-eruptive arcades, coronal dimmings, EUV waves, form a suite of *source signatures* of CMEs, which help identify the location of the eruption origin. The events for which all these features are present are rare, and mostly several or just one can be observed. However, during solar minimum the percentage of eruptions correlated with a clear source region is much lower (Ma et al. 2010), as is the overall number of CMEs. Forecasters use these signatures to assess whether a CME is Earth-directed or not, making them crucial for the prediction of an upcoming geomagnetic effect, as the ICME passes Earth (discussed further in Subchapter 1.3). There are also cases in which a front-sided CME that is seen in a coronagraph is associated with none of these features, and these particular events are the topic of the next Subchapter.

1.2.4 Stealth coronal mass ejections

We mentioned in the previous Subchapter that not all CMEs have source signatures associated with them such as filament or prominence eruptions, flares, flare ribbons, post-eruptive arcades, coronal dimmings or EUV waves. When only observations from Earth or spacecraft orbiting at the L1 point (a singular point of view) are available, a CME will be simply seen as an expanding

structure, with no information regarding its direction towards or away from our planet. For this reason, if the features usually associated with eruptions are not clearly distinguishable on the visible side of the Sun, the CME is assumed to be originating from the back-side of the Sun (facing away from Earth).

However, there have been numerous reports of geomagnetic disturbances that could not be traced back to any Earth-facing events. Almost a century ago, the correlation between large flares and noticeable changes in the geomagnetic field, ionosphere and particles surrounding the Earth was being noticed and began to be documented (Hale 1931; Newton 1943). Three decades later, discrepancies between these associations were found more and more frequently, as not all geomagnetic disturbances had a preceding solar flare (Dodson & Hedeman 1964). These unexpected disturbances in Earth's magnetic field without clearly associated solar or CME precursors were referred to as 'problem storms' (Dodson & Hedeman 1964; Dodson et al. 1974, 1979), 8% of the geomagnetic events from the rising phase of solar cycles 19 and 20 being classified as such (Dodson-Prince et al. 1978).

In more recent studies, the correlation has been made between disturbances

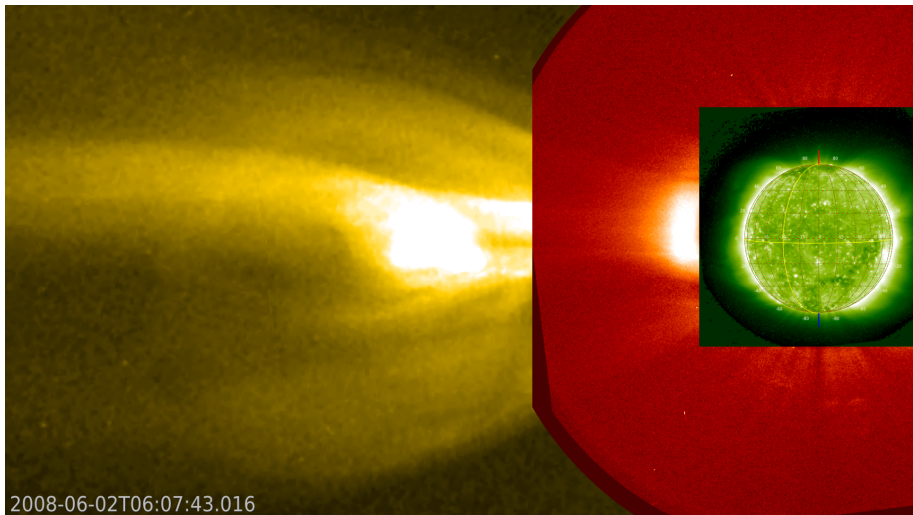


Figure 1.18: CME without low-coronal signatures observed on 2 June 2008 and analyzed by Robbrecht et al. (2009b). Images were taken by the following instruments onboard STEREO-A: EUVI 195 Å (green), COR1 in white-light (red) and COR2 in white-light (yellow). The composite image was created using the JHelioviewer software (Müller, D. et al. 2017).

recorded at Earth and CMEs, rather than just flares. The eruptions without obviously associated low-coronal signatures were named ‘stealth’ CMEs. Such an event was first investigated by Robbrecht et al. (2009b), who reported a slow CME eruption without typical source signatures on 1-2 June 2008. It was a fairly narrow ejection, spanning 54° in angular width. A snapshot of its eruption can be seen in Figure 1.18, as observed by instruments onboard STEREO-A. Using the multi-viewpoint capability provided by the twin STEREO spacecraft, Robbrecht et al. (2009b) were able to determine the unexpected origin of the CME by triangulating it to a quiet-Sun front-sided region, near a polarity inversion line. The authors concluded that the core of the CME was a large flux rope that was not filled with prominence material (*empty filament channel*). As a result of consecutive tether-cutting reconnection events over several days, the flux rope stored free magnetic energy, and it eventually crossed the instability threshold and erupted. The lack of source signatures was attributed to the large height of $1.4 R_\odot$ at which the reconnection set in. This mechanism of eruption is called a *streamer blowout*, since the high-lying flux rope that was overlying the PIL was also the core of the helmet streamer that was ejected along with it, creating the front of this stealth CME.

Empty filament channels (or with not so clear filament material) can also form and erupt from quiet regions of the Sun without having an overlying helmet streamer, as reported by Pevtsov et al. (2012). They analyzed two events driven by such a scenario, one that had a geomagnetic effect on Earth, and the other that did not. They also studied in detail the source region of the CME described by Robbrecht et al. (2009b), and noticed very faint signatures unnoticeable at a first examination, emphasizing the difficulty of forecasting the arrival of these eruptions at Earth.

From then on, many other studies reported CMEs without low coronal signatures, such as Ma et al. (2010), D’Huys et al. (2014), Kilpua et al. (2014), and Nitta & Mulligan (2017). The majority of them agree that stealth CMEs are usually narrow, with angular widths below $< 60^\circ$, and slow, with speeds below 300 km s^{-1} . In another study, Alzate & Morgan (2017) used advanced image processing techniques on the sample of 40 events reported by D’Huys et al. (2014), and located some features that could be associated with their source region. They confirm the low kinetic energies observed so far, and accentuate the need for better imaging instruments, continuous observations from separate vantage points, and a better understanding of the triggers of such enigmatic eruptions. A comprehensive study on stealth CMEs and collection of papers on the topic was performed by Nitta et al. (2021).

Another mechanism through which stealth CMEs can occur is coronal magnetic field reconfiguration, usually in the trailing current sheet of a first CME (e.g. Bemporad et al. 2012), which mainly creates small blob-like CMEs

without having clear source signatures. One of the goals of this thesis was to numerically simulate such an eruption and analyze its dynamics, in the scope of understanding the physical differences between CMEs with and without obvious source signatures. The next step was to study the effect of the stealth CME on the preceding eruption, i.e. in what ways it alters the morphology and geomagnetic impact at Earth.

1.2.5 Interplanetary coronal mass ejections

Once CMEs are expelled from the Sun, they begin their journey through the interplanetary space, and their manifestation in this environment is defined as *interplanetary coronal mass ejection*, or ICME (see Figure 1.19). The concept of ICME was introduced in different forms and varieties, from as early as 1919 by Lindemann (1919) as a simple formation containing unmagnetized material. Later on, Morrison (1956), Cocconi et al. (1958), and Piddington (1958), considered ICMEs to be magnetized structures. An important study linking CMEs observed in coronagraphs with in situ disturbances was performed by Burlaga et al. (1982), who described a magnetic structure detected by the Helios 1 spacecraft. Depending on their travel speed, but also on the characteristics of the background solar wind through which they propagate, ICMEs can reach Earth (if directed towards us) in usually 1-5 days after the eruption (Démoulin 2008). In extreme cases, it can even take less than a day for such an event to travel to us, but these cases are very rare, one example occurring in October 2003 (e.g., Manchester et al. 2008).

Ever since their first identification in the early space era (e.g., Hirshberg et al. 1970), ICMEs have been extensively analyzed and collectively concluded to have a suite of detectable features, called *in situ signatures*, but most likely not all of them are present simultaneously. They include (e.g., Zurbuchen & Richardson 2006): enhanced magnetic field strength as compared to the background solar wind; significantly lower proton temperature (Gosling et al. 1973; Richardson & Cane 1995); plasma β values much lower than 1, indicative of the dominant magnetic field contribution as compared to the plasma; bidirectional/counterstreaming suprathermal electron flows, which are evidence of the ICME still being magnetically connected to the Sun on two footpoints regions (Gosling et al. 1987; Gosling 1990); low density and monotonic decrease in the velocity profile (front faster than the end), which suggest a strong expansion of the CME; plasma composition different than that of the ambient solar wind (Richardson & Cane 2004); and reduced galactic cosmic rays count, known as *Forbush decrease*, since the strong magnetic field of ICMEs actually inhibits them from reaching the observer during its passage (Forbush 1937; Richardson & Cane 2011). A comprehensive list of ≈ 300 ICMEs in the period

1996-2009 and their in situ signatures was compiled by Richardson & Cane (2010), as well as their most probable association with the observed CME.

An important subset of ICMEs is represented by magnetic clouds (Burlaga et al. 1982) and they exhibit a very distinctive characteristic: smooth magnetic field components that rotate slowly through a large angle, indicating the presence of a helical magnetic field structure, i.e. a flux rope. Magnetic clouds represent only a small fraction of all ICMEs, approximately one third. There is also a catalog of magnetic clouds observed at 1AU in the period 2000-2003, compiled by Nieves-Chinchilla et al. (2005).

All these signatures can be found inside the ejecta, and differ greatly from the plasma and magnetic field conditions in front of the CME. If the speed of the CME exceeds the previously discussed characteristic MHD wave velocities of the background solar wind, the propagating ejecta drives a shock in front of it. This scenario can be visualized in the schematic model of an ICME in Figure 1.19. The in situ signatures of such a shock would be seen as a sudden increase in the measured magnetic field strength, speed, temperature and plasma density. The region between the shock and the ICME is called the *turbulent sheath* and is composed of compressed and heated solar wind material. The plasma parameters in this area are highly variable, and therefore much different than the more uniform values inside the ICME.

Some of the characteristic features of ICMEs can be perturbed by the interactions of the CMEs with the background solar wind, but also with other CMEs (for a review of these processes, see Manchester et al. 2017). During their propagation through the interplanetary medium, ICMEs can exhibit:

- rotations due to initial untwisting motions (Vourlidas et al. 2011; Thompson et al. 2012);
- deflections caused by coronal configurations and the ambient solar wind structures, such as coronal holes and streamers (Cremades et al. 2006; Gopalswamy et al. 2009; Winslow et al. 2016);
- global deformations of the ICME magnetic structure (Odstrčil & Pizzo 1999; Riley et al. 2004; Manchester et al. 2008);
- erosion of the magnetic field due to reconnections with the solar wind (Dasso et al. 2006; Ruffenach et al. 2015; Hosteaux et al. 2019, 2021).

The CME-CME interaction has also been investigated by several authors, such as Lugaz et al. (2017b); Shen et al. (2017). Since there are only limited in situ observations to infer how CMEs interactions evolve as they propagate away from the Sun, the physical processes involved are still yet to be fully understood. In order to study the effect they have on each other, we need to fill the measurement

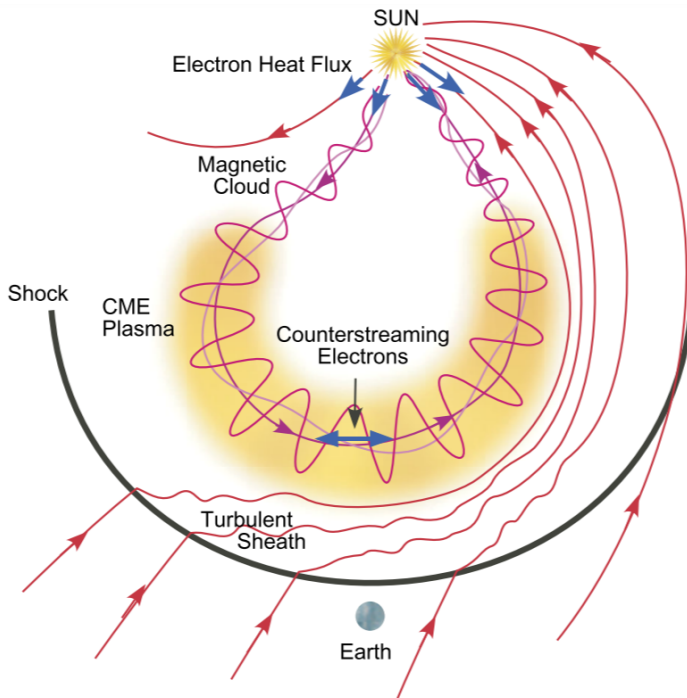


Figure 1.19: Schematic of the standard ICME model, including the basic features: frontal shock, turbulent sheath and the CME with a flux rope magnetic structure. The yellow shading indicates plasma parameters that differ from the ambient solar wind and sheath. If the CME is still magnetically attached to the Sun, counterstreaming electrons are recorded during its passage. Credit: Zurbuchen & Richardson (2006).

gap by numerical simulations, so that we can predict their configuration upon their arrival at Earth. An accurate prediction of their structure leads to a reliable forecast of their arrival at Earth, which is highly needed in the current technology-driven society, as discussed in the next Subchapter.

1.3 Space weather and geo-effectiveness

The term *space weather* refers to the entirety of the physical processes, events and effects driven by the Sun that take place in our solar system, especially in the near-Earth environment (Temmer 2021; Schwenn 2006; Pulkkinen 2007).

CMEs are the sole drivers of extreme events in the context of space weather disturbances (Gosling et al. 1991; Zhang et al. 2007; Kilpua et al. 2017). If they erupt from the visible side of the Sun, they can disrupt telecommunication, positioning and navigation systems. CMEs can also impact the electric power suppliers, spacecraft and aviation industries, and oil and gas pipelines (e.g. Schrijver et al. 2015). Solar eruptions can have an effect on Earth because our planet also carries magnetic field (creating the *magnetosphere*), which interacts with the incoming plasma and magnetic structure of the CMEs and of the solar wind. In the absence of a continuous outflow from the Sun, Earth's magnetosphere would be similar to that of a simple bipolar magnet. Because of the solar wind, the side facing the Sun is compressed, while the night-side is elongated and forms the *magnetotail*. A drawing of the magnetosphere and its components under the influence of the solar wind can be seen in Figure 1.20, showing the magnetotail extending up to several hundreds Earth radii (R_E).

Usually, at 1 AU the solar wind is super-Alfvénic and super-fast, with some exceptions caused by very low density reported in literature by e.g. Gosling et al. (1982) and Chané et al. (2015). Under normal conditions, when the super-fast solar wind impacts Earth's standing magnetosphere, a *bow shock* is formed, and is on average located at $\approx 10 R_E$ in front of our planet (Kallenrode 2004). Due to the solar wind's dynamic structure, the bow shock is not at a fixed distance, but it is rather a moving layer, extending further away in periods of tenuous interplanetary medium, and nearing the Earth during ICMEs or high pressure solar wind. The plasma and magnetic field downstream of the bow shock (towards Earth) are turbulent, with the movement of the particles being altered, and sub-sonic, in a region which is called *magnetosheath*. The boundary between the magnetospheric plasma and the magnetosheath is called the *magnetopause*, represented in Figure 1.20 by the border between white (IMF) and red (Earth) field lines. Here, the total pressure of the solar wind approximately equals the pressure exerted by the magnetosphere. The extended magnetotail is composed of two opposite polarity lobes, which create in between them the *plasma sheet*. Below several R_E lies the *plasmasphere*, which is composed of ionospheric plasma and is more symmetric between the day and night side. The plasmasphere encompasses the *radiation belts*, regions of charged energetic particles trapped by our planet's magnetic field that originate from the solar wind. Lastly, the regions of vanishing magnetic field between the closed day-side field lines and those that are swept by the solar wind towards the magnetotail are called *polar cusps*. Despite their name, they are not located exactly at the poles, but at lower geomagnetic latitudes ($\approx 78^\circ$), and particles from the solar wind can freely enter the magnetosphere here. These are the only regions that connect the surface of the Earth to the magnetopause (Kallenrode 2004).

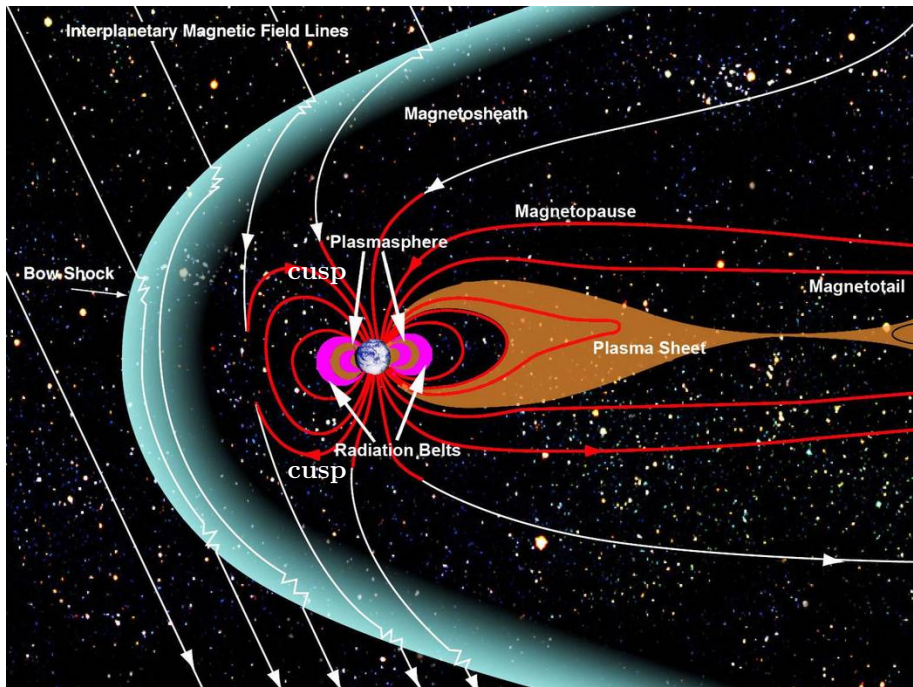


Figure 1.20: Schematic of Earth's magnetosphere and its components. The interplanetary and Earth magnetic field encounter, creating a bow shock and stripping away part of our day-side planet's magnetic field, while elongating it on the night-side to create the magnetotail. Between the bow shock and Earth's magnetic field edge (magnetopause) lies the magnetosheath, a region still filled with IMF and solar wind plasma. Close to Earth is the symmetric plasmasphere which embeds the radiation belts. Polar cusps form on the day-side, in the region between closed field lines and those stripped to the tail. Credit: NASA.

As seen in Figure 1.20, Earth's magnetic field is oriented from the South geographic pole to the North one, which correspond to the North and South magnetic poles, respectively. This is actually how compasses are able to point towards the poles, the south pole of the needle being attracted to the northern magnetic pole and vice-versa. When a magnetic structure arrives at Earth with a northward-directed magnetic field (oriented in the same direction as that of the Earth), it simply flows along Earth's magnetic field without triggering any severe effects.

However, the situation changes drastically when the incoming magnetic structure carries a strong negative (southward) B_z component. In this case, magnetic

reconnection is induced between the day-side magnetopause and the ICME (for instance), opening up field lines and dragging them towards the magnetotail. The field lines which were pulled to the night-side re-close via magnetic reconnection, pushing the particles trapped in the plasma sheet towards the Earth's polar regions. The motion of magnetic field and plasma during this entire process is described by the *Dungey cycle* (Dungey 1961). The particles heading towards our planet enhance the density of the *ring current* (Daglis et al. 1999) which creates an additional magnetic field in the opposite direction to that of the Earth, therefore weakening the total magnetic field. The ring current is an electric current flowing in the equatorial plane at a distance of about 3-8 R_E , clockwise as seen from the North Pole and is carried mainly by positive ions trapped in Earth's magnetosphere (e.g. Milan et al. 2017, and references therein). The strong fluctuations in Earth's magnetic field are called *geomagnetic storms* and can have dramatic effects on ground and space infrastructure. The charged particles entering the magnetosphere are also seen as the beautiful aurora events in the polar regions.

***Dst* index**

The term '(geo)magnetic storm' was introduced at the beginning of the 19th century by Alexander von Humboldt (1769-1859), a Prussian geographer, naturalist and explorer. He used it to describe a sudden decrease in the geomagnetic field's horizontal component measured at Earth's surface, after observing strong oscillations in compass orientation during an auroral event. Even though no two geomagnetic storms are identical, a pattern of three phases has been observed: the initial phase, the main phase and the recovery phase. Such a behavior has been observed in one of the many parameters used to describe the intensity of the geomagnetic storm, called the *disturbance storm time* (*Dst*) index (Sugiura & Kamei 1991). The *Dst* represents the hourly average of the deviation of the horizontal component of magnetic field, the measurements being taken from several ground stations located at mid to low latitudes. Therefore, it is an indication of the global variation in strength of the terrestrial dipole field. *Dst* is measured in units of nT, as it is a difference of two very weak magnetic field values. The lower (more negative) the measured values are, the stronger the storm is. The official values of *Dst* are provided by the World Data Center at Kyoto University ³.

Figure 1.21 shows a typical evolution of the *Dst* during a geomagnetic storm, exhibiting all three phases. The initial phase of the storm is described by an increase of the magnetic field, and occasionally a rapid positive change in *Dst*,

³<http://wdc.kugi.kyoto-u.ac.jp/dst/dir/>

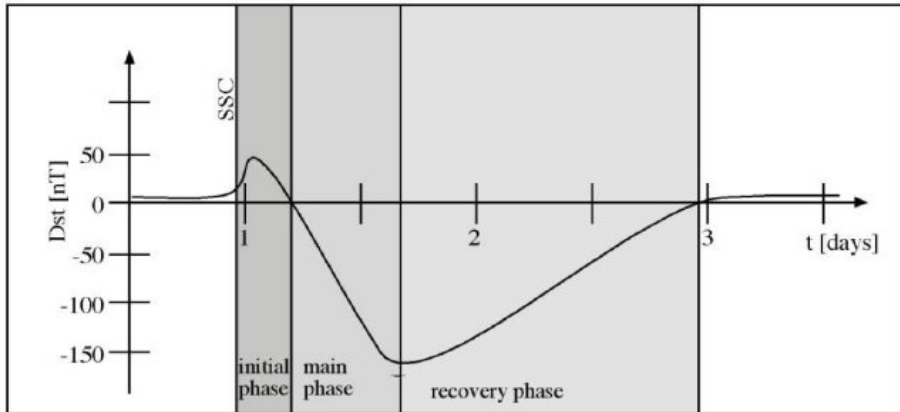


Figure 1.21: Typical evolution of the Dst index during an intense geomagnetic storm, exhibiting the three part structure: the initial phase, the main phase and the recovery phase. This particular storm also presents an initial strong increase in Dst , called storm sudden commencement (SSC). Credit: Kasran et al. (2018).

Table 1.1: Classification of geomagnetic storms as a function of Dst index, from Loewe & Prölss (1997).

Storm class	Dst_{min} range
weak	-30 to -50 nT
moderate	-50 to -100 nT
strong	-100 to -200 nT
severe	-200 to -350 nT
great	< -350 nT

called the storm sudden commencement (SSC; e.g., Mayaud 1975; Curto et al. 2007), but that is not always observed. The increase in Dst is due to the interplanetary shock wave compressing the solar wind ahead of it and creating a jump in the dynamic pressure, similar to plowing the snow. The main phase begins when the Dst values drop below zero and it ends when it reaches its minimum. The recovery phase is usually the longest one and is associated with the ring current decay, while the Dst and magnetic field values return to their original levels before the disturbance. Geomagnetic storms have been divided using the Dst index into several categories by Gonzalez et al. (1994) and Loewe & Prölss (1997), depending on their severity. The intervals of definition can be found in Table 1.1.

Since *Dst* is a good proxy for the strength of geomagnetic storms, many models have been developed with the goal of predicting this index from in situ measured values, and therefore the *geoeffectiveness* of CMEs. Some of the simplest ones take in consideration three main parameters obtained from the solar wind, the B_z component, the speed and the dynamic pressure. Even so, the results obtained by Burton et al. (1975) while using this model were quite accurate. A modified version of this simple model (O'Brien & McPherron 2000) has also been implemented in the current thesis and used to compute the *geoeffectiveness* of our simulated CMEs. More complex semi-empirical algorithms have been developed by Temerin & Li (2002) and Temerin & Li (2006), which take into account more variables that could contribute to the energy transfer from the solar wind to the magnetosphere.

In our technology-dependent society, improving the forecasting of ICME *geoeffectiveness* needs to be a priority of development, since a severe storm could have tremendous impact on our infrastructure if not foreseen, causing enormous amounts of monetary damage. This was the case for the storm on 12-14 March 1989, which made the power grid of Québec collapse within 90 seconds, causing millions of dollars of equipment damage (Medford et al. 1989; Bolduc 2002). A more recent example is SpaceX's 40 satellites that were forced to be decommissioned and taken out of orbit due to a minor to moderate geomagnetic storm occurring between 3-4 February 2022 ⁴.

1.4 Motivation and thesis goals

Given the limited amount of in situ observations close to the Sun and between Sun and Earth, it is difficult to assess the physical processes involved in the eruption and interaction of CMEs as they evolve and propagate away from the Sun. A better understanding of the evolution of CMEs can lead to a more accurate prediction of their arrival at Earth, which is definitely required in our current technology-dependent society.

This measurement gap can be filled using numerical simulations of CMEs, within the necessary approximations and initial hypotheses considered. In our work, we focused on several scientific questions, particularly how:

- Do shearing motions affect the subsequent eruptions?
- Do some stealth CMEs form? What parameters contribute to their eruption?

⁴<https://www.stce.be/news/573/welcome.html>

- Does the background wind/initial configuration affect the formation and evolution of CMEs?
- Do secondary eruptions affect the propagation and geoeffectiveness of the preceding CME?
- Do single eruptions interact with the background wind versus multiple eruptions?
- Does the force balance change during eruptions?
- Do different forces contribute to the eruption and propagation of CMEs?
- Are plasma blobs formed? Why do they appear only in certain configurations?

Answering all these questions lead us to a better understanding of the mechanisms involved in the eruption and propagation of CMEs. It also improved our knowledge of the resulting geomagnetic impact of single, but especially consecutive eruptions, proving the usefulness of numerical simulations and of the methods employed, in particular the decomposition of the forces.

Chapter 2

CME modeling

*“The machine does not isolate man
from the great problems of nature
but plunges him more deeply into them.”
– Antoine de Saint-Exupéry*

Summary

In this Chapter we provide an introduction to the core concepts and numerical tools used in this thesis to create and propagate CMEs until Earth. We first introduce the fourth fundamental state of matter, plasma, and its approximations in the astrophysical context. We then describe from physical and mathematical points of view the magnetohydrodynamics (MHD) theory used to characterize the evolution of such plasmas. The constraints needed for this theory to be applied are also detailed, in the frame of ideal MHD and macroscopic plasmas. Finally, we present MPI-AMRVAC, the code used to numerically simulate all the solar eruptions discussed in the next Chapters.

2.1 Introduction to plasma physics

The term *plasma* has been extensively used throughout the introduction of this thesis, but what is it exactly? Plasma is the fourth fundamental state of matter, and is found not only in an astrophysical context. Lightning, the inside of fluorescent bulbs, aurorae and fire are all made of plasma, albeit different types of it and at different temperatures. Plasma is usually associated to an

electrically conducting gas, but it is fundamentally different from it due to the electromagnetic interactions between the composing charged particles. In this thesis, we use the macroscopic (fluid) definition of plasma, which is *an electrically neutral substance containing many interacting free electrons and ions which exhibit collective behavior due to the long-range Coulomb forces* (Goossens 2003).

The first approximation that is taken into account when describing a macroscopic plasma is the size of the analyzed volume. The length scale of such a system (L) needs to be large enough to be able to statistically affirm that on average, the plasma considered is *quasi-neutral*. This condition is satisfied when ⁵:

$$L \gg \lambda_D, \quad (2.1)$$

where λ_D is a characteristic length and is called the *Debye length*:

$$\lambda_D = \left(\frac{\epsilon_0 k_B T}{n e^2} \right)^{1/2}, \quad (2.2)$$

where ϵ_0 is the vacuum permittivity, k_B is the Boltzmann constant, T and n are the temperature and number density of the fluid plasma, and e is the charge of an electron. The Debye length is the distance beyond which the electrostatic field of a charged test particle is shielded by the surrounding particles of opposite charges. This means that the charge of a proton, for instance, placed in the center of a shell of electrons, will not be ‘felt’ outside a sphere of radius λ_D , called the *Debye sphere*. Typically, λ_D has a value of 0.07 m in the solar corona, and 10 m at 1 AU. Since the range of our simulations spans several R_\odot , this condition is easily satisfied.

Since we don’t live in a static world, never having reached 0 K when theory predicts that all particle motions cease, space is experienced also through time. Therefore, the next logical condition following length is time. Plasma particles oscillate at different frequencies, and it is intuitive that large and heavy ions oscillate at lower frequencies than light electrons. As a consequence, the oscillation frequency of the plasma (ω_p) will be approximately the same as that of the electrons ($\omega_{p,e}$):

$$\omega_p \approx \omega_{p,e} = \left(\frac{n_e e^2}{m_e \epsilon_0} \right)^{1/2}, \quad (2.3)$$

⁵All equations presented in this chapter are expressed in SI units.

where n_e is the electron number density and m_e is the electron mass. Due to their greater mobility, electrons will reorganize themselves in order to restore any imbalance in charge distribution that might occur, such that the quasi-neutrality of the plasma is maintained. This brings us to the temporal constraint, meaning that the system can be electrically neutral only if electrons are allowed to redistribute around the ions, so the time spans of analysis (τ) need to be sufficiently longer than the plasma (or electron) oscillation period:

$$\tau \gg 2\pi/\omega_{p,e}. \quad (2.4)$$

Assuming a typical coronal electron density of 10^{15} m^{-3} , the plasma oscillation period has then an order of magnitude of 10^{-9} s (nanoseconds), which is much smaller than the time-scales analyzed in this thesis, therefore this temporal requirement is met.

The final condition is related to the first spatial one. In order to have a statistically and averaged neutral plasma, not only a significant length is required, but also a particle density such that there are enough interactions for the collective behavior to manifest. This translates in the following condition:

$$N_D \gg 1, \quad (2.5)$$

where N_D is the number of particles inside the Debye sphere. Since $N_D = 1.4 \times 10^9$ in the solar corona, this condition is also easily satisfied for the system simulated and investigated in this thesis.

Strictly speaking, some of the previous conditions are not met in the solar wind environment near Earth, but since kinetic and particle simulations are a lot more computationally demanding, plasma simulations are still employed and widely used for this region. Even with the violation of some of these approximations, plasma simulations still provide a fairly accurate representation of the solar wind-CME system at 1 AU.

2.2 Ideal magnetohydrodynamics theory

The dynamics and evolution of macroscopic plasma is well described by the set of equations in the *magnetohydrodynamics* (MHD) theory, which combines the equations of fluid dynamics with Maxwell's equations. Their complete derivation can be found in the book of Goedbloed & Poedts (2004). In this thesis we used a modified version of the *ideal* MHD, which assumes some more

approximations apart from the previously discussed plasma ones. They are listed as follows:

- Non-relativistic plasma ($v \ll c$, where v is the speed of plasma and c the speed of light in vacuum);
- Fully ionized plasma, which implies that all electrons are free and are no longer bound to the nucleus ;
- Single-fluid plasma, meaning that the particle species behave as one fluid;
- All dissipative processes (finite viscosity, electrical resistivity and thermal conductivity) are neglected, and perfect conductivity is assumed.

All these approximations might seem quite constraining, but they give a pretty reliable description of plasma stability, force balance and dynamics on large scale systems. They also simplify computations and reduce simulation time, as well as minimize the resources (processors) required to run such simulations. After taking them into consideration, the simplified following equations are obtained, that represent the core mathematical description of ideal MHD (Goedbloed & Poedts 2004):

1. Continuity equation (or mass conservation):

$$\frac{\partial \rho}{\partial t} + \nabla \cdot (\rho \mathbf{v}) = 0, \quad (2.6)$$

2. Momentum equation:

$$\rho \left(\frac{\partial \mathbf{v}}{\partial t} + \mathbf{v} \cdot \nabla \mathbf{v} \right) + \nabla p - \rho \mathbf{g} - \frac{1}{\mu_0} (\nabla \times \mathbf{B}) \times \mathbf{B} = 0, \quad (2.7)$$

3. Pressure equation:

$$\frac{\partial p}{\partial t} + \mathbf{v} \cdot \nabla p + \gamma p \nabla \cdot \mathbf{v} = 0, \quad (2.8)$$

4. Induction equation:

$$\frac{\partial \mathbf{B}}{\partial t} - \nabla \times (\mathbf{v} \times \mathbf{B}) = \frac{\partial \mathbf{B}}{\partial t} + \nabla \cdot (\mathbf{v} \mathbf{B} - \mathbf{B} \mathbf{v}) = 0, \quad (2.9)$$

where ρ is the mass density, t is time, \mathbf{v} is the velocity, p is the pressure, \mathbf{g} is the gravitational acceleration (of the Sun in our case), μ_0 is the vacuum

permeability, \mathbf{B} is the magnetic field, and γ is the adiabatic index for an ideal gas. In Equation 2.7, Ampère's law defines $(\nabla \times \mathbf{B})\mu_0^{-1}$ as the electrical current density \mathbf{j} , so the last left-hand side term can be written as $\mathbf{j} \times \mathbf{B}$, which represents the Lorentz force (see Section 2.3).

The first equation (2.6) basically states that the rate of increase of mass (density) in a control volume has to be equal to the net influx of mass. So the mass input needs to be the same as the output, with no accumulation, which describes the 'fluid part' of the plasma. The second equation (2.7) described the motion of plasma, considering all the stress factors acting upon it. The third equation (2.8) can be re-written in terms of the conservative variable of total energy density as such:

$$\frac{\partial}{\partial t} \underbrace{\left(\frac{1}{2}\rho v^2 + \rho e + \frac{B^2}{2\mu_0} \right)}_{\text{total energy density}} + \nabla \cdot \left[\left(\frac{1}{2}\rho v^2 + \rho e + p + \frac{B^2}{\mu_0} \right) \mathbf{v} - \mathbf{v} \cdot \frac{\mathbf{B}\mathbf{B}}{\mu_0} \right] = -\rho \mathbf{v} \cdot \mathbf{g}, \quad (2.10)$$

where e is the internal energy. The total energy density is the sum of the kinetic, internal and magnetic energy densities, with $\rho e = p(\gamma - 1)^{-1}$.

The final equation (2.9) in its middle form states that the magnetic field variation needs to be equal and of opposite sign to the conversion of mechanical energy into electromagnetic induction. If we apply this to a magnetic flux through a surface element $d\Psi = \mathbf{B} \cdot d\boldsymbol{\sigma}$, and express the induction equation in total derivative terms, we obtain the *frozen-in condition*:

$$\Psi = \int_C \mathbf{B} \cdot \mathbf{n} d\sigma = \text{const}, \quad (2.11)$$

where σ is a surface element bounded by the curve C , and \mathbf{n} is the normal to the magnetic field. This equation has several physical implications:

- *The magnetic flux through a surface moving with the plasma is conserved;*
- *Magnetic field lines behave as if they move with the plasma* (Priest 2014), hence the name of the equation;
- Magnetic topology is conserved.

Magnetic monopoles have never been observed or created. Therefore, in addition to these four core equations, the magnetic field also needs to satisfy a final

divergence-free condition, meaning that there cannot be any magnetic sinks or sources:

$$\nabla \cdot \mathbf{B} = 0. \quad (2.12)$$

As mentioned before, even though all these conditions might seem quite restrictive, they accurately describe the evolution of the solar wind and CMEs, the topics of interest for this thesis. However, ideal and simply MHD in general cannot be applied to study systems where non-fluid or kinetic effects are important, such as particles for which the distribution functions are not Maxwellian (e.g. cosmic rays). MHD is also not applicable for weakly ionized or small scale plasmas where kinetic approaches (sometimes in combination with MHD) are commonly used (e.g. Wijsen et al. 2021; Schwadron et al. 2014; van der Holst et al. 2010; Li et al. 2021).

2.3 Forces governing the dynamics of CMEs

Coronagraph observations suggest that many CMEs appear to have a helical structure, which was attributed to the existence of flux ropes in the magnetic structure of CMEs. Their presence can also be inferred from in situ measurements, occurring usually in magnetic clouds. Flux ropes are bundles of magnetic field lines twisted around a central axis, and they are kept in equilibrium in the solar corona by the interplay between outward pushing forces (usually plasma and magnetic pressure gradients) and confining ones (magnetic tension and gravity). Normally the plasma density decreases almost radially away from the Sun, therefore denser regions will exert a force towards rarefaction regions, as seen in Figure 2.1, creating an outward plasma pressure gradient. The larger the difference in pressure between the two regions, the stronger the gradient will be. Similarly, if we replace the density with magnetic field (\mathbf{B}), a magnetic pressure gradient forms that is also pushing away from the Sun, from high to low values of \mathbf{B} (left panel of Figure 2.2). Since flux ropes are normally anchored on the Sun in two points of opposite polarity, they will have a curvature which is pointing towards the Sun. Much like a twig that is being bent, a force will appear that will try to straighten the field lines, pointed radially inward with respect to the curvature. This downward force is called the magnetic tension, and it can be visualized in the right panel of Figure 2.2. The sum of the magnetic pressure gradient and tension comprise what was previously mentioned as the *Lorentz force*. This force is perpendicular to \mathbf{B} , therefore any acceleration that occurs along the field lines can only be caused by the plasma pressure gradient or gravity.

For a more mathematical approach, let's return to the ideal MHD equations, particularly the momentum Eq. 2.7. The terms in the brackets actually comprise the full derivative of velocity in time ($\frac{d\mathbf{v}}{dt}$), i.e. acceleration. By moving all the other terms to the right-hand side and expressing the Lorentz force in its components, we obtain:

$$\rho \left(\frac{d\mathbf{v}}{dt} \right) = -\nabla p + \rho \mathbf{g} - \nabla P_B + \mathbf{T}_B, \quad (2.13)$$

which basically represents Newton's second law of motion for a fluid element!

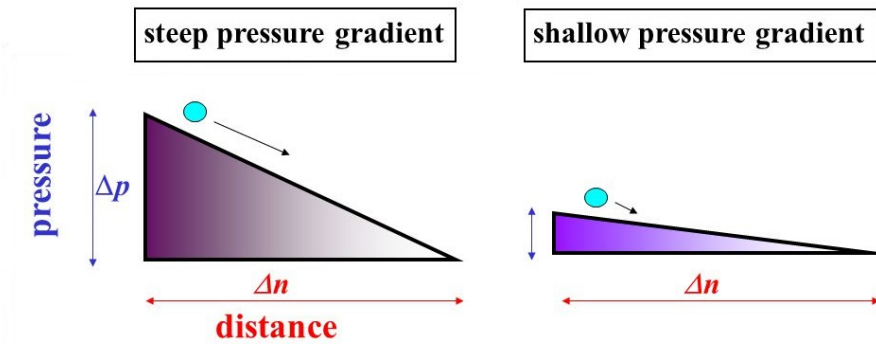


Figure 2.1: Schematic of either plasma or magnetic pressure gradient acting from high towards low pressure regions, and how their strength varies depending on the pressure difference.

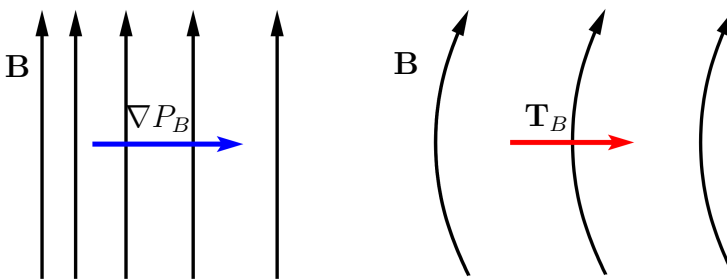


Figure 2.2: Schematic of magnetic field (\mathbf{B}) lines and magnetic forces acting on them. Left: Magnetic pressure gradient (∇P_B) going from regions of strong (closer lines) to weak magnetic field (spread out lines). Right: Magnetic tension (\mathbf{T}_B) acting towards the center of curvature of bent field lines.

The total force on the left-hand side, which is the usual mass (or density) times acceleration, equals the sum of all contributing forces, which are the plasma pressure gradient, gravity, the magnetic pressure gradient (∇P_B), and the magnetic tension (\mathbf{T}_B), with their corresponding signs. The last two terms are defined as follows:

$$\nabla P_B = \nabla \frac{|B|^2}{2\mu_0} \text{ and } \mathbf{T}_B = \frac{(\mathbf{B} \cdot \nabla)\mathbf{B}}{\mu_0}. \quad (2.14)$$

When the fine balance between all these forces is lost, flux ropes can erupt catastrophically, resulting in CMEs. Calculating all the different contributions is not an easy task when using observations, since we do not have access to in situ measurements from inside the solar corona, from which we could extract the required parameters. The remote-sensing observations provide limited information about the photospheric magnetic field and only approximate coronal density and temperature values. Numerical simulations, however, provide these variables and facilitate the analysis of individual forces that lead to the destabilization of coronal structures that erupt and create CMEs. Therefore, these computations are extensively employed in this thesis, in particular in Chapter 5, in an effort of better understanding solar eruptions and their triggering mechanisms.

2.4 MPI-AMRVAC code

The numerical simulations documented and analyzed in this thesis were performed using the Message Passing Interface - Adaptive Mesh Refinement - Versatile Advection Code (MPI-AMRVAC, Keppens et al. 2012; Porth et al. 2014; Xia et al. 2018). The name itself describes the code quite extensively, starting from MPI which is the technique that allows processors to exchange information and split the tasks during simulations, in order to perform parallel computations that reduce their usage time.

The AMR routines can be used on many levels to refine locally the grid on which the equations are solved, in order to increase the accuracy of the regions of interest, but to prevent fine resolutions in the entire domain which require extremely large processing times. Four different criteria can be used to trigger the refining or coarsening. The one employed in this thesis is user-defined, and is based on a parameter that is a proxy for current-carrying structures, in order to refine the regions where magnetic reconnection occurs, usually tracking the CME during its propagation. This particular method will be thoroughly described in Chapters 3 and 4. More generally, the simulation grid is made of

blocks that can be defined on any dimension by the user, in a hierarchically nested manner. The blocks and their respective ghost cells (cells of neighboring blocks) can be treated separately and simultaneously by different processors. In the case of 2D (or 2.5D) simulations, the block that meets the refining criteria, as is the case of block (3,2) in Figure 2.3, is split into four equal blocks. The subsequent blocks are also checked to see if they meet the requirement for refining, and if that happens, they are split again into four equal parts, as does block (6,4) of the same Figure. This process is repeated until the imposed maximum level of AMR is achieved, or when the criteria is no longer met.

The VAC part of the code's name refers to its extreme versatility, being capable of solving any set of differential equations of the type:

$$\partial_t \mathbf{U} + \nabla \cdot \mathbf{F}(\mathbf{U}) = \mathbf{S}_{phys}(\mathbf{U}, \partial_i \mathbf{U}, \partial_i \partial_j \mathbf{U}, \mathbf{x}, t), \quad (2.15)$$

where \mathbf{U} represents a set of conserved variables described by fluxes $\mathbf{F}(\mathbf{U})$, and possible physical source terms \mathbf{S} , placed in the location described by vector \mathbf{x} . This means that MPI-AMRVAC is a very generic code and it can be implemented in any astrophysical setting, with any dimensionality and vast applications, from hydrodynamics to resistive and relativistic MHD. The ideal MHD equations discussed in the previous Subchapters can all be expressed in this conservative form, with their respective source terms (such as gravity). In our case, we chose to apply the code on 2.5 dimensions (axisymmetric), which means that the grid is 2D, but all the variables have three vectors, with the third component being symmetrical. More particularly, the computations were performed in spherical coordinates (r, θ, ϕ) , and the values in the ϕ direction are the same all around the Sun. This decision was made based on the idea of performing a parametric study, which would require too much simulation time in 3D and would not be feasible for a large number of runs. However, 2.5D simulations provide more information and can include more physics than 2D, and are also suitable for multiple runs, therefore making them ideal for the topics of interest studied in this thesis.

(1,3)	(2,3)				
(1,2)	(2,2)	(5,4)	(11,8)(12,8)		
			(11,7)(12,7)		
		(5,3)	(6,3)		
(1,1)	(2,1)	(3,1)	(4,1)		

Figure 2.3: Example of a hypothetical grid of 4×3 blocks at initial base level, onto which are applied two levels of refinement. Blocks (3,2) and (6,4) meet the refinement criteria, so they are split into four subsequent blocks. Credit: Keppens et al. (2012).

Chapter 3

Numerical simulations of shear-induced consecutive CMEs

Abstract

It is widely accepted that photospheric shearing motions play an important role in the initiation of coronal mass ejections (CMEs). Even so, there are events for which the source signatures are difficult to locate, while the CMEs can be clearly observed in coronagraph data. These events are therefore called ‘stealth’ CMEs. They are of particular interest to space weather forecasters, since eruptions are usually discarded from arrival predictions if they appear to be back-sided, which means not presenting any clear low-coronal signatures on the visible solar disc as seen from Earth. Such assumptions are not valid for stealth CMEs since they can originate from the front side of the Sun and be Earth-directed, but their on-disc signatures remain undetected and can therefore trigger unpredicted geomagnetic storms. We numerically model and investigate the effects of shearing motion variations onto the resulting eruptions and we focus in particular on obtaining a stealth CME in the trailing current sheet of a previous ejection. We used the 2.5D magnetohydrodynamics (MHD) package of the code MPI-AMRVAC to numerically simulate consecutive CMEs by imposing shearing motions onto the inner boundary, which represents, in our case, the low corona. The initial magnetic configuration consists of a triple arcade structure embedded into a bimodal solar wind, and the sheared polarity inversion line is

found in the southern loop system. The mesh was continuously adapted through a refinement method that applies to current carrying structures, allowing us to easily track the CMEs in high resolution, without resolving the grid in the entire domain. We also compared the obtained eruptions with the observed directions of propagation, determined using a forward modeling reconstruction technique based on a graduated cylindrical shell (GCS) geometry, of an initial multiple coronal mass ejection (MCME) event that occurred in September 2009. We further analyzed the simulated ejections by tracking the center of their flux ropes in latitude and their total speed. Radial Poynting flux computation was employed as well to follow the evolution of electromagnetic energy introduced into the system. Changes within 1% in the shearing speed result in three different scenarios for the second CME, although the preceding eruption seems insusceptible to such small variations. Depending on the applied shearing speed, we thus obtain a failed eruption, a stealth CME, or a CME driven by the imposed shear, as the second ejection. The dynamics of all eruptions are compared with the observed directions of propagation of an MCME event and a good correlation is achieved. The Poynting flux analysis reveals the temporal variation of the important steps of eruptions. For the first time, a stealth CME is simulated in the aftermath of a first eruption, originating from an asymmetric streamer configuration, through changes in the applied shearing speed, indicating it is not necessary for a closed streamer to exist high in the corona for such an event to occur. We also emphasize the high sensitivity of the corona to small changes in motions at the photosphere, or in our simulations, at the low corona.

This chapter is based on the previously published paper D.-C. Talpeanu, E. Chané, S. Poedts, E. D’Huys, M. Mierla, I. Roussev, and S. Hosteaux (2020). "Numerical simulations of shear-induced consecutive coronal mass ejections". In: *Astronomy&Astrophysics*, Volume 637, id.A77, 10 pp. The text was adapted in this thesis manuscript for completeness. D.-C. Talpeanu performed the numerical simulations, the analysis of numerical and observational data, and prepared the manuscript.

3.1 Introduction

Coronal mass ejections (CMEs) are some of the most energetic solar events that expel magnetic field-loaded plasma into the interplanetary space. These events release energies of the order of 10^{32} ergs (e.g. Forbes 2000) and they leave the solar environment with speeds between 20 km s^{-1} and 2500 km

s^{-1} (Webb & Howard 2012). If headed towards Earth, CMEs can provoke serious geomagnetic disturbances, induce electrical currents in power grids, disrupt the global positioning system, and endanger the life of astronauts. One way of mitigating these effects is to forecast the arrival of the associated interplanetary coronal mass ejection (ICME) at our planet, by identifying its source, direction, and speed. If source signatures such as flares, filament eruptions, coronal dimmings, or extreme ultraviolet (EUV) waves are not clearly visible on the side of the Sun directed towards Earth, it is usually assumed that the event is backside. However, there have been reported cases of eruptions lacking clear source locations, which were still Earthward directed. These situations are extremely puzzling for space weather forecasters, since geomagnetic storms caused by such CMEs can occur unpredicted and can potentially cause disruptions. Ejections without clear low coronal signatures are referred to as ‘stealth’ CMEs and were first investigated by Robbrecht et al. (2009b). The authors attributed the absence of traces to the large lift-off height and concluded that a CME originating from above 1.4 solar radii (R_{\odot}) should not leave any associated dimming, hence creating a stealth eruption. Other studies reporting CMEs without low coronal signatures include those of Ma et al. (2010), D’Huys et al. (2014), Kilpua et al. (2014), and Nitta & Mulligan (2017). Most of the studies on such events agree on two of their prevalent properties: a small angular width, of mostly $< 60^{\circ}$, and low initiation and propagation speeds, which are usually below 300 km s^{-1} . Another study conducted by Alzate & Morgan (2017) used advanced image processing techniques and located sources for the eruptions presented in D’Huys et al. (2014), confirming the low kinetic energies observed so far. These results emphasize the issues faced by space weather forecasters, which are the need for better imaging instruments, continuous observations from different vantage points, and a better understanding of the causes of such problematic eruptions.

Whether CMEs have a clear source region is closely related to the eruption mechanism, the height of reconnection, the overlying magnetic field, the limitation of current instrument capabilities (Howard & Harrison 2013), and other solar atmospheric conditions. It is generally accepted within the solar community that photospheric shearing motions present one of the driving mechanisms for CMEs, as they increase the magnetic helicity and consequently, the free magnetic energy. Linker & Mikic (1995), Van der Holst et al. (2006, 2007), DeVore & Antiochos (2000), and Lynch et al. (2016) are just some examples of studies using numerical simulations with imposed shearing motions to obtain CMEs and investigate their dynamical properties, with their magnetic configurations ranging from the simplest 2.5D bipolar to full-Sun 3D multi-polar structures.

Proposed mechanisms for stealth CME initiation include streamer blowout (e.g.

Robbrecht et al. 2009b), empty filament channel eruption (e.g. Pevtsov et al. 2012), and coronal magnetic field reconfiguration, usually in the trailing current sheet of a first CME (e.g. Bemporad et al. 2012). We modeled and analyzed the latter type of event by means of shearing motions imposed at the lower boundary (low corona), and also focused on the effect of variation of the shear amplitude on the resulting eruptions.

It could be argued that this particular type of stealth events fits in the ‘plasma blobs’ category, as they originate in the current sheet created behind a first CME. These blobs were observed and analyzed by several authors, including Webb & Cliver (1995), Ko et al. (2003), and Webb & Vourlidas (2016), who reported such narrow structures flowing along the current sheets that form after fast CMES; these blobs were also numerically simulated by Riley et al. (2007). Whether these blobs can be called CMES or not is still a topic of debate, but their eruption mechanism is very similar, and therefore, for this study the distinction is not important.

This work is similar to that of Zuccarello et al. (2012) and Bemporad et al. (2012) owing to the initial magnetic configuration and shearing profile imposed, but the main difference is that we did not require a change in magnetic field strength to obtain the second eruption. Instead, small changes applied to the shearing speed resulted in the coronal magnetic field reconfiguration, creating the second stealthy CME. Furthermore, as opposed to having a fixed grid, we use an adaptive mesh refinement (AMR) routine that increases the resolution only in regions of interest, which are areas where the electrical current is enhanced.

3.2 Observations

The observational basis of this work consists of a multiple coronal mass ejections event (MCMEs; Bemporad et al. 2012) that occurred on 21-22 September 2009. The first CME (hereafter CME1) was associated with a western limb prominence eruption and originated from an approximate latitude of 37° south, as seen by SECCHI-Extreme UV Imager (EUVI; Wuelser et al. 2004) on board the STEREO-B spacecraft. Underlying the prominence was an active region at approximately 38° S and 15° W (as seen from Earth), although it did not have a NOAA number assigned. The ejected material left the EUVI field of view on 21 September, at around 19:37 UT, as seen in Fig. 3.1. The second CME (hereafter CME2) entered the COR1-B (Thompson et al. 2003; Howard et al. 2008) coronagraph field of view on 22 September 2009 at $\sim 04:05$ UT, almost eight hours after CME1. We investigated running difference images in different wavelengths and with different time steps, but we could not identify any plasma

motions that could be distinguished clearly from the background noise and that would indicate the origin of the second CME. Because of the difficulty of locating the source of CME2, the lack of obvious low coronal signatures, and the fact that it was visible only when reaching higher distances from the solar surface, we consider it a stealth CME. Even though it was fainter and narrower than CME1, CME2 propagated very similarly to the first event, originating from approximately the same coronal region and presenting a strong equatorial deflection. This behavior was explained and numerically simulated by Zuccarello et al. (2012). Their paper also contains a more detailed description of the eruptions and positions of STEREO-A and B spacecraft during the event. A preview of the spacecraft position with respect to the Sun and the planets can be seen in Figure 3.2.

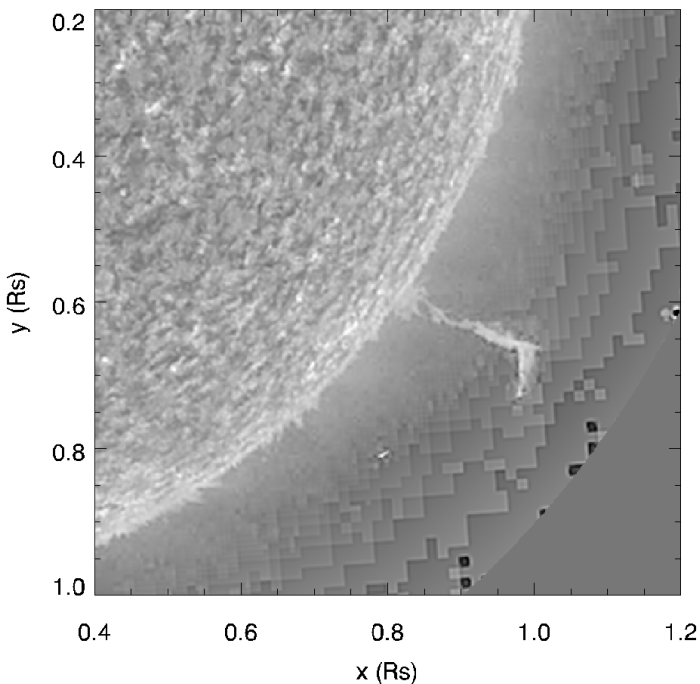


Figure 3.1: Image from STEREO-B EUVI (304) of the erupting prominence, taken on 21 September 2009, at 16:36UT. The image was scaled to enhance the prominence and a mask was applied from $1.35 R_{\odot}$ outwards to remove the large noise at the edges.

Bemporad et al. (2012) calculated the velocities of both CMEs within $4 R_{\odot}$ using height versus time maps ('ht-plots'), and obtained values below 164 km s^{-1} .

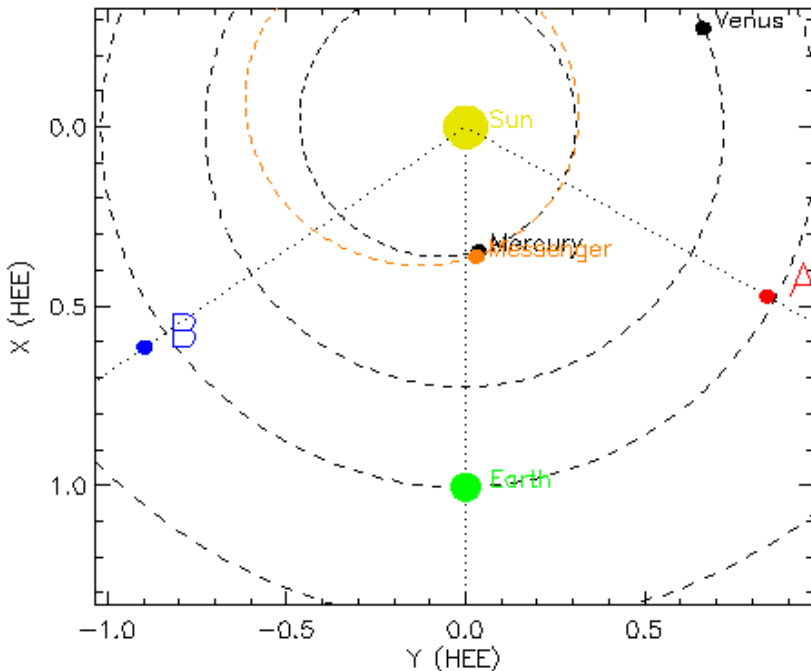


Figure 3.2: Location of the Sun, Mercury, Venus and Earth, and of STEREO-A, STEREO-B, and MESSENGER spacecraft on 22 September 2009 at 00:00 UT. Credit: NASA.

Since we were more interested in the direction of propagation of the two CMES after the deflection, we performed 3D reconstructions using the forward modeling technique higher in altitude (above $6 R_{\odot}$), in the COR2 field of view. The geometrical shape chosen for the CME fitting was the graduated cylindrical shell (GCS) model (Thernisien et al. 2006, 2009; Thernisien 2011) available as a SolarSoftWare (SSW) package⁶, which approximates the CME structure to a bent cylinder connected to the Sun by two cones, representing the CME front and its footpoints, respectively. The shape can be changed through six free parameters, which we adjusted such that the predefined configuration matches the eruption in white-light running difference images (Fig. 3.3 and 3.4). For a more accurate computation, the reconstruction was performed when the CMES were best seen in the observations, i.e. at two different times for CME1, and at three times for CME2. Table 3.1 shows the resulting longitude, latitude, and

⁶<http://www.lmsal.com/solarsoft/>

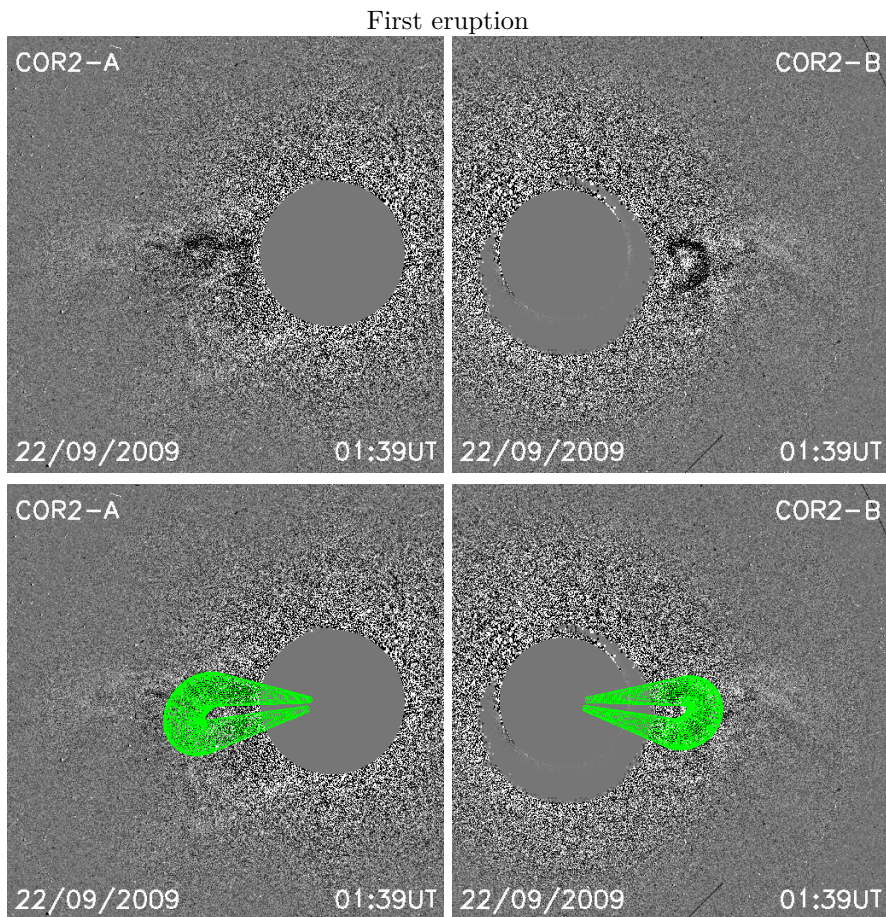


Figure 3.3: Top: Running difference images from COR2-A (left) and COR2-B (right) used in the GCS reconstruction model. Bottom: Reconstructions (green wire) using GCS superposed onto the upper corresponding panels in the case of CME1.

height in the Stonyhurst system of coordinates (Thompson 2006a). All five measurements were made for the same day, that is 22 September 2009.

The deprojected speed of a CME is mainly influenced by its longitude, which in this case had average values of 5.82°W for CME1, and 6.7°W for CME2. The smallest longitude value found for CME2 (5.6° , see Table 3.1) is probably due to errors from the reconstruction method and not a real variation. We previously measured the projected heights of the fronts of both CMEs in COR2-B plane of

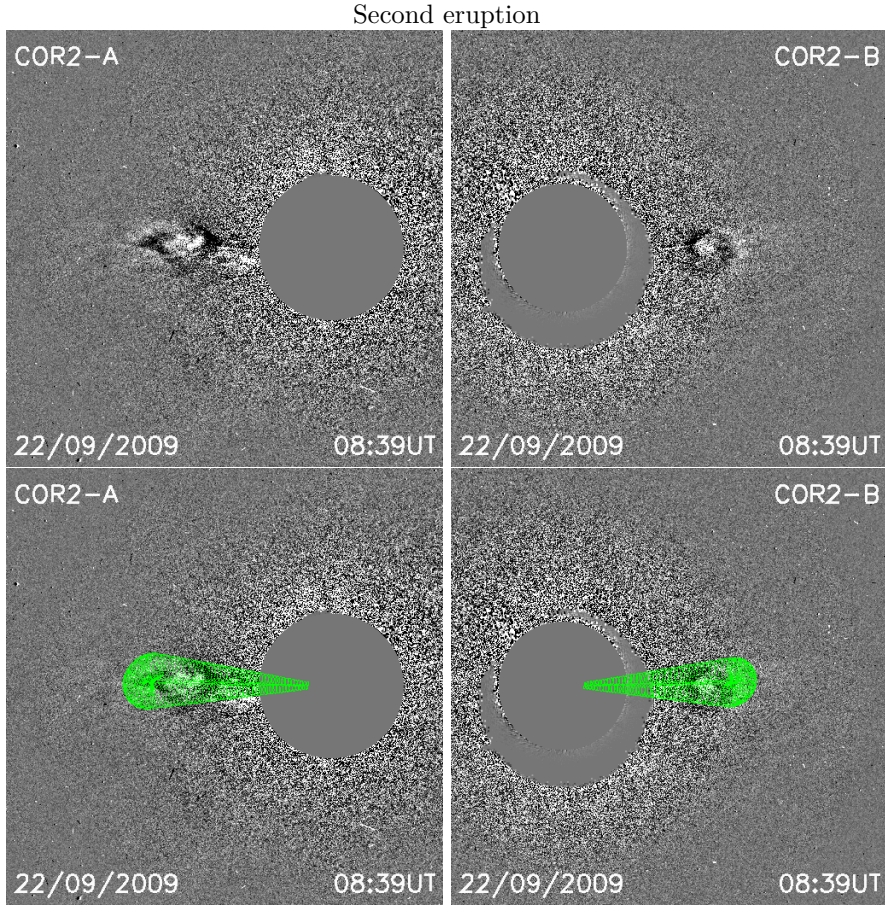


Figure 3.4: Same as Figure 3.3, but for CME2.

Table 3.1: Results from the GCS analysis.

Eruption	Hour	Long.	Lat.	Height/[R_{\odot}]
CME1	01:39 UT	6.1°	2.2°	6.9
	02:39 UT	5.6°	2.8°	7.6
CME2	07:54 UT	6.7°	7.8°	6.9
	08:39 UT	5.6°	7.8°	8.4
	12:24 UT	7.8°	5.6°	14.5

sky, when the angle between STEREO-B and the Sun-Earth line was -55.6° . We thus computed the deprojected distances of both CME fronts from the Sun center. We plotted the deprojected height of the CME1 leading edge as a function of time from $6.3 R_\odot$ to $16.7 R_\odot$ (see Fig. 3.5) and fitted the data with a first order polynomial, resulting in a deprojected velocity of $257 \pm 69 \text{ km s}^{-1}$. This speed is higher than 164 km s^{-1} measured in the low corona within $4 R_\odot$, and this acceleration above $6 R_\odot$ is also seen in the automated CACTus CME list (Robbrecht et al. 2009a) based on COR2-B observations, where the velocity is listed as 277 km s^{-1} . As seen in the ht-plot, CME2 was faster and propagated in the same field of view with a deprojected velocity of $349 \pm 70 \text{ km s}^{-1}$, mainly because it was expelled into a depleted solar wind following the passage of CME1. Given these slow speeds, a good assumption would be that the CMEs eventually reached the slow solar wind speed (as seen in Fig. 3.6) due to the drag force exerted on them. The error bars in Fig. 3.5 were calculated by selecting the CME front several times and extracting the largest variation between measurements. We computed the standard deviation in speed using the `derivsig.pro` function available in IDL, based on the height and time measurements and their error bars. The function computes the speed uncertainty values from the errors in height using an error propagation formula.

In order to obtain the speed of the wind into which the CMEs were ejected, we used the in-situ measured solar wind speed as extracted from NASA/GSFC's OMNI data set through OMNIWeb⁷ between 3 to 8 days after the eruption. This parameter is needed as input for the simulations described in Section 3.3. In this time interval, we carried out a back-calculation for each OMNI speed measurement to find the date and time at which the embedded CMEs should have originated from the Sun, in the assumption they had approximately the same velocity as the solar wind. We then compared this with the real eruption time and concluded the arrival time of the CMEs should be 27-28 September, as indicated by the red vertical lines in Fig. 3.6. In this period, the solar wind speed did not present any major jumps, as expected owing to the low speeds of the CMEs, and had an average value of $\approx 330 \text{ km s}^{-1}$. The small jump in speed on 26 September at 13:00 is not correlated to any other in situ ICME signature and this jump also arrived too early, therefore it was not considered to be the beginning of the ICME. We performed a more detailed study of other solar wind parameters as well, such as magnetic field components, to determine the arrival of the discussed CMEs at Earth, and this topic is the focus of the next Chapter.

⁷<https://omniweb.gsfc.nasa.gov/>

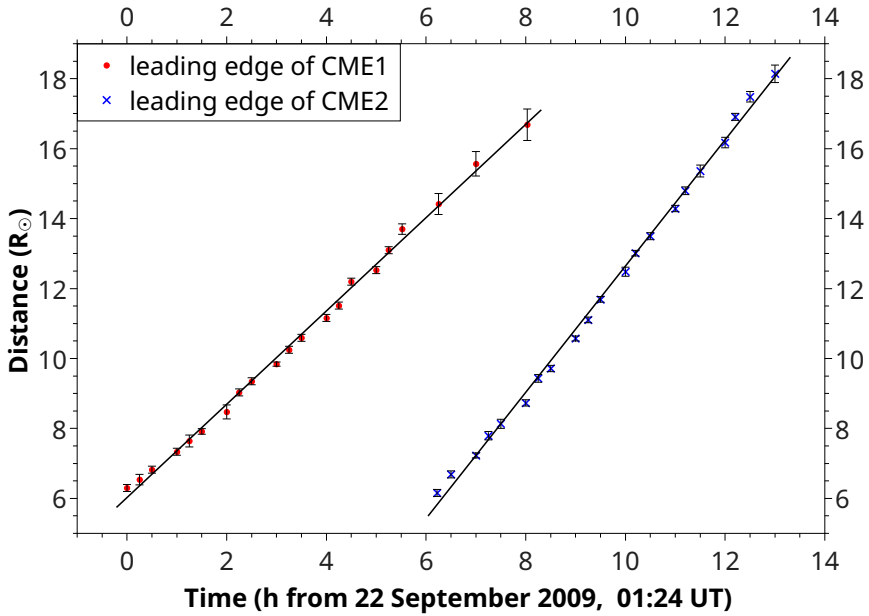


Figure 3.5: Height-time plots of the two studied CMEs, erupting between 21-22 September 2009, based on STEREO-B coronagraph observations.

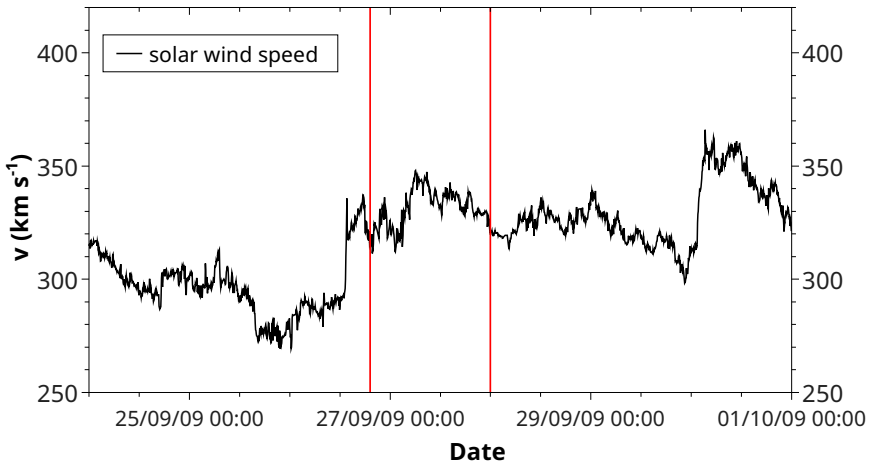


Figure 3.6: Solar wind speed recorded at Earth, taken from the OMNI database. The two red lines indicate the expected arrival time interval of the two CMEs.

3.3 Simulations set-up and method

Our goal was to investigate the effect of variations in the amplitude of shearing motions on the dynamics of CMEs, starting from the observed event discussed in Section 3.2. For this purpose, we performed 2.5D spherical axisymmetric numerical simulations using the code MPI-AMRVAC. The mesh has an initial resolution of 480×240 cells and the domain spans between the north and south poles of the Sun, and the Earth, that is $(r, \theta) \in [1, 215] R_{\odot} \times [0^{\circ}, 180^{\circ}]$, where r is the radial distance from the center of the Sun and θ is the heliographic colatitude. Even though the grid extends until 1 AU, in this study we only focused on the near-Sun region, below $20 R_{\odot}$. The propagation of the simulated CMEs to Earth is discussed in the next Chapter. In order to achieve much better detail of the dynamics of the eruption and of the structures that form, without increasing the resolution of the entire domain, an AMR protocol was used. The grid was refined to a maximum of two additional levels and only in the regions of interest, where the electrical current presented an enhancement, that is at potential magnetic reconnection sites. This increase is quantified through a parameter taken from Karpen et al. (2012) and also used by Hosteaux et al. (2018) as follows:

$$c \equiv \frac{|\iint_S \nabla \times \mathbf{B} \cdot d\mathbf{a}|}{\oint_C |\mathbf{B} \cdot d\mathbf{l}|} = \frac{|\oint_C \mathbf{B} \cdot d\mathbf{l}|}{\oint_C |\mathbf{B} \cdot d\mathbf{l}|} = \frac{|\sum_{n=1}^4 B_{t,n} l_n|}{\sum_{n=1}^4 |B_{t,n} l_n|}, \quad (3.1)$$

where $B_{t,n}$ represents the tangential component of the magnetic field along the segment l_n . The line integral at the numerator is obtained by applying the Stokes' theorem on the surface integral in the left hand-side term, and in this case the curve (contour) and the surface are those of a grid cell. In their discrete form, the line integrals are rewritten as the sum of the product between the tangential magnetic field and the length of the edges, along all four sides of a cell. Therefore, c is simply the ratio of the magnitude of the electrical current passing through the surface S spanning loop C to the sum of the absolute value of all of its components. In this definition, the parameter c varies from 0 to 1, depending on the non-potentiality of the magnetic field. The blocks of the grid are refined if and where c crosses a certain threshold, which we chose as $c > 0.02$. On the other hand, if $c < 0.01$, the grid is coarsened to a lower level, since there are no strong current-carrying structures in that region. In between these two values, the AMR routine does not impose any constraints, so the grid retains its resolution from previous time steps. The refinement is also fixed to a maximum number of two levels (on top of the base grid) for distances below $2.5 R_{\odot}$ and for $\theta \in [27^{\circ}, 153^{\circ}]$, such that there is no change in diffusivity close to the boundary, which would have affected the eruption dynamics and introduced

artificial phenomena. Because of the stretching of the grid, the scale of cells is kept constant, and the size ratio of the widths (or heights) of the farthest to closest cells to the inner boundary is ≈ 215 for the same mesh refinement level.

The MHD equations are temporally discretised using a two-step predictor corrector, which is suitable for a finite-volume discretisation method called the total variation diminishing Lax-Friedrichs (TVDLF) scheme. We used the most diffuse and stable type of slope limiter, minmod, and a Courant-Friedrichs-Lewy (CFL) number of 0.3. The magnetic field solution is kept divergence free using the generalized Lagrange multiplier method (GLM; Dedner et al. 2002), which introduces a new variable into the system, that dampens and transports the unphysical magnetic monopoles outside the computational domain.

The initial conditions (at the start of shear) consist of a realistic bimodal solar wind created by introducing extra source terms to the momentum and energy equations to account for gravity and heating mechanisms. This solar wind model is similar to that used in previous studies by Jacobs et al. (2005), Chané et al. (2006), Chané et al. (2008) and Hosteaux et al. (2019). The volumetric heating function was initially used by Groth et al. (2000) and Manchester IV et al. (2004), and takes the following empirical form:

$$Q = \rho q_0 (T_0 - T) \exp \left[-\frac{(r - 1R_\odot)^2}{\sigma_0^2} \right], \quad (3.2)$$

where ρ is the mass density, the amplitude of the volumetric heating $q_0 = 10^6$ ergs $\text{g}^{-1} \text{s}^{-1} \text{K}^{-1}$, r (R_\odot) is the distance from the center of the Sun, and T (K) is the temperature. The values T_0 (K) and σ_0 (R_\odot) represent the target temperature and the heating scale height, respectively, and these are both dependent on the value of a critical angle, θ_0 (measured from the North pole), as follows: from θ_0 equator-ward, $T_0 = 1.32 \times 10^6$ K and $\sigma_0 = 4.5 R_\odot$, and from θ_0 pole-ward, $T_0 = 2.3 \times 10^6$ K and $\sigma_0 = 4.5[2 - \sin^2(\theta)/\sin^2(\theta_0)] R_\odot$. To better reproduce the slow/fast solar wind features, θ_0 is also defined with a distance dependence as follows:

- $\sin^2(\theta_0) = \sin^2(17.5^\circ) + \cos^2(17.5^\circ)(r - 1R_\odot)/8R_\odot$, for $r < 7 R_\odot$,
- $\sin^2(\theta_0) = \sin^2(61.5^\circ) + \cos^2(61.5^\circ)(r - 7R_\odot)/40R_\odot$, for $7 R_\odot \leq r < 47 R_\odot$,
- $\sin^2(\theta_0) = 1$, for $47 R_\odot \leq r$.

The temperature and mass density are fixed at the inner boundary to 1.32×10^6 K and $1.66 \times 10^{-16} \text{g cm}^{-3}$, respectively. The temperature value at the

boundary is chosen based on the impact it has on the solar wind speed through the momentum equation, provided that the observed speed at Earth was $\approx 330 \text{ km s}^{-1}$ (as discussed in Section 3.2). Therefore, the temperature is adjusted to provide a realistic slow solar wind speed at Earth of $\approx 330 \text{ km s}^{-1}$, and a fast solar wind speed at the poles of $\approx 735 \text{ km s}^{-1}$. The radial component of the momentum is extrapolated in the ghost cells, while the latitudinal component (v_θ) is set to 0 at the boundary. The azimuthal component (v_ϕ) is set such that it resembles the differential rotation of the Sun. In order to introduce a dipole field, the term $r^2 B_r$ is fixed at the inner boundary, while $r^5 B_\theta$ and B_ϕ are extrapolated from the first inner cell. At the outer supersonic boundary, the variables $r^2 \rho$, $r^2 \rho v_r$, ρv_θ , $r v_\phi$, $r^2 B_r$, B_θ , $r B_\phi$, and T are continuous as well.

A commonly encountered magnetic field structure on the Sun depicts a triple arcade system embedded in a helmet streamer (see Fig. 3.7), which was also simulated by Bemporad et al. (2012) and Zuccarello et al. (2012) to study the deflection and dynamics of the chosen multiple event, and by Karpen et al. (2012) to analyze a breakout event. We applied the same configuration in our model, by taking the curl of the following vector potential:

$$A_\phi = \frac{A_0}{r^4 \sin \theta} \cos^2 \left[\frac{180^\circ(\lambda + 11.5^\circ)}{2\Delta a} \right], \quad (3.3)$$

through which we obtained the magnetic field components

$$B_r = \frac{A_0}{r^5 \sin \theta} \frac{180^\circ}{\Delta a} \cos \left[\frac{180^\circ(\lambda + 11.5^\circ)}{2\Delta a} \right] \sin \left[\frac{180^\circ(\lambda + 11.5^\circ)}{2\Delta a} \right], \quad (3.4)$$

$$B_\theta = \frac{3A_0}{r^5 \sin \theta} \cos^2 \left[\frac{180^\circ(\lambda + 11.5^\circ)}{2\Delta a} \right], \quad (3.5)$$

where $\Delta a = 37.2^\circ$ represents half the width of the arcade system, $\lambda = 90^\circ - \theta$ the solar latitude, $A_0 = 0.73 \text{ G} \cdot R_\odot^5$, and the whole arcade system is shifted by 11.5° to the south. These components were only added to the dipole magnetic field in the region determined by the latitude $\lambda \in [-48.7^\circ, 25.8^\circ]$. This configuration provides a polar magnetic field strength of 1.8 G (or $1.8 \times 10^5 \text{ nT}$), and a maximum arcade strength of 1.57 G (or $1.57 \times 10^5 \text{ nT}$), measured at the first cell of the domain.

Once the solar wind has reached a steady-state solution after $\approx 200 \text{ h}$, CMEs are obtained by applying time-dependent shearing motions at the inner boundary,

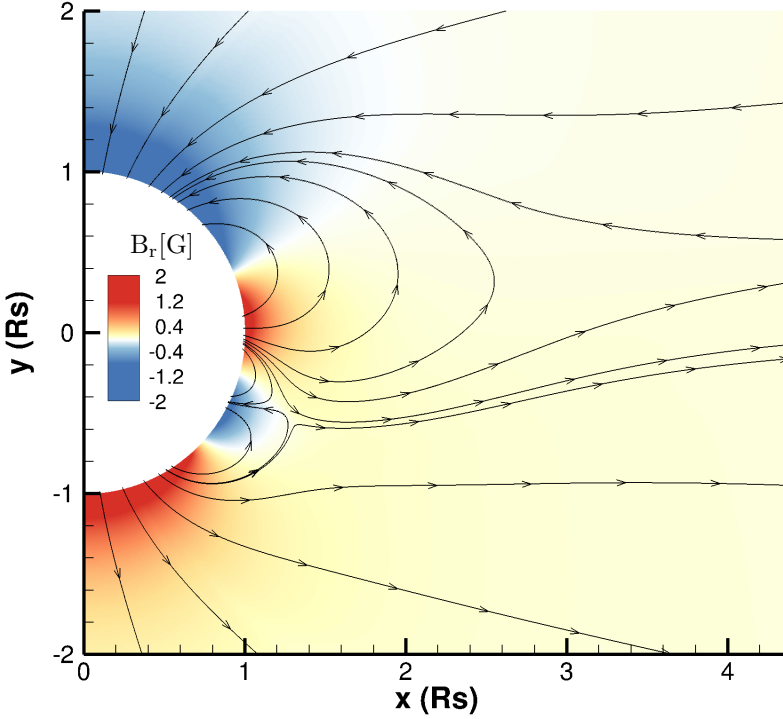


Figure 3.7: Initial magnetic field configuration - B_r (color scale) and selected magnetic field lines in the meridional plane.

thus magnetically stressing the corona above the selected region. The shear was introduced through the following additional azimuthal component of the speed:

$$v_\phi = v_0(\alpha^2 - \Delta\theta^2)^2 \sin \alpha \sin[180^\circ(t - t_0)/\Delta t], \quad (3.6)$$

where $\alpha = \lambda - \lambda_0$. This flow is almost symmetric with respect to the latitude of the southernmost polarity inversion line, which is approx. $\lambda_0 = -41^\circ$, and spans over $2\Delta\theta = 17.2^\circ$. It is applied for $\Delta t = 16$ h starting from $t_0 = 0$ h and it has a slow increase and decrease, with a maximum at half the time interval. Throughout the simulations, the scaling factor v_0 is given such that v_ϕ does not exceed 10% of the local Alfvén speed. A representation of the shearing profile can be seen in Figure 3.8.

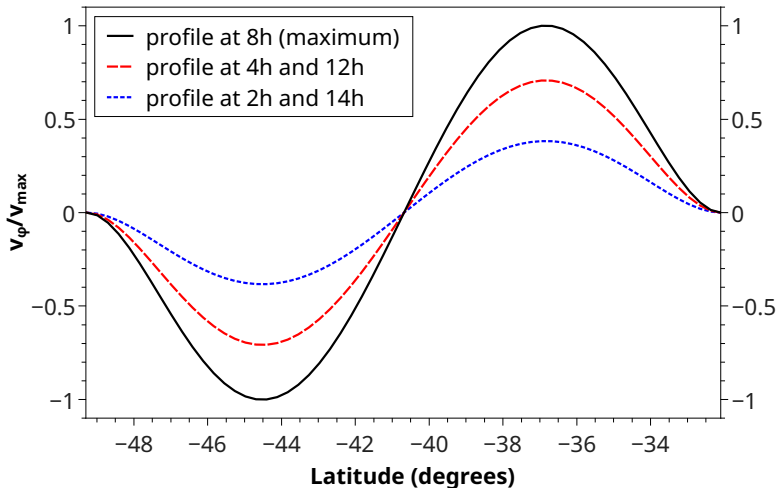


Figure 3.8: Normalized shearing profile (v_ϕ/v_{max}) as a function of latitude, at different simulation times from the start of shear.

3.4 Results

In order to make the system erupt, we applied shearing motions to the southernmost polarity inversion line and modified the amplitude of the shear by adjusting the scaling factor v_0 . Thus, a first erupting flux rope (CME1) is created approximately 8 h after the start of the shear (see Figures 3.9a,b,c), and its evolution and propagation are mostly independent of the small variations we impose on v_0 , as seen in Figures 3.10c,e,g. On the other hand, for the second and third flux ropes, changes within 1% of the initial lowest shearing speed (measured at the first cell of the domain) result in three different dynamical scenarios:

1. The double eruption case where $|v_\phi^{max}| = 37.4 \text{ km s}^{-1}$. After the first CME, a second flux rope also erupts (CME2) from the shear applied at the boundary (see Figures 3.9d,e,f and 3.10c,d).
2. The stealth eruption case, where $|v_\phi^{max}| = 37 \text{ km s}^{-1}$. After the first CME, the second flux rope (FR2) created from the shearing motions falls back to the Sun (Fig. 3.9g,h,i); a third flux rope emerges from the reconfiguration of the coronal magnetic field (Fig. 3.9j,k,l) and erupts in the trail of the preceding eruption (see Fig. 3.10e,f).

3. The failed eruption case, where $|v_\phi^{max}| = 37.2 \text{ km s}^{-1}$. After the first CME, the second flux rope (FR2) created from the shearing motions falls back to the Sun (Fig. 3.9g,h,i); a third flux rope emerges from the reconfiguration of the coronal magnetic field (Fig. 3.9m,n,o) and reconnects with the northern closed arcade, thus not erupting (Figures 3.10g,h).

Values of $|v_\phi^{max}|$ below the smallest or above the largest values of those mentioned result in only one eruption, or multiple eruptions, respectively, with the stealth occurring solely in the threshold specified. The amplitude of the applied shear is larger than the observed photospheric motions, which have typical speeds of around 5 km s^{-1} (Manchester 2007; Malherbe et al. 1983) and usually lead to flux rope formation, system destabilization, and eventually eruption. Nevertheless, our simulated inner boundary describes the low coronal environment, and the observed magnitude of the shearing speed increases with height in the solar atmosphere, as shown by Athay et al. (1982, 1985) (transition region: 20 km s^{-1}) and by Chae et al. (2000) (low corona: $20\text{--}50 \text{ km s}^{-1}$). Therefore, the amplitude of our imposed shear flow is in agreement with the computed velocities from coronal observations. Initially, Zuccarello et al. (2012) and Bemporad et al. (2012) applied the shear for 36 h in their simulations; this duration was calculated based on observed photospheric motions. In order to save computation time and resources, in this work we decrease the time interval during which the additional v_ϕ is applied from 36 h to 16 h, the latter being the value used in the discussed cases. This leads to an increase in the shear magnitude, but with almost no effect on the simulated eruptions.

In all three cases listed above, the formation of the first flux rope and its eruption are essentially the same. Firstly, the applied azimuthal flow increases the magnetic pressure inside the southern arcade, making it rise and expand. Secondly, the imbalance between the magnetic pressure gradient and tension compresses the magnetic field locally. This triggers reconnection between the sides of the arcade (white circle, Fig. 3.9b) and creates the flux rope, which is deflected towards the equator owing to the southern polar magnetic pressure (Fig. 3.9a,b,c), and propagates radially inside the current sheet of the northern helmet streamer approximately after $5 R_\odot$ (Fig. 3.10). For a more detailed view of the evolution, supporting videos for all three simulations and of the observed eruptions are available online⁸. In the simulation movies, extra flux ropes can be seen in the wake of the CMEs, and these flux ropes are somewhat comparable to those appearing in the coronagraph observations, but the occurrence of these is highly influenced by the initial coronal magnetic field configuration and the background solar wind. The magnetic configuration simulated is surely more simplified than the real configuration, and the solar wind is only adjusted such

⁸<https://www.aanda.org/articles/aa/olm/2020/05/aa37477-20/aa37477-20.html>

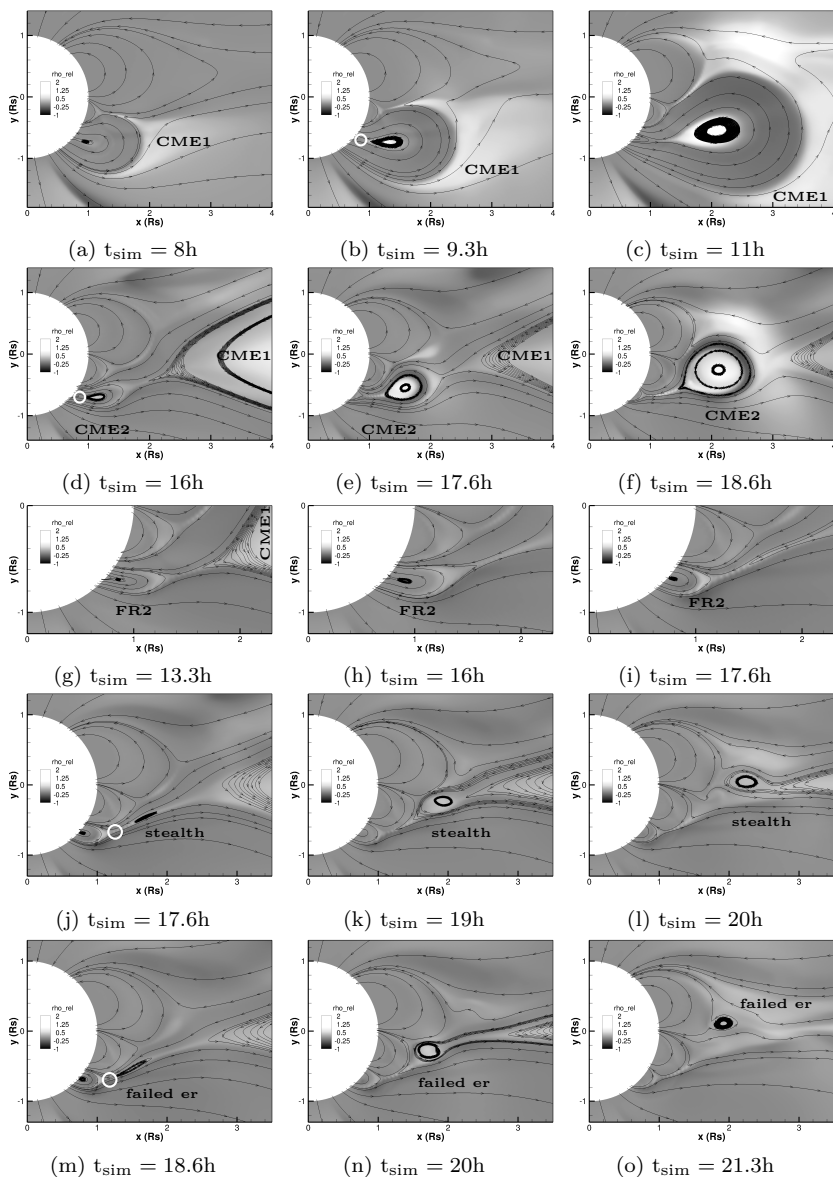


Figure 3.9: Simulated relative density (gray scale) and selected magnetic field lines during the formation phase of flux ropes (FRs), in the case of: first row - CME1; second row - CME2 (double eruption case); third row - second (FR2) which falls back to the Sun; fourth row - stealth eruption; fifth row - failed eruption. The white circles indicate reconnection sites. The relative density is $\rho_{\text{rel}} = \frac{\rho(t) - \rho_0}{\rho_0}$, where ρ_0 is the density of the initial relaxed state before the shear.

that the speed matches that measured at 1AU. Therefore we do not compare these small eruptions any further since they would require simulation from a data-driven MHD model. The time in the simulation videos is not normalized to a real unit system and the conversion equation is $t_{real} = t_{sim} \times 1.9325$ h, where t_{sim} is the time shown in movies. Also, the distances on axes are expressed in solar radii. The movie of the observations was visualized in the JHelioviewer software, using running difference images from the EUVI, COR1, and COR2 instruments on board STEREO-B.

The fastest shear we applied (37.4 km s^{-1}) results in the formation of another flux rope in the wake of the first CME, much in the same manner as the previous flux rope. The arcade expands again, and the sides pinch (white circle, Fig. 3.9d) and create the flux rope, which then erupts into the equatorial current sheet to produce CME2 (Fig. 3.9d,e,f). The evolution and propagation can be visualized in Fig. 3.10c,d. This second flux rope also forms in the next two scenarios, but it fails to erupt and falls back to the Sun, dissipating at the boundary (Fig. 3.9g,h,i).

The lowest speed we used (37 km s^{-1}) produced CME1 in the same way, but the magnetic flux introduced was insufficient to inflate the arcade long enough to make it detach once more. Instead, the unstable current sheet formed in the trail of CME1 reconnects (white circle, Fig. 3.9j) and creates a third flux rope after ≈ 17.5 h of shearing, which is then slowly deflected towards equator (Fig. 3.9j,k,l). Given the high altitude at which the reconnection sets in ($1.4 R_{\odot}$) and the low speed of the process, this second eruption most likely does not leave any clear signatures, placing it in the stealth CME category (Robbrecht et al. 2009b). Compared to CME2 from the previous case, this one is narrower, slower, and occurs later, as seen in Figures 3.10e,f.

Applying an intermediate shearing speed (37.2 km s^{-1}) again gives rise to CME1, to a second flux rope that falls back to the Sun, and to a third flux rope emerging through the same mechanism as the stealth, from coronal magnetic field reconnection (white circle, Fig. 3.9m) ≈ 19 h after the start of the shearing. Its evolution, however, is different since the small amount of additional flux translates into a slightly more energetic reconfiguration, which increases the speed of the flux rope. As a consequence of its higher acceleration, slightly higher speed, and lower formation height ($1.55 R_{\odot}$, taken at the center of the flux rope, as opposed to $1.7 R_{\odot}$ for the stealth), the CME cannot be deflected as easily towards the equator by the magnetic pressure gradient, and eventually reconnects with the large northern arcade, creating a failed (confined) eruption (Fig. 3.9m,n,o). We analyzed and compared the dynamics of the three scenarios in more detail, and these results are presented in the next section.

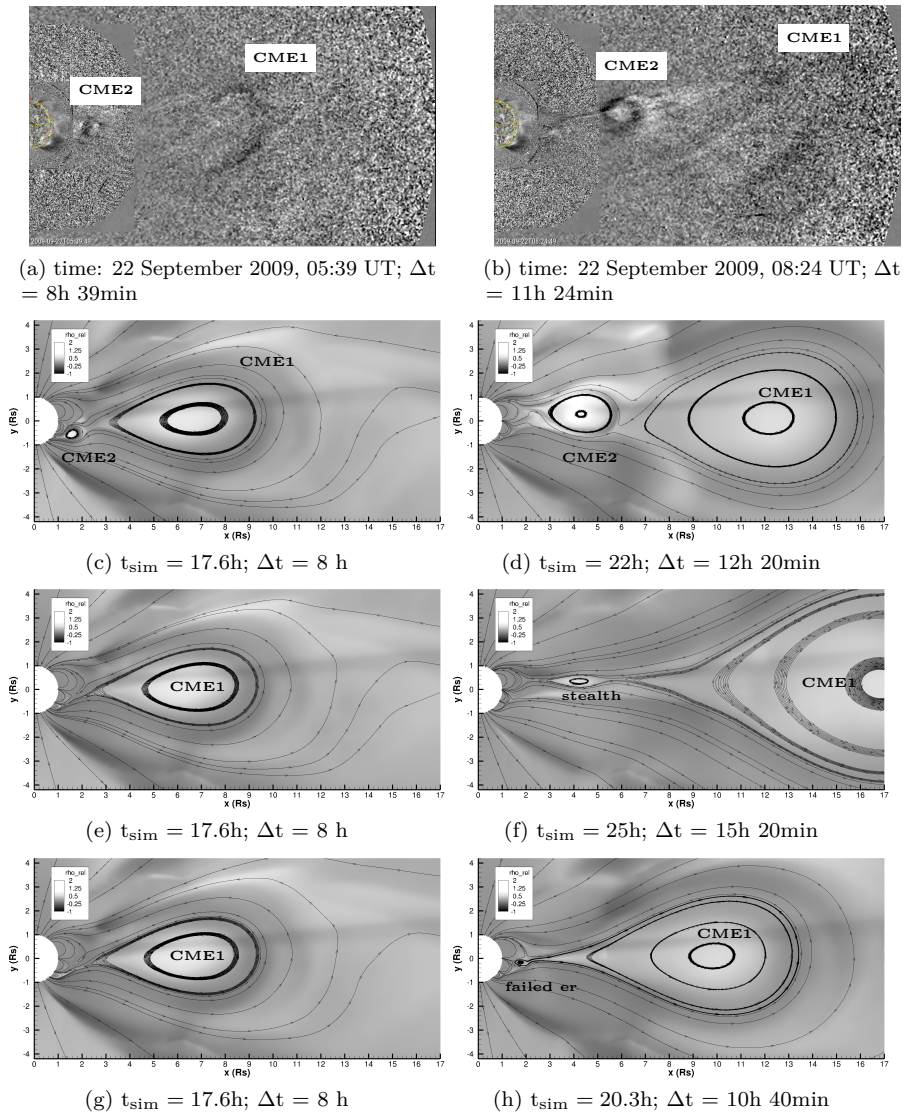


Figure 3.10: First column: Snapshots of observations and MPI-AMRVAC simulations taken when CME1 front is located at $10 R_{\odot}$. Second column: Snapshots of observations and simulations taken when CME2 front is located at $6 R_{\odot}$ (except (h)). Panels (a) and (b): Running difference images taken from EUVI, COR1, and COR2 instruments on board STEREO-B and visualized in JHelioviewer software. Snapshots of the simulated relative density and selected magnetic field lines: panels (c) and (d) indicate the double eruption scenario, (e) and (f) show the stealth eruption scenario, and (g) and (h) indicate the failed eruption scenario. The parameter Δt represents the time interval from the eruption of CME1, chosen as 21 September 2009 21:00 UT, or 9.6 h simulation time after the start of shearing motions, when the center of the flux rope crosses $1.5 R_{\odot}$ and enters COR1-B field of view.

3.5 Analysis of the simulations

In order to compare the dynamics of the simulated and observed CMES, we plotted the deprojected heights of the eruption fronts and the locations of simulated leading edges in Fig. 3.11. The real distances from Sun to the observed CMES were required in this step due to the 2.5D topology of the simulated eruptions, which would exclude any longitudinal deflection. The CMES on 21-22 September 2009 were tracked only in the COR2-B field of view, from which they began to propagate radially. Below $6 R_{\odot}$, the strong deflection and diffuse fronts of the CMES prevented us from extracting accurate information.

In the simulation data shown in Figure 3.11 there is only one representation of the first CME because it evolved similarly for all three cases, as described in Section 3.4. We note that the first simulated eruption was slightly faster than the observed eruption (but still extremely similar), with a simulated speed of 279 km s^{-1} corresponding to the last measured height in COR2-B, where the speed was 257 km s^{-1} . Given the fact that the background magnetic configuration and solar wind were not perfectly simulated to match remote sensing and in situ observations, this value is a good approximation. The second CME of the double eruption case correlates better with its observed counterpart, which has a simulated speed of 342 km s^{-1} at the last data point at a height of $18 R_{\odot}$, as compared to the observed 349 km s^{-1} . The stealth CME front was starting to merge with the trail of the first eruption at that distance, and therefore we were unable to detect it, but the speed of the center of the flux rope was 339 km s^{-1} . All three values closely resemble the observed values, therefore managing to realistically reproduce two slow CMES, with two different erupting scenarios.

Next, we focused more on the simulations as an independent result, rather than comparing them to the observations, and we analyzed the differences between the three cases. As shown in Figure 3.12, all three secondary eruptions present a stronger acceleration compared to CME1 when close to the Sun, owing to the depletion of background wind, and to the already open field lines created from the passage of the first CME. We note that CME2 from the double eruption case presents a slow initial rising phase. All three of these secondary eruptions emerge in the current sheet created by the first eruption, whereas CME1 needs to overcome the magnetic tension of the overlying field, hence the smaller acceleration and slow rise. The higher initial acceleration makes it harder for these narrower flux ropes to be deflected towards the equator, so they reach higher latitudes than CME1, as shown in Figure 3.13. In the case of the failed eruption, the slightly larger momentum of the flux rope increases the latitudinal deflection, making it unable to escape the reconnection with the

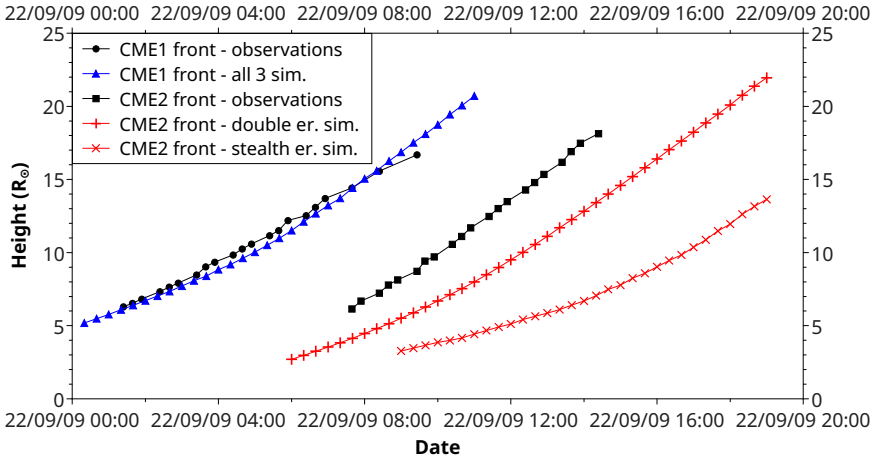


Figure 3.11: Location of the CMEs fronts in the meridional plane as a function of time. The black dots indicate the observed CME1, black squares indicate the observed CME2, blue triangles represent the simulated CME1, red crosses indicate the simulated CME2 (double eruption scenario), and red diagonal crosses represent the simulated stealthy CME2.

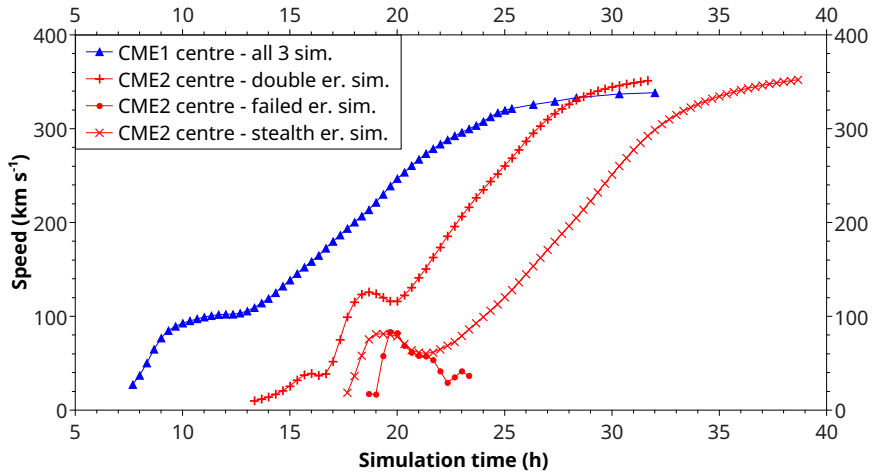


Figure 3.12: Total speed of the simulated CMEs, calculated at the center of the flux rope. The blue triangles indicate CME1, the red crosses indicate CME2 (double eruption scenario), the red dots represent CME2 (failed eruption), and the red diagonal crosses indicate stealthy CME2.

northern arcade. The timeline of its evolution can be seen in Fig. 3.9m,n,o, and is described as follows: 20.5 h after the initiation of the shearing motions, the flux rope enters the northern streamer; 20 min later, it gets trapped by the closed arcades, and after 23.5 h, it reconnects entirely and disappears. In the double eruption scenario, the second flux rope begins to form around 13.5 h after the start of the shearing motions, and is accelerated away from the Sun 3 h later. In the case of the stealth CME, the flux rope becomes embedded into the streamer after 19 h (Fig. 3.9k), a step which induces deceleration for all the scenarios, at their corresponding times.

Upon reaching the highest latitude, the polar magnetic pressure together with the northern streamer force all CMEs to deflect equatorward, thus also contributing to the deceleration of the CMEs. Once the propagation becomes radial and the CMEs enter the solar wind, they accelerate again and reach speeds of up to 350 km s^{-1} . Even though the CME formation and cause of eruption are different, it is interesting to point out the similarities in the overall speed profile of CME2 for the stealth and double eruption scenarios.

We also performed Poynting flux analysis by calculating the radial component of its associated vector close to the inner boundary through a sphere located at $1.14 R_{\odot}$ as follows:

$$S_r = \frac{[-(\mathbf{v} \times \mathbf{B}) \times \mathbf{B}]_r}{\mu_0} = \frac{B^2 v_r - (\mathbf{v} \cdot \mathbf{B}) B_r}{\mu_0}, \quad (3.7)$$

and multiplying every value with the corresponding area of the surface obtained by rotating the bottom of the grid cell around the Sun at $1.14 R_{\odot}$. The final values consist in the summation over the entire surface of the shell around the Sun, and their variation in time is shown in Figure 3.14, where time=0 indicates the start of the shear. As expected, the induced shearing motions increase the electromagnetic energy flow through the inner boundary, as seen in the first 6 h of simulation, during which the southern arcade starts expanding. Afterwards, the lateral magnetic pressure gradient compresses the field locally to create the first flux rope, and after ≈ 8 h this flux rope detaches from the Sun as it is accelerated a first time, which corresponds to the ‘shoulder’ in the radial Poynting flux, indicated by the arrow in Fig. 3.14. Following the eruption of CME1, a second flux rope begins to form as a consequence of ongoing shearing motions and lateral pinching commences after the peak at 12 h. This evolution is the same for all three simulation cases within the first 14 h. In the next part, the dynamics start to differentiate because this recently created flux rope erupts and forms CME2 in the double eruption case. For the other two scenarios, the remaining shear does not impose sufficient energy onto the flux rope to overcome the magnetic tension of the overlying closed magnetic field, so the

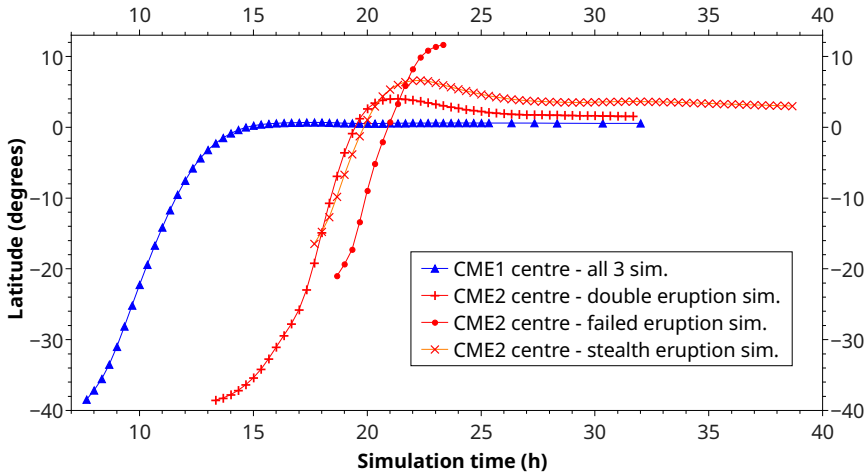


Figure 3.13: Latitude of the simulated CMEs with respect to the Sun’s equator as a function of time, taken at the center of the flux rope. The legend is the same as in Figure 3.12.

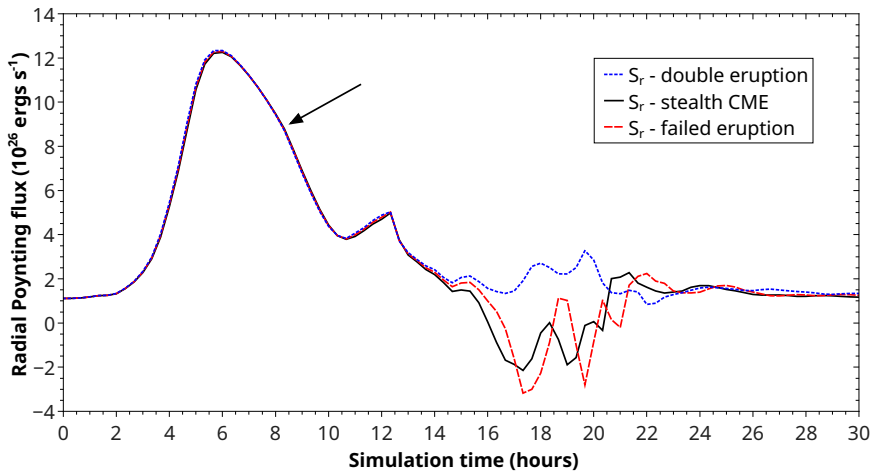


Figure 3.14: Evolution in time of the radial component of the Poynting flux, summed over the whole Sun.

flux rope falls back to the Sun at ≈ 15 h and disperses at the inner boundary, as described in Section 3.4.

A particularly interesting aspect presented in Figure 3.14 is that the Poynting

flux profile is practically the same until near the end of the shearing motions (which were applied for 16 h), yet the coronal environment behaves completely different from that point onwards. Furthermore, the radial electromagnetic energy flux is very similar in the cases of stealth and failed eruptions, emphasizing the argument stated before that these flux ropes are not caused by the shear, instead they result from the coronal magnetic field reconfiguration. This can also be seen in Figure 3.12, in the difference between initiation phases, which presents a slow rise for CME2 in the double eruption case, whereas for the other two, which form higher in the corona, the moment they are created also coincides with the initial acceleration stage.

3.6 Summary

Initially, this chapter was based on the observation of a multiple CME event on 21-22 September 2009, with an interval between the eruptions of approximately eight hours. In order to obtain the real propagation directions, we performed GCS analysis high in the corona on both CMEs, and derived an average longitude of 5.82°W for CME1 and of 6.7°W for CME2, respectively.

Subsequently, we used the MHD package of the code MPI-AMRVAC to numerically simulate consecutive CMEs by applying shearing motions at the inner boundary, starting from an initial triple arcade structure embedded into a bimodal solar wind. We changed the amplitude of the shear to understand the effects of its variation on the induced eruptions with the goal of obtaining a stealth eruption in the trailing current sheet of a preceding CME. We obtained three different eruption scenarios for the second CME, within just 1% variation of the lowest shearing speed (37 km s^{-1}). The three scenarios are: a stealth CME, a failed eruption, and a double eruption. We emphasize in particular the initiation, for the first time, of a stealth from the change in applied shear, and not only from the overlying magnetic field constraints, as previously studied. All three cases are comprised of a first eruption generated from the imposed stress at the inner boundary, and a second eruption occurring either from the reconfiguration of coronal magnetic field or from the additional v_ϕ component. We compared the height-time evolution of these eruptions with the observations described above, and achieved a good slope correlation for CME1 and CME2 from the double eruption scenario. The simulated deflection of both ejections in all cases was also studied by tracking the latitude and total speed of the flux rope centers. We would like to emphasize the physical interpretation of these results, in the sense that the solar corona can react and produce eruptions differently, given almost the same initial triggering factors, making the predictions of such eruptive processes even more difficult.

We also investigated the evolution of the radial Poynting flux close to the inner boundary, to acquire a global perspective of the electromagnetic energy introduced into the domain. The steps in dynamical evolution of the simulated CMEs could also be correlated with certain features, such as maximum, minimum or fluctuations, in the Poynting flux profile. This highlights the surprising similarities between the stealth and failed eruptions and the sensitive coronal response to stress factors. In Chapter 4 we discuss the propagation of these simulations in the interplanetary space and compare their signatures to in situ measurements.

Chapter 4

Study of the propagation, in situ signatures, and geoeffectiveness of shear-induced CMEs in different solar winds

Abstract

Our goal is to propagate multiple eruptions - obtained through numerical simulations performed in Chapter 3 - to 1 AU and to analyze the effects of different background solar winds on their dynamics and structure at Earth. We also aim to improve the understanding of why some consecutive eruptions do not result in the expected geoeffectiveness, and how a secondary coronal mass ejection (CME) can affect the configuration of the preceding one. Using the 2.5D magnetohydrodynamics (MHD) package of the code MPI-AMRVAC, we numerically modeled consecutive CMEs inserted in two different solar winds by imposing shearing motions onto the inner boundary, which in our case represents the low corona. In one of the simulations, the secondary CME was a stealth ejecta resulting from the reconfiguration of the coronal field. The initial magnetic configuration depicts a triple arcade structure shifted southward, and embedded into a bimodal solar wind. We triggered eruptions by imposing shearing

motions along the southernmost polarity inversion line, and the computational mesh tracks them via a refinement method that applies to current-carrying structures, and is continuously adapted throughout the simulations. We also compared the signatures of some of our eruptions with those of a multiple coronal mass ejection (MCME) event that occurred in September 2009 using data from spacecraft around Mercury and Earth. Furthermore, we computed and analyzed the Dst index for all the simulations performed. The observed event fits well at 1 AU with two of our simulations, one with a stealth CME and the other without. This highlights the importance of the processes the flux ropes undergo during their propagation in the interplanetary space. We simulate the CMEs propagated in two different solar winds, one slow and another faster one. In the first case, plasma blobs arise in the trail of eruptions. The faster solar wind simulations create no plasma blobs in the aftermath of the eruptions, and therefore we interpret them as possible indicators of the initial magnetic configuration, which changes along with the background wind. Interestingly, the Dst computation results in a reduced geoeffectiveness in the case of consecutive CMEs when the flux ropes arrive with a leading positive B_z . When the B_z component is reversed, the geoeffectiveness increases, meaning that the magnetic reconnections with the trailing blobs and eruptions strongly affect the impact of the arriving interplanetary CME.

This chapter is based on the previously published paper D.-C. Talpeanu, S. Poedts, E. D’Huys, M. Mierla (2022). "Study of the propagation, in situ signatures, and geoeffectiveness of shear-induced coronal mass ejections in different solar winds". In: *Astronomy&Astrophysics*, Volume 658, id.A56, 14 pp. The text was adapted in this thesis manuscript in order to avoid repetitions. D.-C. Talpeanu performed the numerical simulations and computations, the analysis of numerical and observational data, and prepared the manuscript.

4.1 Introduction

Stealth CMEs are events observed in coronagraph images but difficult to trace back to their origin. Even though their sources are difficult to locate, stealth CMEs can be unexpectedly geoeffective (Kilpua et al. 2014; Liu et al. 2016; Nitta et al. 2021). One reason is that the magnetic fields of slow and stealth CMEs may be enhanced by interactions with the background solar wind through

which they are propagating, resulting in surprisingly strong geomagnetic storms (He et al. 2018; Chen et al. 2019).

Palmerio et al. (2021) employed a multitude of imaging and geometric techniques, using various spacecraft images to identify the source of four stealth CMEs occurring throughout all the stages of the solar cycle. Several other authors such as Kilpua et al. (2014) and Nitta & Mulligan (2017) studied comprehensive sets of stealth CMEs, as well as their interplanetary counterparts, and even their effect on Earth's magnetosphere, which reached the level of intense geomagnetic storms.

The present study is a follow-up of Chapter 3, where we debate whether or not the second modeled eruption is indeed a stealth CME, because the simulations are more consistent with a scenario of an eruption driven by shearing motions from the inner boundary. In this Chapter, we model the propagation of those multiple eruptions to 1 AU in different background solar winds, compare in situ signatures, and compute the hypothetical induced geoeffectiveness. Numerical simulations are important in studying the propagation of multiple consecutive CMEs, because it is known that these can interact with each other and also with the background solar wind via magnetic reconnection and deflection (e.g. Manchester et al. 2017). Most of the time, the observational resources available to study these processes consist of remote-sensing images and in situ data at 1 AU. The limited information accessible between Sun and Earth means that numerical simulations are extremely useful in further understanding these interactions, as well as anticipating the morphology of interplanetary CMEs (ICMEs) arriving at Earth. Motivated by the above, we simulate the propagation of consecutive slow CMEs inserted in different solar winds in an attempt to further understand how such eruptions interact, and how the magnetic structure is distorted during the propagation. If these factors are reliably modeled, then it may be possible to compute the geomagnetic impact of the CMEs hours or even days ahead. We will assess this impact using the *Dst* index, which measures changes in the horizontal component of the magnetic field at ground level (Sugiura & Kamei 1991). Several authors have developed ways of *Dst* prediction using solar wind parameters, which take into consideration different effects and mechanisms, from the first and simplest model of Burton et al. (1975) to some of the most complex semi-empirical algorithms of Temerin & Li (2002, 2006). In the final step of our analysis, we use a modified version of the method outlined by O'Brien & McPherron (2000) to compute the geoeffectiveness of our simulated CMEs. We chose this method because of its relative simplicity and fast computational speed.

4.2 Observations

The observed event modeled here consists of an MCME that was seen on 21-22 Sept 2009. The second eruption of this event was considered to be a stealth due to the lack of clear low coronal signatures. The reader can find detailed EUV and coronagraph observations and kinematics information of this event in Chapter 3.

In that Chapter, the deprojected velocities of the CMES have been calculated along with the propagation longitudes, and the results were $257 \pm 69 \text{ km s}^{-1}$ and 5.82° W for CME1, and $349 \pm 70 \text{ km s}^{-1}$ and 6.7° W for CME2. The second eruption was faster than the first one because of the depletion of solar wind material caused by the passage of its precursor. As both ejections were Earth-directed and there were no major CMES before or after them, one can assume that in the absence of strong erosion forces during their propagation, the flux ropes could have arrived at our planet. Their low speeds also led to the expectation that the CMES would arrive at Earth with almost the same speed as the solar wind into which they were inserted because of the drag forces exerted onto them. This speed was calculated in Chapter 3, and was assumed to remain constant throughout the propagation, resulting in an average of $\approx 330 \text{ km s}^{-1}$ (Fig. 3.6) and providing an arrival date at 1 AU between 27 and 28 Sept 2009. In the present follow-up Chapter, we investigate possible ICME signatures at Mercury and Earth, and find a clear jump in total magnetic field, as well as a smooth rotation of the B_z component in MESSENGER data. As it was such a weak event, the signatures at 1 AU were not as clear, but still distinguishable from the background noise, and they are presented and compared with our simulations in Section 4.5.

4.3 Numerical MHD code and methods

In this follow-up study, our goal is to propagate the CMES simulated in Chapter 3 out to 1 AU, and therefore the numerical setup and code are very similar. In addition, we investigate the effect of an increase in speed of the background solar wind on the dynamics and resulting geoeffectiveness of the eruptions, which we discuss further below. We performed numerical MHD simulations using the code MPI-AMRVAC with a 2.5D spherical axisymmetric solution. The computational domain spans from the low corona until 1.5AU, and from the north solar pole to the south solar pole, that is $(r, \theta) \in [1, 322] R_\odot \times [0^\circ, 180^\circ]$, where r is the radial distance from the center of the Sun and θ is the heliographic colatitude. We extend the outer boundary by 0.5AU as compared to the previous study because here we analyze the in situ signatures at Earth

and we want to avoid possible artificial boundary effects. This change does not influence the initiation phase of the CMEs or the early propagation phase discussed in Chapter 3. The 2D grid has an initial resolution of 516×240 cells in the r and θ directions, and the number of cells is increased by up to twofold through the same AMR routine as in Chapter 3 (see Section 3.3). The logarithmic stretching of the grid keeps the scale of the cells constant, and the ratio between the widths or heights of the furthest cell to those of the closest cell in the same grid level of refinement is ≈ 321 .

The spatial and temporal discretization of the MHD equations is performed in the same way as in Chapter 3. In order to maintain a divergence-free magnetic field solution, the same GLM method is applied.

The initial conditions into which we are erupting CMEs consist of a bimodal background solar wind symmetric in the ϕ direction and obtained by introducing extra source terms to the momentum and energy equation that account for gravity and heating mechanisms. The bimodality is expressed as a function of latitude, with faster solar wind at high latitudes, consistent with the data obtained by the Solar Wind Observations Over the Poles of the Sun (SWOOPS, Bame et al. 1992) instrument on board Ulysses spacecraft (McComas et al. 1998), as well as with interplanetary scintillation (IPS, Hewish et al. 1964) observations at solar minimum. This type of solar wind model was used by Jacobs et al. (2005), Chané et al. (2006), Chané et al. (2008), and Hosteaux et al. (2019), and in Chapter 3. The volumetric heating function that defines the separation between slow and fast wind is the same as that from Chapter 3 (Equation 3.2 and the subsequent definition of $\sin^2(\theta_0)$), which also includes T_0 (K). The parameter T_0 (K) represents the target temperature through which we can adjust the momentum of the background wind, and therefore its speed as well. We used the same temperature as in Chapter 3 in order to propagate the same solar eruptions, but also a higher value in order to obtain a separate faster solar wind. The aim here is to investigate whether the plasma blobs occurring in the aftermath of eruptions are influenced by the speed of the background wind, but also whether or not the initial magnetic configuration, eruption dynamics, propagation, and geoeffectiveness of CMEs are affected in any way. Therefore, we refer from now on to our two configurations and separate simulations as slow wind (SW) and faster wind (FW), and not as composite latitudinal parts of the same solar wind. The two individual types of winds (separate simulations) are determined by T_0 in the following way: from θ_0 towards the equator, $T_0 = 1.32 \times 10^6$ K for the slow wind and $T_0 = 1.5 \times 10^6$ K for the faster wind, and from θ_0 towards the pole, $T_0 = 2.31 \times 10^6$ K for the slow wind, and $T_0 = 2.625 \times 10^6$ K for the faster wind. This results in the following minimum and maximum speeds at 1 AU: 330.6 km s^{-1} and 735 km s^{-1} for the slow wind, and 375.7 km s^{-1} and 786.3 km s^{-1} for the faster wind.

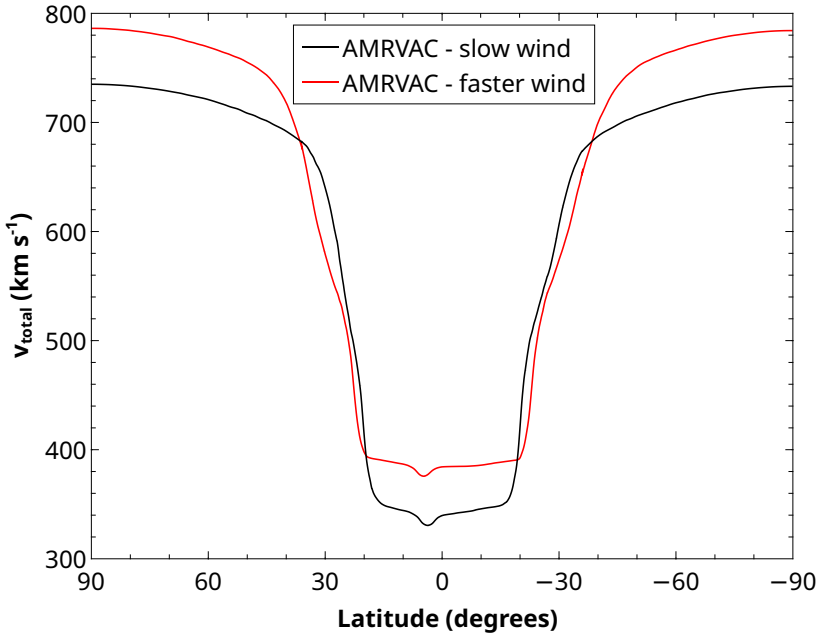


Figure 4.1: Total speed of the simulated slow (black line) and faster (red line) background solar winds, calculated at 1 AU.

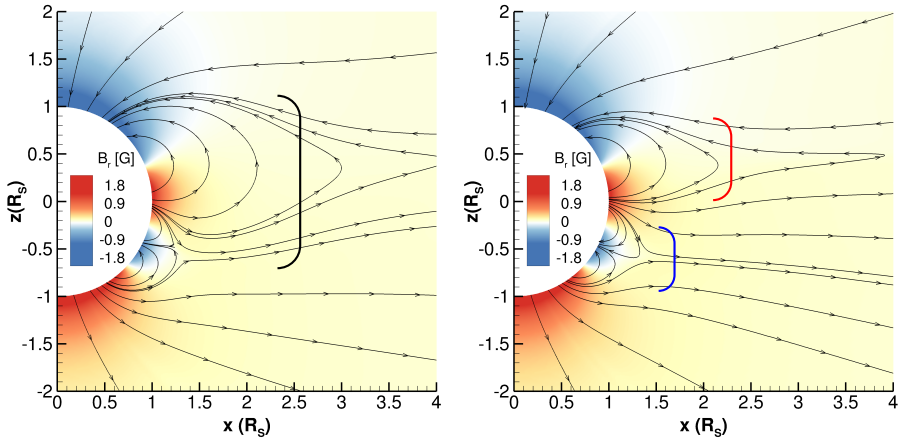


Figure 4.2: Initial magnetic field configuration - B_r (color scale) and selected magnetic field lines in the meridional plane for the slow solar wind (left side) and faster solar wind (right side).

The minimum value of the speed is found in the equatorial current sheet, which is shifted northward because of the initial asymmetric magnetic configuration described later on. The maximum value is found at the north pole (90° latitude), and the speed profile of both background winds at 1 AU can be seen in Fig. 4.1.

The mass density and temperature are fixed at the inner boundary to $1.66 \times 10^{-16} \text{ g cm}^{-3}$ for both winds, and to $1.32 \times 10^6 \text{ K}$ for the slow wind, and to $1.5 \times 10^6 \text{ K}$ for the faster wind. The other variables at the inner and outer boundaries (located at 1.5 AU) are defined in the same way as in Chapter 3, Section 3.3. Also, the magnetic field configuration is created via the same set of equations as in Section 3.3, which described a triple arcade system added to a background dipole field. Even though the same conditions are applied on both solar winds and the resulting values are extremely similar, the created magnetic configurations are not identical, as can be seen in Fig. 4.2. The similarity between the values can be seen clearly in the top left panel of Fig. 4.3. This interesting result is discussed further below.

In order to propagate two of the eruptions obtained in Chapter 3, we created CMEs in the same manner (see Section 3.3), by applying the same shearing motions and amplitudes onto the inner boundary in the azimuthal direction, summed with the differential rotation previously mentioned, only after the solar winds have reached a steady-state solution.

4.4 Simulated eruptions and solar winds

The slow solar wind case in the current study is almost identical to the background wind in Chapter 3, with the two differences that the outer boundary of the computational domain is extended until 1.5 AU, and that the refined grid area close to the Sun is enlarged such that it encompasses the entire arcade system. However, these changes had no effect on reproducing two of the eruptions in Chapter 3. Therefore, we could consider them identical and propagate them to Earth.

We obtain an initial interesting result simply from comparing the two background solar wind simulations (Fig. 4.2). As mentioned above, the same magnetic boundary conditions in combination with a hotter, denser, and faster wind resulted in a very different magnetic configuration, as shown in Fig. 4.2. The initial helmet streamer (indicated by the black bracket on the left side of Fig. 4.2) breaks up into a northern smaller arcade (red bracket, right-hand side of Fig. 4.2) and a southern pseudostreamer (blue bracket, right-hand side of Fig. 4.2), as a result of the applied change in temperature and ultimately in speed, as seen in the bottom right panel of Fig. 4.3. The values shown in

Fig. 4.3 are extracted from the first cell of the computational domain, and B_{total} and v_{total} are calculated by taking the square root of the sum of the squares of all their respective components. The numerous latitudinal variations in total speed occur because of the plasma changes at the boundaries of each magnetic arcade, and at the two (northern and southern) interfaces between slow and fast wind contained in the same magnetic configuration/simulation. Surprisingly enough, the radial component of the magnetic field is not affected by the modified temperature, as indicated by the overlapping curves in the top left panel of Fig. 4.3, and yet a different configuration is created. As a result, the only influence on the total magnetic field, and therefore on the overall arcade configuration, is provided by the B_θ component (because B_ϕ has a value of 0 at the inner boundary), which changes along with other plasma parameters. At higher distances, all the magnetic field components change due to the higher speed and density of the faster solar wind configuration, which determine a different coronal and heliospheric structure.

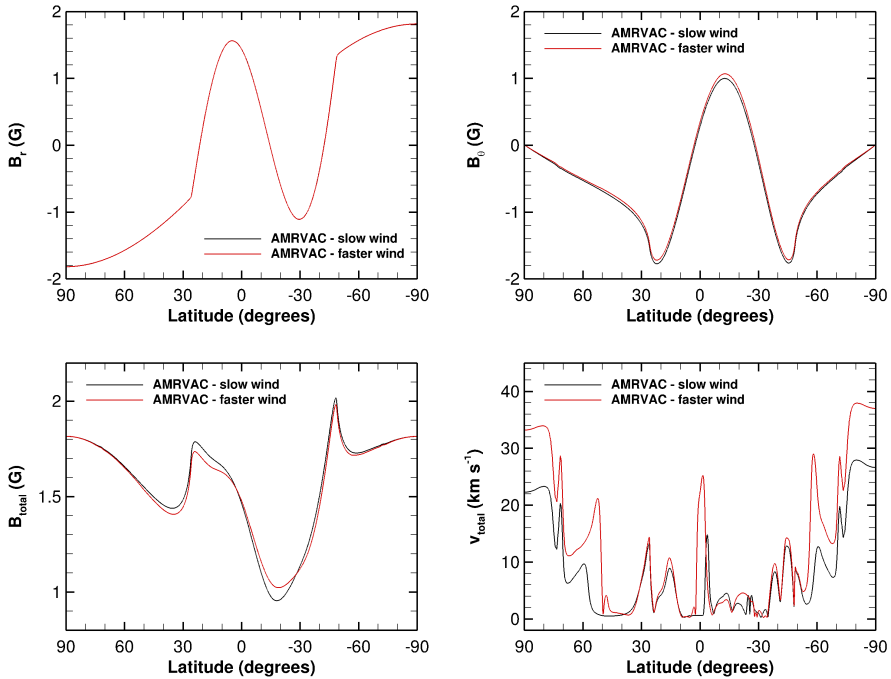


Figure 4.3: Magnetic field components and total speed calculated in the first cell of the computational domain, for both solar winds: top left - B_r , top right - B_θ , bottom left - B_{total} , bottom right - v_{total} .

Once both solar winds relaxed to a steady state and no more changes occurred in the magnetic field at the outer boundary, we created CMEs by applying an additional v_ϕ component to the inner boundary, approximately along the southernmost polarity inversion line as described in the previous section. The shearing motions applied to the arcade in the slow wind case are the same as those that resulted in double and stealth eruptions in Chapter 3, where they are also described in more detail. Briefly, in Chapter 3 we numerically simulated three different types of consecutive solar eruptions by varying the shearing motions applied at the inner boundary by only 1%. The two cases of interest for the current study are comprised of a first CME triggered in all the cases by the shearing motions, and a second eruption which was generated either by the shear (double eruption case) or by the reconfiguration of the coronal magnetic field (stealth eruption case). Inside the current sheet that followed the eruptions, plasma blobs were created via magnetic reconnection in all the scenarios. In order to analyze the effects of the trailing eruptions on the first CME, we also performed a simulation with a single flux rope formation by decreasing the amplitude of v_0 and implicitly that of v_ϕ .

We also simulated a faster solar wind by increasing the temperature of the initial background wind. We performed this change with the aim of investigating the occurrence of plasma blobs in the trailing current sheet of CMEs in a different plasma environment. In order to recreate the eruptions that led to the presence of blobs in their aftermath, we applied the amplitudes of v_0 that resulted in stealth ejecta and single eruptions in the slow wind case to the inner boundary of the newly simulated faster wind. Below, we refer to these current simulations (same v_0 but different background wind) as the stealth speed case (unrelated to the stealth ejecta formation mechanism) and the single eruption case, respectively. Even though the same amplitudes of v_0 applied in the ghost cells did not produce the exact same values of v_ϕ inside the computational domain, we kept the same numbers of v_0 for consistency, and the actual values measured in the first cell of the domain can be seen in Table 4.1, taken at half (at 8h) the length of shearing time (16 h).

Table 4.1: Maximum shearing speeds in absolute value for both solar winds in all simulation cases, taken from the first cell of the computational domain.

Background wind	Eruption type	$ v_\phi^{max} $ [km s ⁻¹]
Slow wind	double er.	37.43
	stealth er.	37
	single er.	21.95
Faster wind	stealth speed	36.77
	single er.	22.33

In total, we performed five simulations and for each of them, Figures 4.4, 4.5, 4.6, 4.7, and 4.8 show three snapshots in time of the propagation of the erupting structures through the solar wind. These figures are accompanied by supplementary videos available online ⁹. For easier visual inspection, in all five figures the gray scale indicates the density of the current time-step snapshot relative to the relaxed wind state, similar to base difference images created from coronagraph images (lighter shading indicates denser plasma). The relative density is defined as $\rho_{rel} = \frac{\rho(t) - \rho_0}{\rho_0}$, where ρ_0 is the density of the initial relaxed state before the shear. The slow wind is abbreviated as ‘SW’ and the faster wind as ‘FW’. The time t_{sim} is counted from the start of shear. In all cases, the first flux rope is formed by the applied azimuthal flow through the same physical processes. The additional v_ϕ firstly increases the magnetic pressure inside the southernmost arcade, expanding it and making it rise. As a consequence, an imbalance is created between the magnetic tension and magnetic pressure gradient which leads to a local compression of the magnetic field. The numerical resistivity allows the sides of the arcade to reconnect, thus creating the flux rope, which begins to erupt. The southern polar magnetic pressure deflects it towards the equator, until it starts propagating radially inside the equatorial current sheet from several solar radii onwards, depending on each scenario. The secondary eruptions (if any) differ for each case, and the five numerical simulations can be briefly described as follows (including the first CME):

1. Single eruption (slow wind): Given the low amplitude of the shearing motions, only one flux rope is formed 12 h after the start of the shear, which slowly erupts and gets deflected towards the equatorial plane, creating the main CME (Fig. 4.4a,b). The current sheet formed in the wake of this eruption magnetically reconnects and thus five plasma blobs arise, of which only one survives during their journey to Earth and is indicated by the white arrow in Fig. 4.4c. An extra blob forms much later during this propagation (84 h after the start of the shear) and is indicated by the black arrow in Fig. 4.4c. The rest of the blobs magnetically reconnect with the first CME, because they are created in a depleted solar wind environment which allows them to easily catch up with their precursor.
2. Eruption + stealth (slow wind): After the formation of the first flux rope (8 h after the shear start) triggered by shearing motions, and the ejection of the associated CME (Fig. 4.5a), a second flux rope (stealth ejecta) is created from the reconfiguration of the coronal magnetic field and erupts in the trail of the preceding eruption (Fig. 4.5b, indicated by the white arrow), also being deflected towards the equator. Two plasma blobs arise in this case as well (apart from the stealth ejecta) and maintain their

⁹<https://www.aanda.org/articles/aa/olm/2022/02/aa41977-21/aa41977-21.html>

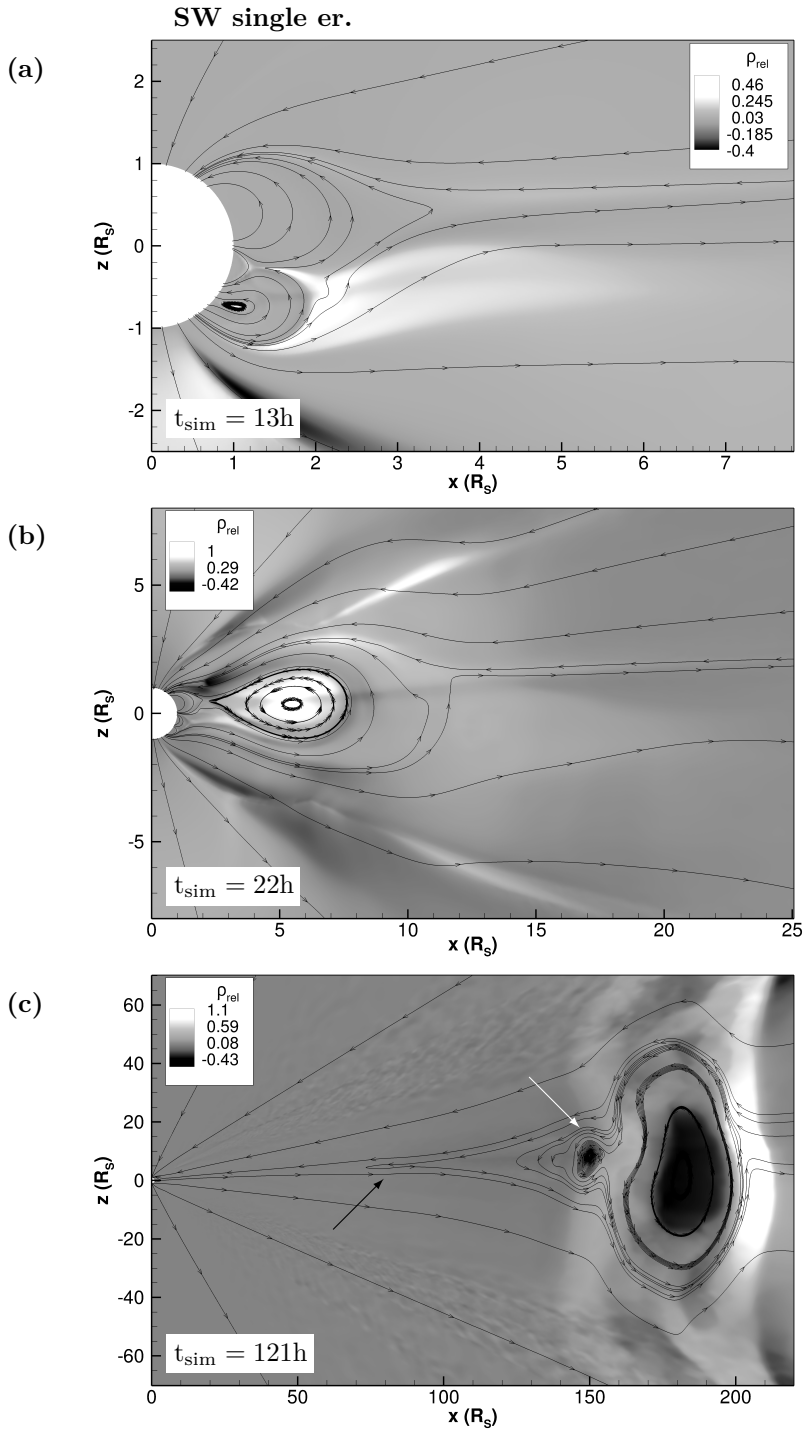


Figure 4.4: Snapshots of the simulated relative density (gray scale) and selected magnetic field lines during the evolution of the single eruption case ejected into the slow wind.

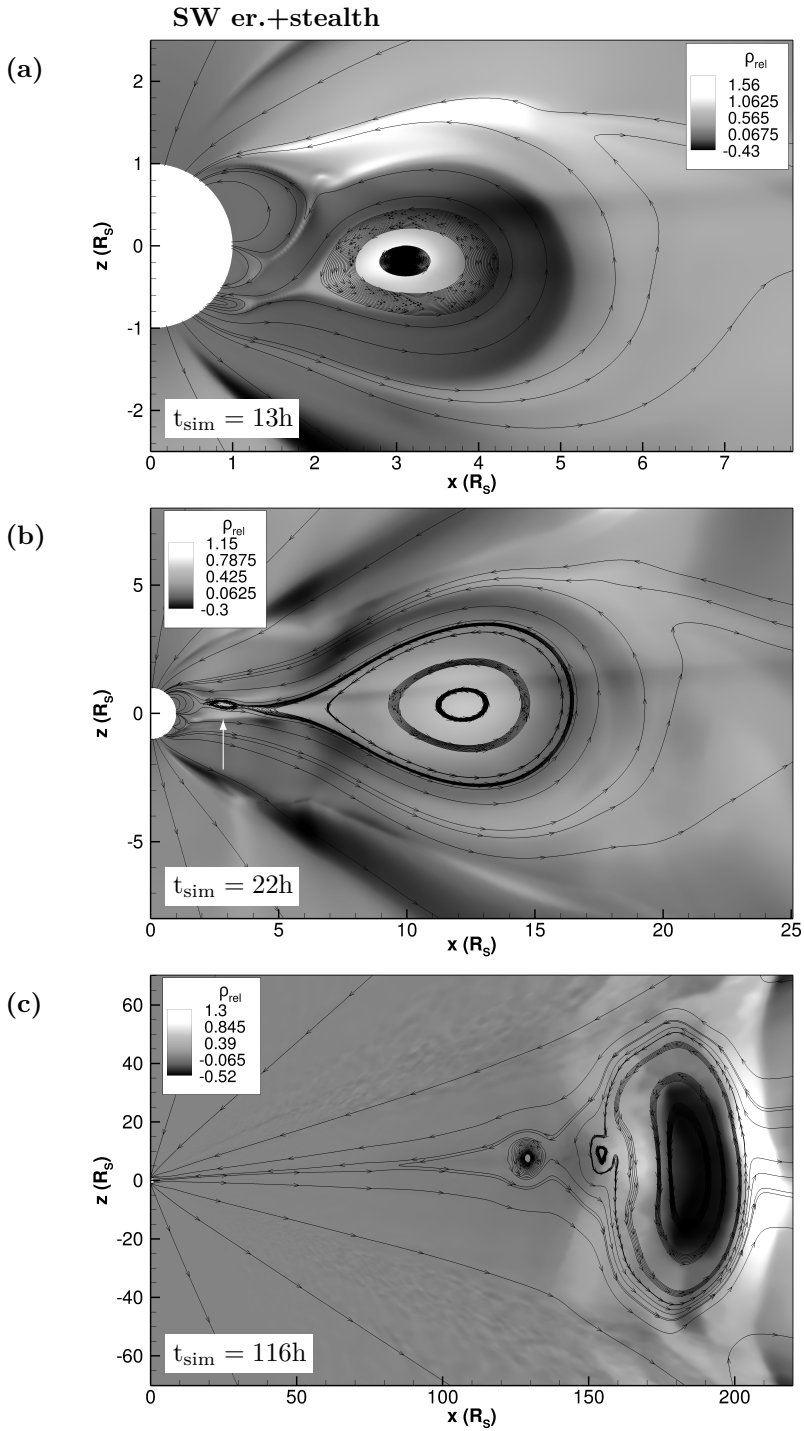


Figure 4.5: Same as Fig. 4.4, but in the eruption+stealth case, ejected into the slow wind.

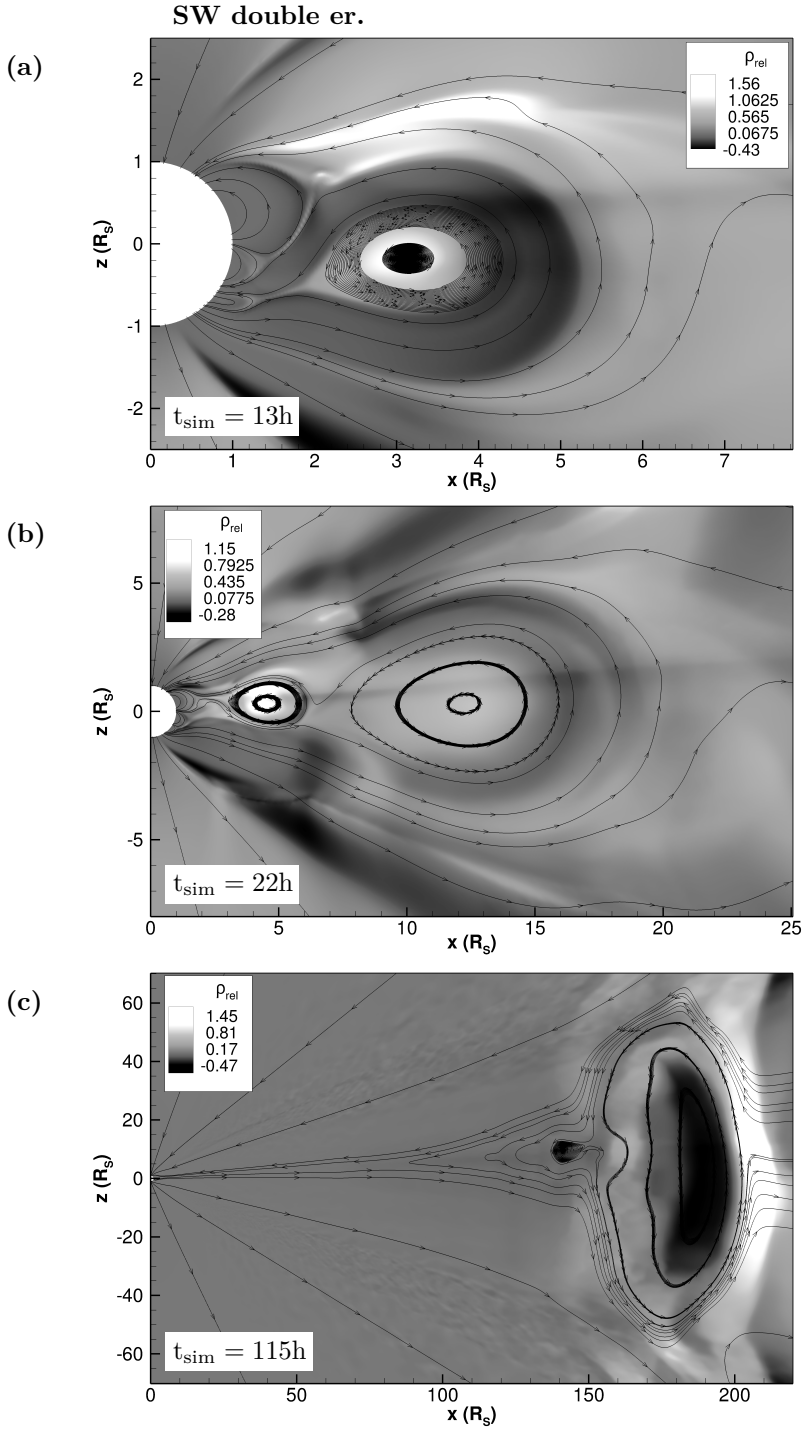


Figure 4.6: Same as Fig. 4.4, but in the double eruption case, ejected into the slow wind.

FW single er.

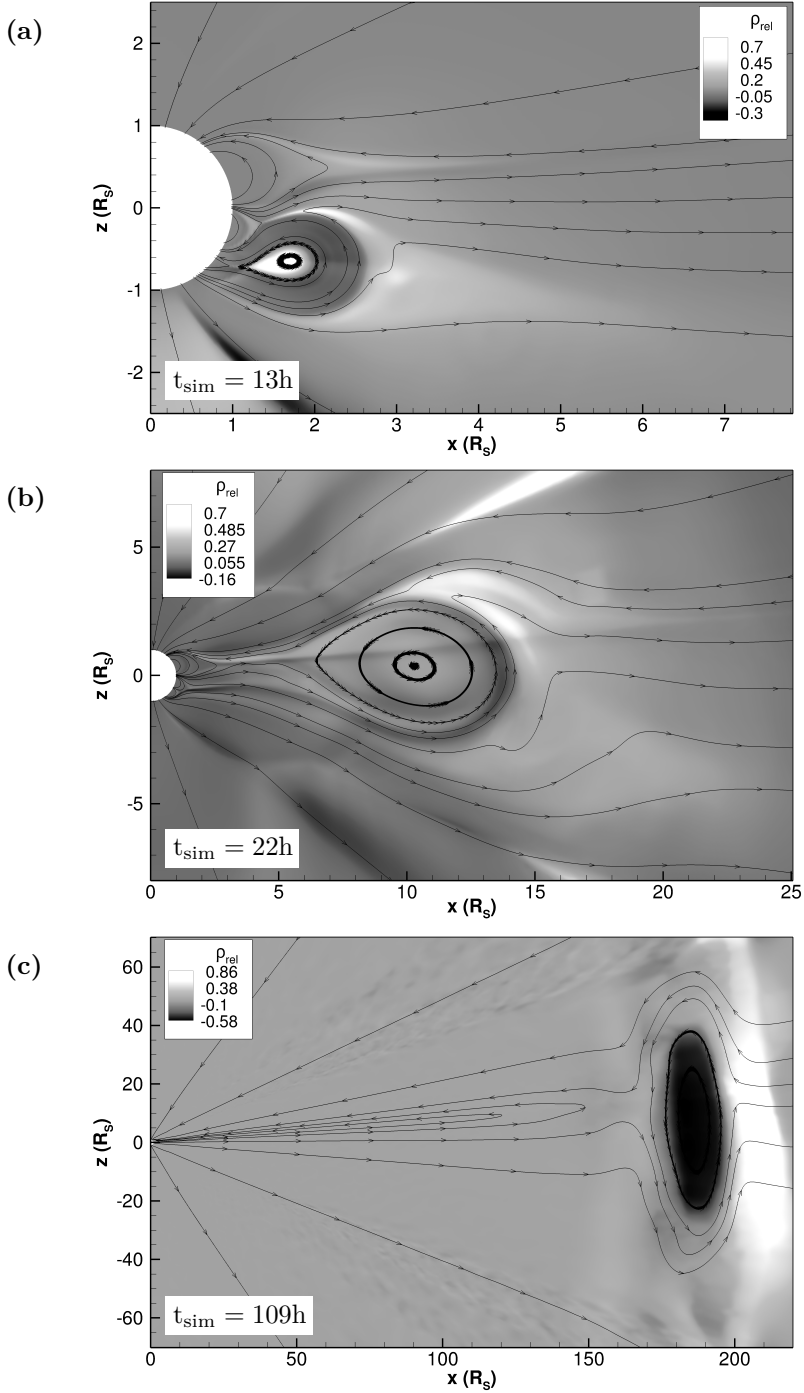


Figure 4.7: Same as Fig. 4.4, but in the single eruption case, ejected into the faster wind.

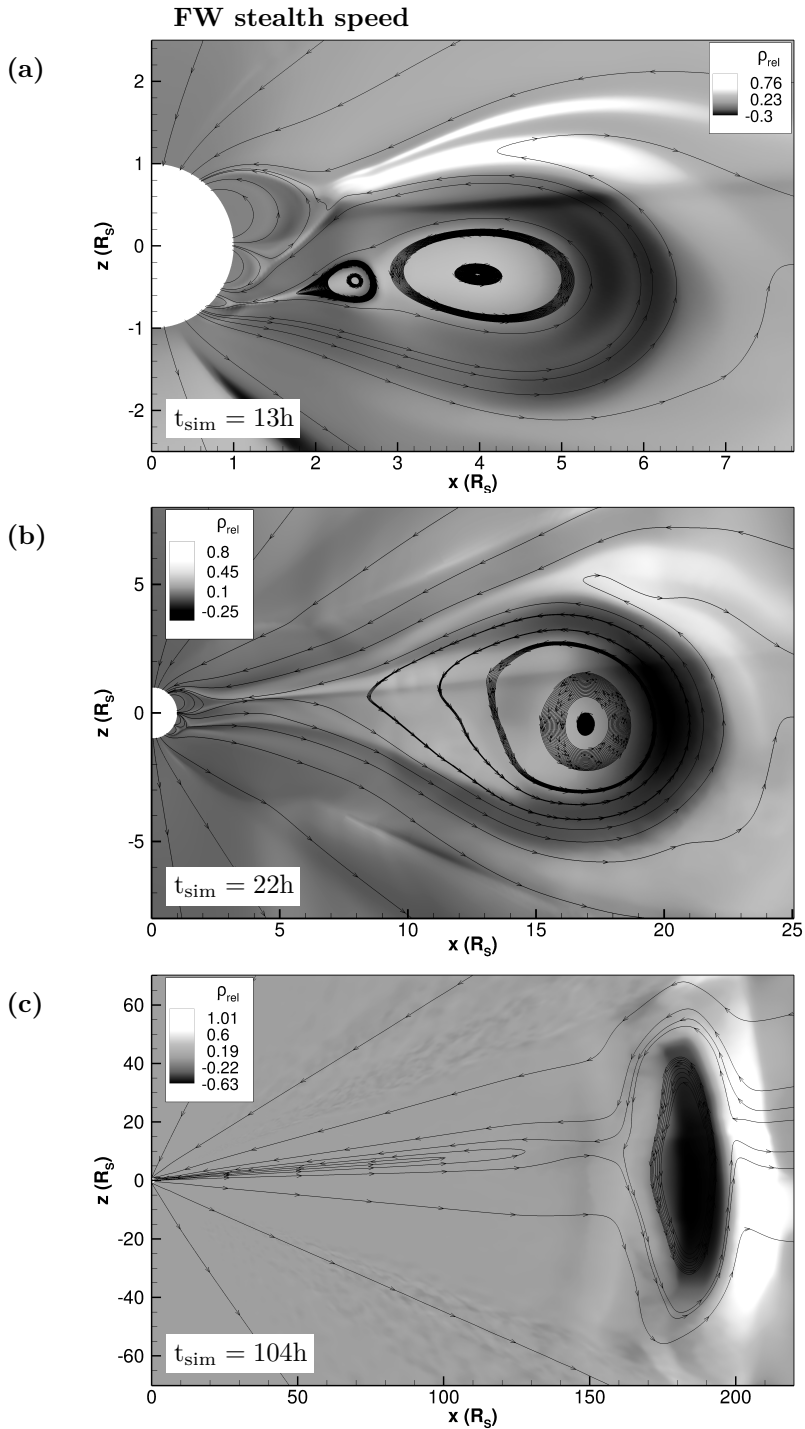


Figure 4.8: Same as Fig. 4.4, but in the stealth speed case, ejected into the faster wind. This case resulted from applying on the faster wind the same shearing speed that created a stealth ejecta in the slow wind case (Fig. 4.5).

magnetic structure until 1 AU. Similarly to the previous case, an extra blob is created 82 h after the start of the shear, and so when the CME arrives at Earth, there are three trailing flux ropes, as the stealth ejecta magnetically reconnected with the first eruption.

3. Double eruption (slow wind): After the first CME (Fig. 4.6a), a second flux rope also erupts (Fig. 4.6b), both triggered by the shear applied at the boundary. During their propagation to 1 AU, the slow nature of both eruptions allows the second CME to reconnect with the first one, arriving as one entity at Earth, as seen in Fig. 4.6c. From the five plasma blobs created, only two remain after 115 h, but the second one disappears shortly after that. Following the other two cases, another blob arises in the trailing current sheet 87 h after the start of the shear.
4. Single eruption (faster wind): An erupting flux rope is formed 10 h after the start of the shear, and is deflected northward into the equatorial current sheet, into which it propagates almost radially after ≈ 20 h (Fig. 4.7a,b). Interestingly enough, there are no plasma blobs created after the CME, which arrives at Earth after ≈ 109 h as one pancaked flux rope, followed by the trailing streamer current sheet forming again in its wake (Fig. 4.7c).
5. Stealth speed (faster wind): A first flux rope is formed much faster than in the single eruption case (similarly to the slow wind scenarios), namely 7 h after the start of shear, and a second one only 12 h after the start of shearing, both being deflected northward into the equatorial current sheet (Fig. 4.8a). The second flux rope is no longer created from the reconnection of the coronal magnetic field, but is a result of the imposed shearing motions. Their faster formation and eruption speeds led to a much earlier merging between the two CMEs, propagating as one entity as of 19 h from the start of shear (Fig. 4.8b). Their quick reconnection created a very similar pancaked flux rope to that of the single eruption case at 1 AU (Fig. 4.8c), but not the same magnitude of magnetic field, as will be shown in the following two sections (4.5 and 4.6). Interestingly, in this case there were also no plasma blobs created, making their formation dependent on the initial magnetic configuration rather than the magnitude of the shearing speed.

The first two panels ((a) and (b)) of Figures 4.4, 4.5, 4.6, 4.7, and 4.8 are snapshots of simulations taken at the same time in order to show a comparison between the formation and eruption of the CMEs created in the two different background winds. We note the difference in density, for instance in the single eruption cases. The flux rope in the slow wind is filled with plasma, whereas in the faster wind, the front is more compressed due to the higher speed, and

therefore is denser than the core. However, this ratio is not kept during the propagation to 1 AU, probably due to the drag forces exerted by the background wind and by the different initial densities as a result of higher temperatures. The arrival at 1 AU of the CMEs can be seen in panel (c) of each of the above-mentioned figures, which occurs at a different time for each simulation.

4.5 Comparison with in situ signatures

Simulations should show some agreement with observations if they are to help us understand the physics of actual events. Once the simulation is realistic, it is interesting to investigate how different variables influence the eruption itself and the propagation through the interplanetary space, because one particular event is not representative of the multitude of eruptions and solar parameters. Fortuitously, the MCME described in Section 4.2 erupted on 21-22 Sept 2009, and encountered spacecraft at Mercury and Earth, allowing us to compare our simulation results with in situ observations at these locations.

The comparison close to the Sun between these two simulations and the event was performed in Chapter 3, and in this Chapter we are focusing on the interplanetary part and in situ signatures. We took 1D slices in our 2.5D simulations on the equatorial plane and extracted the data at $75 R_{\odot}$ and $215 R_{\odot}$ in order to compare with measured values at Mercury and at Earth. As this eruption takes place at the time of the equinox, the equatorial and ecliptic plane coincide, and no latitudinal correction is needed. On 23 Sept 2009 (when the CME arrived at Mercury), the MESSENGER spacecraft was at an angle of only $\approx 11^{\circ}$ westward from the Sun–Earth line at a distance of $\approx 75 R_{\odot}$ from the Sun and not in Mercury’s magnetosphere. This makes the onboard Magnetometer (Anderson et al. 2007) instrument ideal for in situ magnetic field data comparison with our simulations. The in situ values at Earth (L1) were taken from the OMNI database, which combines data measured by the WIND (Ogilvie et al. 1995; Lepping et al. 1995) and ACE (Stone et al. 1998) spacecraft to provide near-continuous solar wind observations. The cadence of the data used was 1 min for MESSENGER and 5 min for OMNI, both averaged over 20 minute intervals in order to reduce fluctuations that are on much smaller scales than those produced in the simulation, but also to ease inspection of the structures of interest. For a proper comparison with the in situ data, we also averaged our simulation values over 20 minutes, because even though they lack the small-scale structures, the amplitude of the investigated flux ropes are also affected by the averaging, and we wish to be consistent in our study. We mention that the simulation time has been matched with the observed time at the moment when the dark cavity of the first CME was still just within the

COR1-B field of view, at 23:00 on 21 Sept 2009. From then on, we no longer adjust the simulation time. This process was required because the simulation time starts counting at the start of shear when $t_{\text{sim}} = 0$ h, and it needs to be given a real date, otherwise the data cannot be compared.

In Fig. 4.9, the ICME can be distinguished in MESSENGER data by the increase in total magnetic field and B_y , as well as the fairly smooth rotation in the B_z component, criteria based on which the green area has been delimited. The simulation data show similar trends for both cases, eruption + stealth and double eruption, as well as a perfect arrival time (at Mercury). The second flux rope can still be differentiated from the first one in the observed data, by the presence of the dip delimited by the gray dashed line in the total magnetic field and in the B_y component on 24 Sept at $\approx 08:00$. The simulations also show a second flux rope, which is much more pronounced in the double eruption case (separation indicated by the cyan dashed line). This happens because the second CME in this scenario is wider and has a stronger magnetic field than the stealth CME. However, the main difference between MESSENGER and AMRVAC data is that the observed signatures of total magnetic field and the B_y component last almost twice as long.

During the propagation until 1 AU, the influence of the real solar wind exhibits a larger impact than closer to the Sun and its drag force is dominant as compared to other forces, which distorts the signatures. This effect can be seen in the magnetic field components measured near Earth and is shown by the black lines in Fig. 4.10 in the top three panels. The arrival time at Earth in simulations is also affected by the faster background solar wind speed at the equator (340 km s^{-1}), as compared to the very localized minimum speed recorded in the northward-shifted current sheet (330.6 km s^{-1} , Fig. 4.1). We noticed in AMRVAC data the well-known and thoroughly studied pancaking effect of the frontal flux rope, but also the merging of both secondary flux ropes with the first one, as they are ejected into a depleted solar wind from the passage of the first CME. Even though the first two flux ropes are reconnected, the signature of the previously present second CME is stronger in the double eruption case than in the stealth ejecta, as you can see in the evolution of the B_z component (blue and red lines, second panel in Fig. 4.10). After B_z turns negative, it increases again but no longer changes sign, which also affects the minimum value of this component. As the CME arrives at Earth with a positive frontal B_z , the negative trailing magnetic field is diminished due to the reconnection with the following flux ropes, leading to an increased (closer to zero) value of the negative part. Some plasma blobs can still be distinguished by the small oscillations in the trail of the ICMEs.

The compressed front of the first CME evident in observations is reproduced well in simulations, as seen in the first peak of the dynamic pressure (P_{dyn} panel

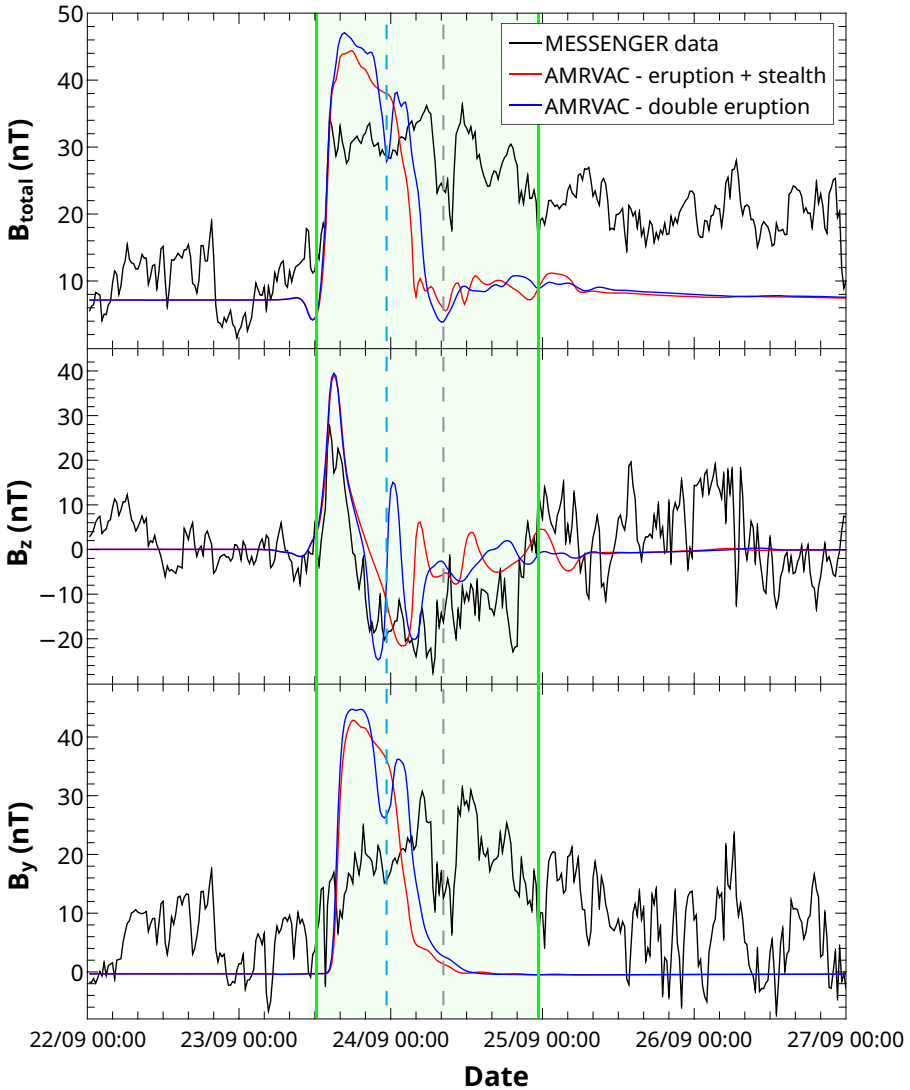


Figure 4.9: In situ measured components of the magnetic field taken by MESSENGER (black line), and simulation data in the eruption + stealth (red line) and double eruption (blue line) cases, propagated in the slow wind and taken at $75 R_{\odot}$. The green highlighted area approximately delimits the observed ICME. The cyan and gray dashed lines indicate the separation between the two flux ropes in the simulated double eruption case, and observed data, respectively. The dates on the X axis are from the year 2009.

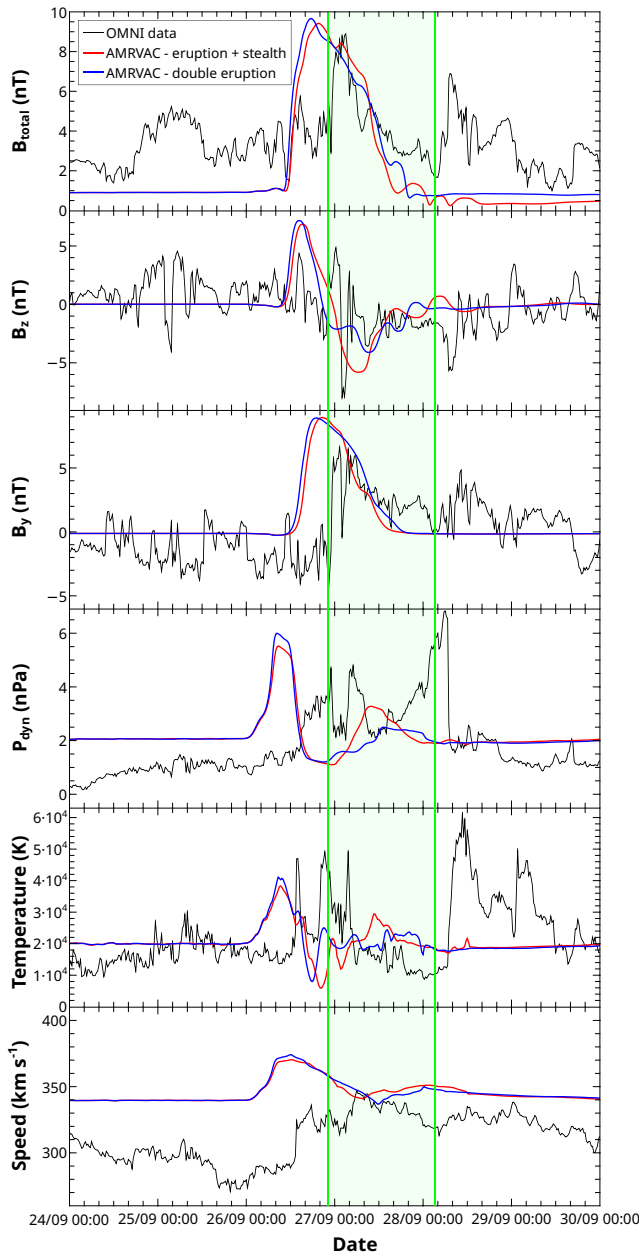


Figure 4.10: In situ measured values of the magnetic field components, dynamic pressure, temperature, and speed of the solar wind (top to bottom) taken from the OMNI database (black line). Also plotted are simulation data in the eruption + stealth (red line) and double eruption (blue line) cases propagated in the slow wind and taken at 1 AU. The green highlighted area approximately delimits the ICME. The dates on the X axis are from 2009.

in Fig. 4.10), which is defined as half the mass density multiplied by the square of the total speed of the solar wind. The observed proton temperature also presents an increase in the frontal part, followed by the usual lower values inside the flux rope, a signature observed in a large percentage of ICMEs (Richardson & Cane 1995; Zurbuchen & Richardson 2006). The simulations do not show such an extended interval of low temperatures due to the trailing plasma blobs, but they do exhibit the decrease in temperature. The final panel of Fig. 4.10 describes the expansion of the magnetic cloud through the faster front and lower speed of the tail.

The arrival time of the fronts of the CMEs at 1 AU is very similar for both simulated cases (double eruption and eruption + stealth), with a difference of only 20 min in magnetic field components, which is given by the slightly different eruption times. This is expected because the different eruption times of the CMEs are a consequence of the extremely small variation in the triggering shearing speed when there is a similar background wind and a higher amplitude of v_ϕ resulting in a faster flux rope formation and ejection. The difference in arrival time between the simulations and observations is ~ 10 hours. This difference occurs due to the differently modeled background solar wind speed as compared to the observed solar wind, but seems to be a typical error for such simulations (see, e.g., Mays et al. 2015). Nevertheless, this is a surprisingly good result considering that the wind was 2.5D simulated to only approximately match the 1 AU in situ measured speed. Furthermore, all the extracted parameters qualitatively fit the observed variables.

The fact that the two discussed simulations show good correlation with observations suggests that the initial setup is realistic enough to further investigate other eruptive scenarios. We are also interested in analyzing how the second CME influences its precursor, and to do so we simulated a single erupting flux rope, as previously described in Section 4.4. Furthermore, we investigated how a faster background solar wind would influence the propagation of such shear-induced CMEs, and we focus in the next part of this section on the five simulations as an independent result, rather than comparing them with the observations. The five discussed scenarios are illustrated in Section 4.4.

For each of these simulations, the magnetic field components were extracted in the equatorial plane at $75 R_\odot$ (Fig. 4.11) and at $215 R_\odot$ (1 AU, Fig. 4.12). For an easier comparison, the curves have been shifted in time and aligned with those of the last arriving CME, which is always the single eruption inserted into the slow solar wind. In both figures, B_{total} and B_y have their fronts aligned, the B_z curves are aligned at the point where the values change sign inside the first flux rope, and in Fig. 4.12 plasma beta curves are aligned at their minima. The process of aligning the curves leads to a loss of the information of arrival time at the respective distances, and so we note those explicitly in Table 4.2.

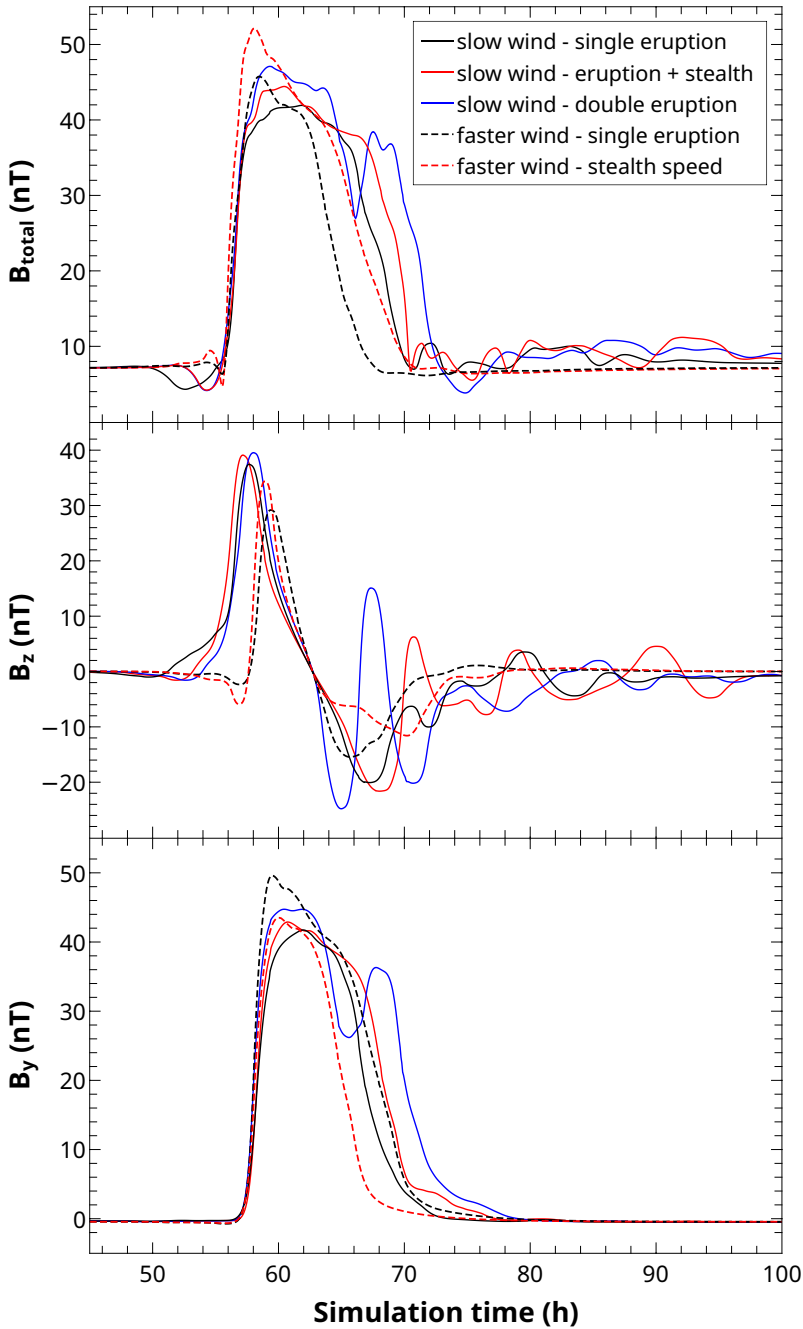


Figure 4.11: Magnetic field components simulated in all five cases, taken on the equatorial plane at $75 R_{\odot}$. All simulation data are shifted and aligned with the last arriving CME, which occurs in the slow wind, single eruption case. B_{total} and B_y have their fronts aligned, whereas B_z is aligned at the point where the values change sign inside the first main CME.

Table 4.2: Arrival times of the total magnetic field dip (followed by enhancement) of all simulated CMEs at $75 R_{\odot}$ and at $215 R_{\odot}$. Here, SW = slow wind and FW = faster wind.

Eruption type	Arr. time at $75 R_{\odot}$	Arr. time at $215 R_{\odot}$
Single er. SW	52.6 h	124.8 h
Stealth er. SW	48.13 h	119.2 h
Double er. SW	48.13 h	118.53 h
Single er. FW	49.4 h	113.93 h
Stealth speed FW	45.4 h	109.67 h

Table 4.2 was created using the arrival times of the minimum of the small dip that is created in front of the total magnetic field due to turbulence and compression of the equatorial current sheet ahead of the CME, and therefore this dip might not correlate precisely with the front of CMEs. We used this feature because of its precision, as compared to the magnetic field enhancement which would require a subjective choice of starting time. However, the time difference is insignificant, namely of the order of tens of minutes.

The total magnetic field taken at $75 R_{\odot}$ presents some major differences between the eruptions inserted in the slow and faster wind, namely in the widths of the ICMEs and the presence or absence of following plasma blobs. The double eruption case exhibits the widest ICME structure due to the yet-to-be-reconnected second CME, whereas the single eruption in the faster wind is the shortest in time. However, the stealth speed case presents the largest total magnitude of magnetic field, both at $75 R_{\odot}$, and also at 1 AU (top panel of Fig. 4.12). The weakest magnetic field is found in the single eruption case of the slow wind, both at Mercury and Earth. The signatures seem to be sharper in the faster wind cases than in the slow wind ones, which is probably related to the compression of the front attributed to the higher speed of CMEs and denser background solar wind. The second flux rope is still present in both double eruption and stealth ejecta cases, but can only be clearly distinguished in B_{total} and B_y in the first case. On the other hand, B_z (middle panel of Fig. 4.11) shows a larger variation and more clearly indicates the flux ropes erupting in the trail of the first CME in the slow wind cases.

The plasma blobs appear to be well defined in the B_z component, but in B_y there is almost no difference in the tail between the slow and faster wind cases, and so the blobs are not visible in this component either at $75 R_{\odot}$ (bottom panel of Fig. 4.11) or at $215 R_{\odot}$ (third panel of Fig. 4.12).

We propose a possible explanation for the absence of plasma blobs in the faster

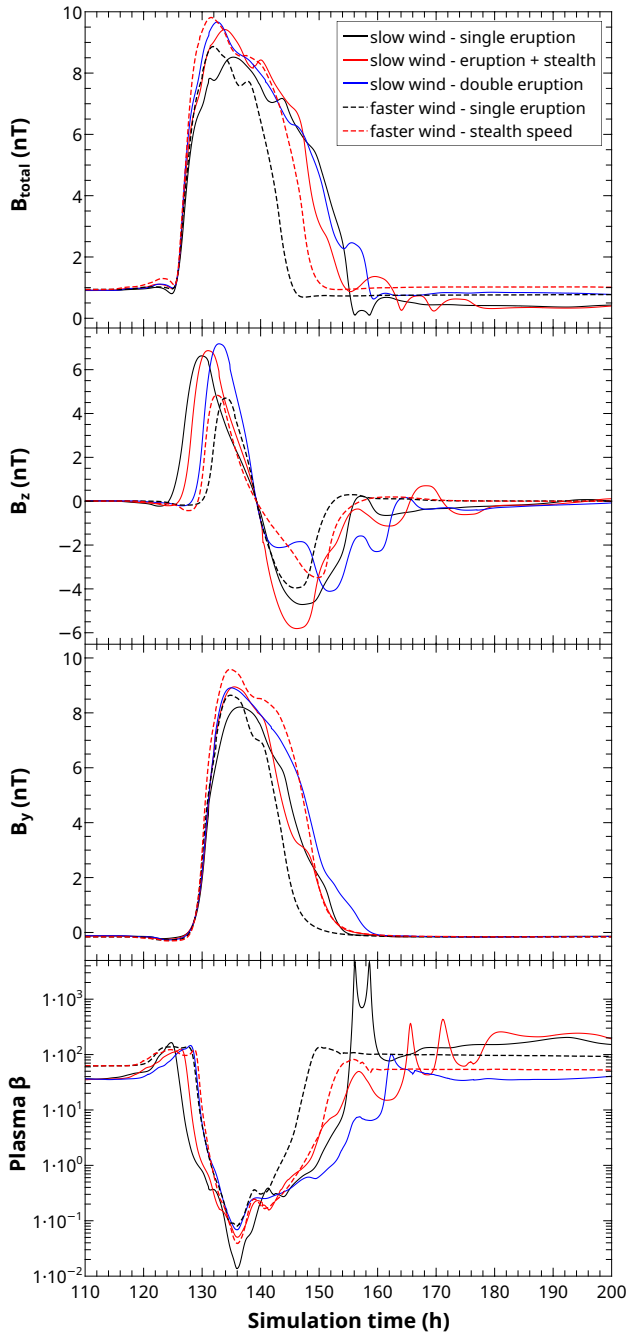


Figure 4.12: Magnetic field components simulated in all five cases, taken on the equatorial plane at 1 AU. The magnetic field components are overlapped in the same way as in Fig. 4.11, and we overlapped the minima of the plasma beta curves with the curve of the slow wind, single eruption case.

wind scenarios. The first CME is deflected towards the equator in all simulations, thereby compressing the northern arcade. In the faster wind configuration, this structure does not extend as far in the slow wind, and is not affected as much by the CME; therefore, it does not relax to the initial state, because it was not as perturbed. In the slow wind cases, the height of the northern arcade is greatly reduced during the deflection of the first CME, and in the process of returning to its initial state, it compresses the current sheet, inducing reconnection and creating plasma blobs just above the streamer cusp. This suggests the blobs may be indicators of more closed magnetic structures in the source region before the eruption.

It is interesting to note that the amplitude of the negative B_z component is smaller for the faster solar wind cases than for the slower wind scenarios. Also, the weakest negative B_z is found in the stealth speed simulation and is due to the second shear-triggered CME that reconnects with the trailing part of the first one. Comparing this to the total magnetic field, we can see that the contribution of B_z is not as significant as the other components, in particular B_y . In this 2D visualization, the B_y component is equivalent to B_ϕ , and is the axial or toroidal magnetic field along the center of the flux rope, while B_z is the azimuthal field (twist or poloidal component). Therefore, B_y is a consequence of the shear component of the magnetic field introduced by the v_ϕ boundary motions, whereas B_z originates from the reconnection of overlying streamer flux with itself, in the process of creating the twisted flux rope. The overlying streamer flux is larger in scale than the low-lying shear component, and therefore has lower field magnitude, which is also true in many flux rope models used to fit in situ data (e.g. Lepping et al. 1990; Burlaga 1988). This also explains the presence of the second peak in B_y in the double eruption case, because the second CME is triggered by the shearing motions and its flux rope is created close to the inner boundary. This characteristic of showing an axial field magnitude larger than the twist field magnitude also propagates to 1 AU, and is an important factor in estimating the geoeffectiveness of the simulated CMEs in Section 4.6.

The interaction with the background solar wind until 1 AU and the latitudinal expansion and radial compression of the flux ropes led to several changes in the ICME signatures. The B_z components in the faster wind cases are more symmetric with respect to the center of their flux ropes, between the positive and the negative values. However, they still carry the lowest absolute values of all the simulations, as can be seen in the second panel of Fig. 4.12. The last panel shows the ICMEs lengths through the plasma beta parameter, which usually shows a decrease inside the magnetic cloud due to the enhanced magnetic field (Lepping et al. 2006), and it is clearly seen that the single eruption inserted in the faster wind is the most compressed and short flux rope, followed by the

stealth speed case. The slow wind simulations present larger flux ropes, as well as plasma blobs following the main eruptions, distinguished by the peaks and oscillations in plasma beta. Some curves might present stronger peaks than others, but this only indicates that the selected trajectory through the simulation runs close to the center of these flux ropes, or almost through the null points between flux ropes, where there is approximately zero magnetic field. The well-known decrease in plasma beta inside the main ICME (Manchester et al. 2017) occurs in all simulations.

4.6 Geoeffectiveness

The last topic of this Chapter is our investigation of the potential impact of the simulated CMEs on Earth's magnetosphere. One way of quantifying the geoeffectiveness of CMEs is through the *Dst* index, which measures changes in the horizontal component of the magnetic field at ground level (Sugiura & Kamei 1991), and can be predicted from solar wind parameters using various empirical models. Depending on the number of mechanisms and parameters taken into consideration, these models can be rather rudimentary (Burton et al. 1975), or fairly comprehensive, as in the algorithm of Temerin & Li (2002, 2006). We chose to compute our simulated *Dst* using an intermediate model introduced by O'Brien & McPherron (2000), which achieves a sufficient level of accuracy when compared to the measured values of *Dst* taken from the World Data Center at Kyoto University¹⁰. The three main parameters that contribute, in this description, to the geoeffectiveness of interplanetary structures are the speed of the incoming solar wind, the N-S component of the magnetic field, and the dynamic pressure (Srivastava & Venkatakrishnan 2004). Depending on the sign of B_z , the product between the first two variables provides the y component of the solar wind convective electric field (VB_S) in geocentric solar magnetospheric (GSM) coordinates (Thompson 2006b), as follows:

$$VB_S[\text{mV m}^{-1}] = \begin{cases} |VB_z|, & B_z < 0 \\ 0, & B_z \geq 0. \end{cases} \quad (4.1)$$

This electric field uniquely determines the rate of ring current injection function Q :

$$Q[\text{nT h}^{-1}] = \begin{cases} a(VB_S - E_c), & VB_S > E_c \\ 0, & VB_S \leq E_c \end{cases}, \quad (4.2)$$

¹⁰<http://wdc.kugi.kyoto-u.ac.jp/dstdir/>

where $a = -4.4 \text{ nT m h}^{-1} \text{ mV}^{-1}$ and $E_c = 0.49 \text{ mV m}^{-1}$. The corrected Dst index (Dst^*) is defined as:

$$Dst^* = Dst - b\sqrt{P_{dyn}} + c, \quad (4.3)$$

where b is a pressure correction term of value $7.26 \text{ nT}(\text{nPa})^{-1/2}$, and c is a constant that accounts for the quiet day currents. The approximate evolution in time of the corrected Dst index is given by the discrete form of the Burton equation:

$$Dst^*(t + \Delta t) \approx Dst^*(t) + \left[Q(t) - \frac{Dst^*(t)}{\tau} \right] \Delta t, \quad (4.4)$$

where τ is the recovery storm time and was considered by O'Brien & McPherron (2000) to show the best fit to data in the following form:

$$\tau(\text{hours}) = 2.4 \exp \left[\frac{9.74}{4.69 + VB_S} \right]. \quad (4.5)$$

The change in the dynamic pressure term determines the sudden commencement (the initial positive excursion in Dst at the start of the storm) amplitude, as $Dst^*(t + \Delta t)$ should increase because of the difference in this correction term.

In the case of our simulations, the steady background solar wind should produce no change in the Dst index, such that $Dst^*(t + \Delta t) = Dst^*(t)$, and the initial value before the start of the ICME effect should also be zero. From these conditions, we find two separate c constants (from Eq. 4.3) for our simulations, with values of 10.44 nT for the slow wind and 15.77 nT for the faster wind. These values differ from the ones computed by Burton et al. (1975) and O'Brien & McPherron (2000), of namely 20 nT and 11 nT , respectively, because of the different observational datasets used in their studies. This discrepancy is not unexpected because our winds are uniform in time whereas the in situ measured data reveal a wind that varies greatly over time.

We used the simulated data (speed, B_z , and dynamic pressure) in all of the above equations and computed a predicted Dst index that our CMEs would create. Figure 4.13 shows a comparison between the OMNI hourly Dst index and the hourly averaged Dst computed from simulation data extracted every 4 min, in the slow wind cases of eruption + stealth and double eruption. Given the weakness of the observed CMEs (slow speed and only brief intervals of modest southward B_z (Fig. 4.10)), the corresponding ICME did not create a geomagnetic storm ($Dst \leq -30 \text{ nT}$, Loewe & Pröls 1997; Gonzalez et al. 1994), reaching a minimum measured Dst of only -16 nT . As mentioned in Sect. 4.5, the simulated trailing flux ropes reconnected with the tail of the first CME, and

therefore the negative B_z component in the double eruption case was not as strong as in the eruption + stealth scenario (see Fig. 4.10 and 4.12). It is well known that a strong decrease in the negative B_z results in a stronger Dst (e.g. Tsurutani et al. 1988). In accordance with this correlation, the double eruption case resulted in a less geoeffective ICME than the eruption + stealth scenario, with Dst values resembling those recorded at Earth (see Fig. 4.13).

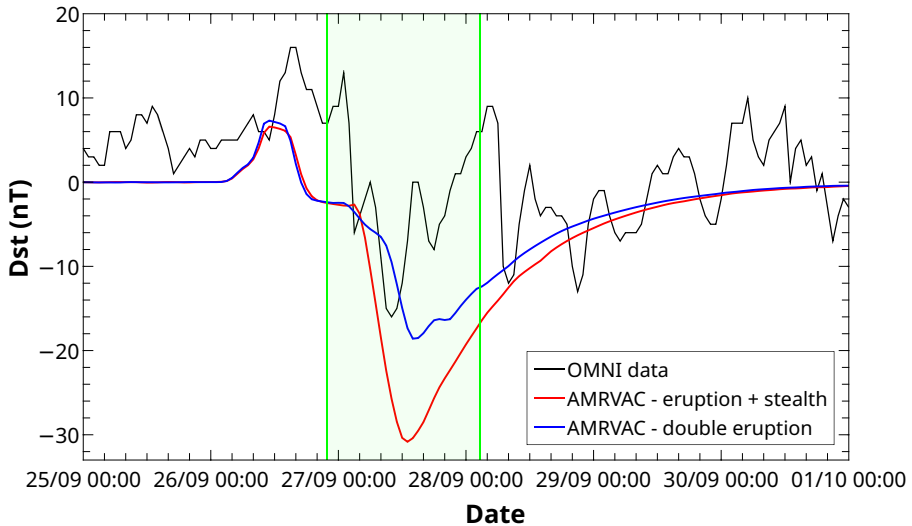


Figure 4.13: Comparison of hourly Dst index from observed database (black line) with modeled Dst using simulation data, in the eruption + stealth (red line) and double eruption (blue line) cases, propagated into the slow solar wind. The green highlighted area approximately delimits the ICME arrival. The dates on the X axis are from the year 2009.

Most previous studies on this topic concluded that more intense geomagnetic storms were associated with multiple interacting CMEs, rather than single CMEs (Burlaga et al. 1987; Zhang et al. 2007; Gopalswamy et al. 2007, and many others). Surprisingly, our simulations highlight that the presence of interacting CMEs does not necessarily imply strong geoeffectiveness, at least in the case of slow CMEs. In our simulations, the eruption + stealth scenario is predicted to create a weak geomagnetic storm (minimum $Dst = -30.83$ nT), whereas the double eruption is predicted to be even less geoeffective, with minimum $Dst = -18.6$ nT. However, this does not necessarily contradict the previous studies, quite the contrary. Their direction of analysis was mainly starting from a geomagnetic storm back to its origin on the Sun, which means that our simulated scenarios would not even fit in their studied cases. In the

opposite direction, i.e. trying to predict the impact that CMEs would have on Earth, starting from remote sensing observations, these simulations could explain some issues in the current models. One example of such a study is the model of Dumbović et al. (2015) which uses solar parameters to assess the occurrence probability of geomagnetic storms, which also contains false alarms, that is, CMEs that have the potential to impact Earth but did not produce any storm. Our simulations might be able to explain some of these false positive events, which should not be disregarded from a forecasting point of view, despite their lower-than-usual geoeffectiveness.

In order to analyze the different contributions of the solar wind parameters to the computed Dst , we plotted the evolution in time at 1 AU in the equatorial plane of the simulated B_z magnetic field component, dynamic pressure, and Dst in Fig. 4.14. The first feature that reaches Earth is a jump in pressure caused by an increase in speed in the first part of the ICME, which creates a compressed front. This small sudden storm commencement (SSC; e.g. Mayaud 1975; Curto et al. 2007) can also be seen in the OMNI data in Fig. 4.13, during the hours ahead of the green highlighted area. Before B_z turns negative, the only contribution to the Dst is given by the dynamic pressure, with the amplitude of $b\Delta P_{dyn}^{1/2}$, as also described initially by Burton et al. (1975). Once B_z turns negative and the interplanetary electric field (VB_S) overcomes the 0.49 mV m^{-1} threshold, the injection function Q becomes negative and starts decreasing the Dst , creating the main phase of the storm. We note the oscillations in Dst after its minimum value in the top panel of Fig. 4.14, which are imposed by the variations in B_z . On the other hand, in the bottom panel, the decrease in Dst just after SSC and increase during the main phase are both imposed by the profile of the dynamic pressure, which increases in response to plasma pile-ups. This contribution is indicated by the black arrows and can be more easily observed in the recovery phase of the storm, when B_z is positive again and the energy injection from the solar wind into the magnetosphere has ended.

We computed and compared the Dst indices for all the simulations, and their evolution is shown in the top panel of Fig. 4.15. The interplay between the two important aforementioned parameters slightly changes the order of the strength of the geomagnetic storms as compared to the B_z minima plotted in Fig. 4.12. The only difference is that the single eruption inserted into the faster wind becomes slightly more geoeffective than the double eruption in the slow wind. The least negative B_z (faster wind, stealth speed case) still creates the weakest geoeffectiveness, whereas the most negative B_z (slow wind, eruption + stealth case) induces a weak geomagnetic storm with the lowest Dst of all the simulations.

Our proposed explanation for the overall low geoeffectiveness of the simulated

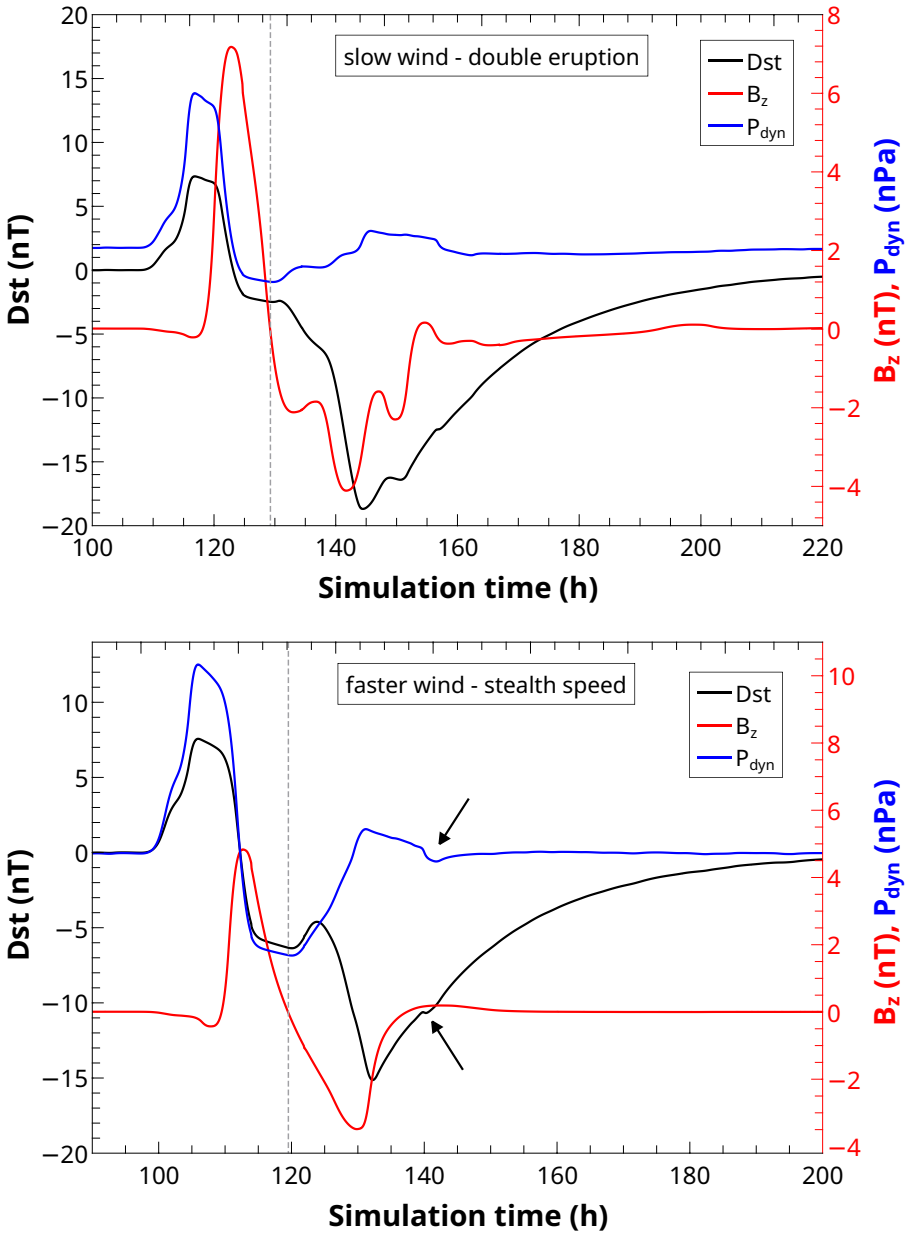


Figure 4.14: modeled Dst using simulation data (black line, left axis), the B_z component of the magnetic field (red line, right axis), and the dynamic pressure (blue line, right axis) in the case of the slow wind - double eruption (top panel) and faster wind - stealth speed (bottom panel). The curves have not been overlapped, and so they indicate the actual simulated arrival time. The gray dashed line shows the polarity reversal of B_z .

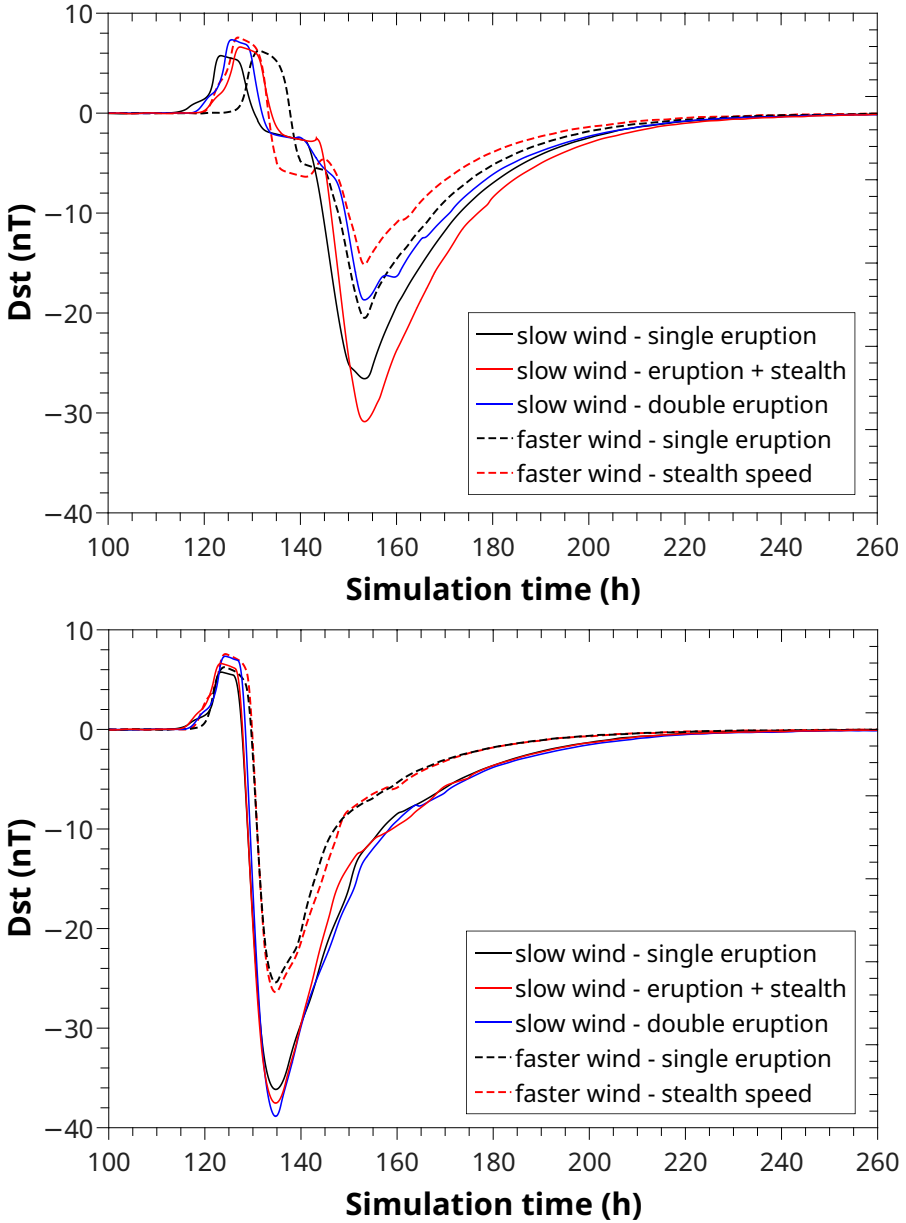


Figure 4.15: modeled Dst using simulation data (top panel) and using the B_z component with the reversed sign (bottom panel). The minima of the curves have been aligned onto that of the last occurring minimum, which was the case of the single eruption in the slow wind.

eruptions is the reduction in the negative trailing B_z component due to the magnetic reconnection with flux ropes appearing in the wake of the first CME. To test this hypothesis, we reversed the polarity of B_z in the slices taken at 1 AU, such that the first CME would impact Earth with the negative front, and the reconnected part would be the positive one. We recomputed the Dst using this new magnetic configuration, but keeping the same dynamic pressure and speed; the resulting values are plotted in the bottom panel of Fig. 4.15. As expected, in all simulations the frontal CME becomes more geoeffective, and all eruptions inserted into the slow wind produce weak geomagnetic storms, with an emphasis on the double eruption which now presents the lowest Dst minimum. Interestingly, the strength of the storms is exactly correlated with the positive amplitude of the B_z component in Fig. 4.12, which would now become the negative front. Another aspect is the abrupt decrease in Dst immediately after the SSC, meaning that the dynamic pressure did not exhibit a contribution as important as in the previous case, which is because the energy injection function turned negative as soon as the flux ropes arrived at Earth. This also led to a smaller variation in the index values between the simulations as well as during each individual storm. Ultimately, we can extract a final detail from Fig. 4.15. Even though the single eruption inserted into the faster wind was the only one that did not present any following flux ropes and therefore lacked the trailing magnetic reconnection, it still changed geoeffectiveness along with the B_z reversal of sign. Our understanding of these simulation results is that the frontal part of a CME has more impact on Earth's magnetosphere than the elongated tail and, as previously noted (e.g. Fenrich & Luhmann 1998), this is exacerbated when it arrives with a negative N-S component of the magnetic field.

4.7 Summary and Discussion

In this Chapter, we describe and analyze five simulations performed using the code MPI-AMRVAC, of which three were propagated into a slow wind, and two were inserted into a faster and denser background wind. The model configuration is based on an MCME event on 21-22 Sept 2009 that erupted approximately towards Mercury and Earth, providing an opportunity to compare the in situ data between simulations and two spacecraft. Initial simulations of this event were presented in Chapter 3, where good agreement was found between coronal remote sensing observations and the double eruption and eruption + stealth scenarios ejected into the slow wind. In this Chapter, we propagate these two cases out to 1 AU. At 0.3 AU, the eruption with the stealth ejecta shows the best fit to in situ data taken from MESSENGER, which is surprising when compared to the results of Chapter 3 where we found

a better fit of white-light coronagraph observations with the double eruption scenario. This can be attributed to our 2.5D setup, as the slices are not affected by the longitudinal difference between CME propagation and spacecraft, and therefore in the MESSENGER data some flux ropes might be missed due to their narrow dimensions. The stealth ejecta is also partially missed in simulations, which is attributed to the slice being taken at the equator, while the current sheet in which the CME propagates is slightly shifted northward. At Earth, the differences between the two simulations are even smaller because of the influence of the solar wind throughout the propagation. Taking all these factors into consideration, it is difficult to distinguish the triggering mechanism responsible for the second observed CME, making the distinction between stealth ejecta and source CMEs even more unclear. This highlights the need for better remote sensing instruments with higher resolution and cadence, which may in the future be able to observe much fainter structures, allowing us to better understand these stealth CMEs.

We also analyze the influence of the solar wind on the eruptions by numerically simulating two more scenarios of shear-induced CMEs in a faster and denser background wind. A first observation we extracted from this new configuration was a change in the initial magnetic structure, even though we have not interfered with the magnetic components, leading to an opening of the overall streamer. Even if our magnetic solution is not originating from a potential field, this could still indicate a non-unique solution for extrapolations that compute the coronal magnetic field solely from line-of-sight magnetic field converted to B_r , as in the potential field source surface (PFSS, Schatten et al. 1969) model. The PFSS solution also depends on both lower and upper boundary conditions of the other non-radial components of the magnetic field, and according to those, one can obtain different resulting magnetic configurations. In order to better reproduce the field lines in the solar atmosphere, one might need to better constrain the plasma solution by providing the other B components, or other parameters such as density and/or temperature from observations. Judge et al. (2021) described a method of inversion of spectropolarimetric data from observed coronal plasma at the limb of the Sun in order to obtain the magnetic field components inferred from measured Stokes parameters I , Q , U , and V . Such a method can be used to invert physical parameters from coronal observations taken by the novel Daniel K. Inouye Solar Telescope (DKIST, Rimmele et al. 2020), and an inversion algorithm is currently being prepared by Paraschiv & Judge (2021).

The change in our simulated magnetic field configuration also affected the subsequent eruptions, by creating two CMEs from the applied shear when using the v_0 value that resulted in a stealth ejecta in the slow wind case. There were also no plasma blobs appearing in the faster wind simulations, making them a possible indicator of the initial magnetic structure.

In addition, we computed the Dst index from our simulations using an empirical formula into which we introduced the speed, the B_z component of the magnetic field, and the dynamic pressure. The measured Dst is both qualitatively and quantitatively reproduced by the double eruption scenario in the slow wind, as is the small SSC occurring before the drop in Dst . The computed recovery phase is longer and more gradual than the observed one, which we can attribute to another event developing after the passage of our ICME that again decreases the actual Dst . That second event was only identified in the in situ data and is not investigated in the presented study because it is of no current interest. We also analyzed the different parameters contributing to the computed Dst and concluded that the amplitude of a storm can be greatly influenced not only by B_z but also by the dynamic pressure. A very good representation of this statement is the two-step geomagnetic ‘storm’ created just from the arrival of one flux rope at Earth (stealth speed case), due to the interplay between the two variables, B_z and p_{dyn} . The low geoeffectiveness of the slow wind simulations was attributed to the magnetic reconnection in the tail of the CMEs, which made the trailing B_z less negative, leading us to study the Dst in the case where the CMEs arrived at Earth with reversed polarity of B_z . This change in the polarity of B_z increased the geoeffectiveness of all the simulated eruptions and decreased the contribution of the dynamic pressure to the overall trend of the storms, which now affected mainly the SSCs. Another finding from this study is that multiple CMEs might even have a reduced geoeffectiveness as compared to single CMEs, which could explain some false alarms encountered in storm predictions using solar parameters. In the next Chapter we will present the analysis of forces that contribute to the eruption of these CMEs, mergers between them, and their propagation to 1 AU.

Chapter 5

Interaction of coronal mass ejections and the solar wind. A force analysis

Abstract

Our goal is to thoroughly analyze the dynamics of single and multiple solar eruptions, as well as a stealth ejecta. The data were obtained through self-consistent numerical simulations performed in a previous study. We also assess the effect of a different background solar wind on the propagation of these ejecta to Earth. We calculated all the components of the forces contributing to the evolution of the numerically modeled consecutive coronal mass ejections obtained with the 2.5D magnetohydrodynamics module of the code MPI-AMRVAC. We analyzed the thermal and magnetic pressure gradients and the magnetic tension dictating the formation of several flux ropes in different locations in the aftermath of the eruptions. These three components were tracked in the equatorial plane during the propagation of the CMEs to Earth. The CMEs' interaction with other CMEs and with the background solar wind was also studied. We explain the formation of the stealth ejecta and the plasma blobs (or plasmoids) occurring in the aftermath of solar eruptions. We also address the faster eruption of a CME in one case with a different background wind, even when the same triggering boundary motions were applied, and attribute this to the slightly different magnetic configuration and the large neighboring arcade. The thermal pressure gradient revealed a shock in front of these slow eruptions, formed

during their propagation to 1 AU. The double-peaked magnetic pressure gradient indicates that the triggering method affects the structure of the CMEs and that a part of the adjacent streamer is ejected along with the CME.

This chapter is based on the paper accepted for publication D.-C. Talpeanu, S. Poedts, E. D’Huys, M. Mierla, Ian G. Richardson (March 2022). "Interaction of coronal mass ejections and the solar wind. A force analysis". In: *Astronomy&Astrophysics*. The text was adapted in this thesis manuscript in order to avoid repetitions. D.-C. Talpeanu performed the numerical simulations and computations, the force analysis of numerical data, and prepared the manuscript.

5.1 Introduction

CME interactions have been observed near the Sun and in interplanetary space. Using remote-sensing observations and in-situ data, such interactions between two successively launched CMEs have been tracked and analyzed from the Sun to Earth by several authors, such as Temmer et al. (2012) and Temmer et al. (2014), and all the way to Saturn by Palmerio et al. (2021). The launch of the twin STEREO spacecraft in 2006 has prompted studies (e.g. Liu et al. 2014; Webb et al. 2013) of successive CMEs using the multi-viewpoint capabilities provided by instruments on these spacecraft, in combination with in-situ data. Liu et al. (2014) also analyzed two CMEs interacting near 1 AU that resulted in a two-step geomagnetic storm driven by their complex ejecta.

The mechanisms by which ICMEs interact have been investigated using numerical simulations by several authors, such as Török et al. (2011), who modeled two sympathetic eruptions based on an observed event; Lugaz et al. (2017b) who simulated the interaction of two CMEs from the Sun to Earth; and Bemporad et al. (2012), who performed MHD simulations to physically explain the origin of multiple CMEs from an asymmetric coronal field configuration.

In Chapter 3 we performed self-consistent 2.5D MHD numerical simulations of consecutive CMEs obtained by applying time-dependent shearing motions at the inner boundary of the computational domain, along the southernmost polarity inversion line of a triple arcade magnetic structure. One of the eruptions was a blob-like stealth ejecta, occurring in the trailing current sheet created by the passage of a first CME. In Chapter 4 we investigated the effect of a faster and denser background solar wind on the initial magnetic configuration and the resulting eruptions obtained through the same triggering mechanism. Firstly,

we reported a split of the initial overlying streamer into a northern arcade and a southern pseudostreamer. Secondly, when applying the same shearing speed amplitude as in Chapter 3, the flux ropes formed earlier and the associated CME had a higher speed in the faster solar wind case. Lastly, the stealth ejecta no longer formed, nor did the plasma blobs (or plasmoids) following the main eruptions in the trailing current sheet.

It is known that the upward magnetic and plasma pressure gradients, balancing the downward magnetic tension and gravity, keep magnetic structures and filaments in equilibrium in the solar atmosphere (Chen 1996; Forbes 2000; Schmieder et al. 2013). The exact interplay and imbalance between all these forces that eventually drive CMEs has not been extensively documented in the literature. Cargill & Schmidt (2002) and Cargill (2004) investigated the forces acting on numerically simulated CMEs during propagation, as well as the coupling between the CMEs and the background solar wind expressed through the aerodynamic drag (e.g. Chen & Garren 1993; Cargill et al. 1995). The few more recent studies of these physical processes include Shen et al. (2012), who analyzed the forces causing acceleration and deceleration of CMEs, and Hosteaux et al. (2021), who studied the deformation and erosion of CMEs during their evolution. Furthermore, Kay & Nieves-Chinchilla (2021) presented the first results of their numerical code that simulates the propagation, expansion, and deformation of a CME in the interplanetary medium, and quantified the contributions of each of the imposed forces to these processes. Closer to the Sun, Lynch et al. (2009) explain the rotation of a CME during eruption by analyzing the forces involved. The review of Manchester et al. (2017) summarizes the ways in which CMEs and their interplanetary counterparts evolve during their journey through the solar wind.

In order to thoroughly explain the differences in dynamics observed in Chapters 3 and 4, we calculate all the contributing forces that govern the resulting eruptions. We also investigate the CME-CME and CME-solar wind interactions during their propagation away from the Sun. The numerical set-up and the methods used are described in Section 2. The detailed force analysis during CME onset and evolution is provided in Section 3. Finally, Section 4 contains the summary and our conclusions.

5.2 Numerical MHD code, methods and simulations

5.2.1 Numerical setup

The goal of this follow-up study is to analyze and understand the forces dominating the CMEs simulated and described in Chapter 4 from their eruption phase to their propagation in interplanetary space. Because the numerical setups are identical to those used in Chapter 4, we limit ourselves here to a few remarks about the code. If the results are to be reproduced, the mathematical description of the background solar wind, initial conditions and CME triggering method can be found in Chapters 3 and 4.

The CMEs are erupted into a bimodal background solar wind symmetric in the ϕ direction. The simulations were performed at two different background solar wind speeds and densities, which we refer to as slow wind and faster wind. These terms denote two separate configurations, rather than composite latitudinal parts of the same solar wind. In addition to the dipole field, a quadrupolar magnetic term was introduced in the initial and boundary conditions. The resulting coronal magnetic structure for the slow-wind case depicts an asymmetric triple arcade system embedded in a helmet streamer, as previously described in Chapter 3, Section 3.3. The two small arcades in the southern hemisphere constitute a local pseudostreamer, but due to its proximity to the large northern arcade, the pseudostreamer tends to follow the boundary of the northern arcade and helmet streamer. Thus, the pseudostreamer may be considered as part of a combined helmet streamer. When the momentum was increased in order to obtain the faster solar wind configuration, the helmet streamer broke up into the northern arcade and the southern pseudostreamer, without modifying the magnetic field boundary conditions. The pseudostreamer was then considered as a separate entity since it is directed almost radially away from the Sun and is less influenced by the northern structure. These two simulated configurations are shown in Fig. 4.2.

When the background solar winds reached steady state, CMEs were obtained by applying time-dependent shearing motions described in Chapter 3, Section 3.3.

5.2.2 Simulated eruptions

We analyze here five simulations performed in Chapter 4 (see Figures 4.4, 4.5, 4.6, 4.7, and 4.8), which are briefly described in this subsection. In all cases, the first erupting flux rope is driven by the boundary shearing motions that

increase the magnetic pressure inside the southernmost arcade, causing it to rise and expand. This affects the initial balance between the magnetic tension and the magnetic pressure gradient and compresses the magnetic field locally. The numerical resistivity induces reconnection between the sides of the arcade, creating a flux rope that begins to erupt. Under the influence of the southern polar magnetic pressure, the erupting flux rope is deflected towards the equator and propagates almost radially inside the equatorial current sheet beyond several solar radii; this height depends on the respective scenario. The differences in amplitude of the applied shearing speed result in the occurrence or absence of secondary CMEs. We investigated in total five simulations, that are described in more detail in Chapter 4, Section 4.4.

5.3 Force analysis

In order to explain the evolution and interactions of the simulated eruptions, as well as the formation of different flux ropes in certain situations, we calculated and analyzed the individual forces contributing to their dynamics. The mathematical description of the force densities in a unit volume is given by the MHD momentum equation,

$$\rho \frac{d\mathbf{v}}{dt} = -\nabla P_P + \underbrace{\mathbf{j} \times \mathbf{B}}_{\text{Lorentz force}} + \rho \mathbf{g} = -\nabla P_P - \underbrace{\nabla \frac{|B|^2}{2\mu_0}}_{-\nabla P_B} + \underbrace{\frac{(\mathbf{B} \cdot \nabla) \mathbf{B}}{\mu_0}}_{\mathbf{T}_B} + \rho \mathbf{g}. \quad (5.1)$$

Each component was calculated throughout the computational domain with their corresponding sign, since that represents their contribution to the total force. The first term on the right-hand side of the equation is the plasma pressure gradient, $-\nabla P_P$. The Lorentz force ($\mathbf{j} \times \mathbf{B}$) (in MHD the electric force is ignored) was decomposed into its constituents parts, the magnetic pressure gradient ($-\nabla \frac{|B|^2}{2\mu_0}$), which we denote as $-\nabla P_B$, and the magnetic tension ($\frac{(\mathbf{B} \cdot \nabla) \mathbf{B}}{\mu_0}$), which we write as \mathbf{T}_B . The last term ($\rho \mathbf{g}$) represents the gravity of the Sun and was added only to the radial component of the force.

We discuss and explain several interesting aspects of the simulations, using the calculated forces. The topics we examined are the following:

1. The faster eruption of CMEs in the faster solar wind cases, when the same shearing speed is applied as in the slow wind cases;

2. The formation of the stealth ejecta;
3. The occurrence of plasma blobs (or plasmoids) in the aftermath of eruptions, only in the slow wind cases;
4. The propagation of CMEs and their interaction with the background solar wind and with other CMEs.

5.3.1 Different CME eruption times for the two background solar winds

The first aspect we address is the quicker formation and eruption of CMEs in the faster solar wind cases, when the same shearing is applied as in the slow solar wind cases. As mentioned in Section 3.3, two shearing speeds of similar amplitudes were applied to the southernmost arcade of both background magnetic field configurations (and solar winds), and yet they resulted in different CME dynamics. The flux rope in the faster wind - single eruption case forms two hours earlier than in the slow-wind case, and the first flux rope in the stealth speed case is created an hour earlier than its equivalent eruption in the slow-wind

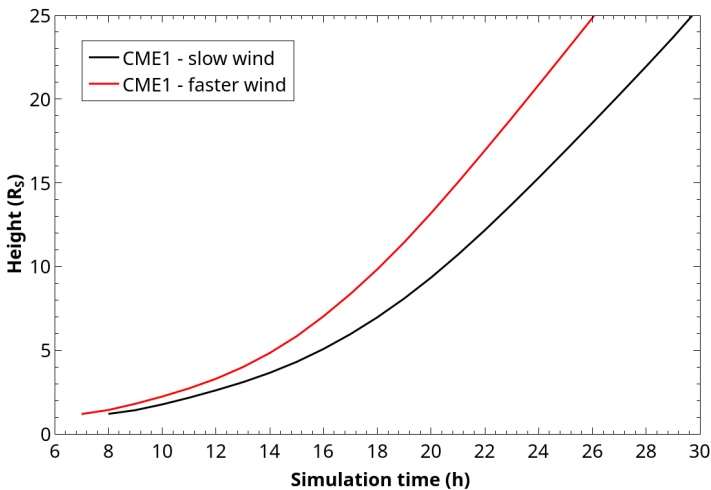


Figure 5.1: Height-time plot of the center of the flux rope associated with the first CME in the cases of slow wind - eruption + stealth (black line), and faster wind - stealth speed (red line). The height is calculated from the center of the Sun, and the simulation time is from the start of the shearing motions.

case (eruption + stealth). This second comparison is shown in Fig. 5.1, which shows the height of the center of the flux rope versus time; the steeper slope of the red line indicates a higher eruption speed of CME1 in the faster-wind case. It is also interesting to note that the temporal difference between the equivalent scenarios (between the two background winds) increases as the amplitude of the shearing speed decreases. The simulated shearing motions are intended to represent the accumulated footpoint displacement resulting from weeks of real differential rotation (Lynch et al. 2016), in addition to local photospheric movements strongly correlated to magnetic flux emergence (Wang et al. 2018). Our simulations indicate that the weaker these combined motions, the stronger the effect of the coronal magnetic environment on the dynamics of the flux ropes. The lower limit of this assumption would be that at some point, the shearing motions will not produce any eruption in the slow wind case, whereas a CME will still be created in the faster-wind configuration.

In order to analyze the results of our simulations, we calculated the forces in the relaxed background wind because (since we imposed approximately the same shearing speed) the triggering method cannot be the cause of the different eruption scenarios. We computed the forces in the entire domain for both solar winds and then extracted them at $1.5 R_{\odot}$ at all latitudes (see Fig. 5.2). This distance was chosen because it is just above the southernmost arcade and null point. We may therefore obtain the influence of the overlying coronal environment on the eruptions. The blue semicircle in Fig. 5.3 represents the location of the force values plotted in Fig. 5.2.

The top panel of Fig. 5.2 shows the initial difference between the two background solar wind simulations, specifically, a larger plasma pressure gradient in the faster wind case. This is caused by the approach we used to generate the faster wind by increasing the initial temperature of the simulated slow wind. The coded MHD equations governing the plasma dynamics are expressed in conservative variables, and so the temperature changes the momentum, and therefore the velocity as well as density. The left-most and right-most peaks indicated by the dashed blue lines at $\approx \pm 67^{\circ}$ denote compression regions between the latitudinal components of the slow and fast wind, which can also be seen as regions of enhanced electric current density in the maps of Fig. 5.3. The three intermediate peaks for the faster solar wind simulation (red line) lie at the borders of the northern arcade (at $\approx 35^{\circ}$ and $\approx 3^{\circ}$) and the current sheet created by the southern pseudostreamer (at $\approx -24^{\circ}$), also indicated by the white circles in the bottom panel of Fig. 5.3. These peaks clearly show the separation between the two magnetic structures. In contrast, the slow solar wind simulation (black line) only shows two peaks at the northern edge of the large streamer (at $\approx 46^{\circ}$) and the southern one (at $\approx -30^{\circ}$). These two peaks can be traced to the solar wind configuration by the white circles in the top panel of Fig.

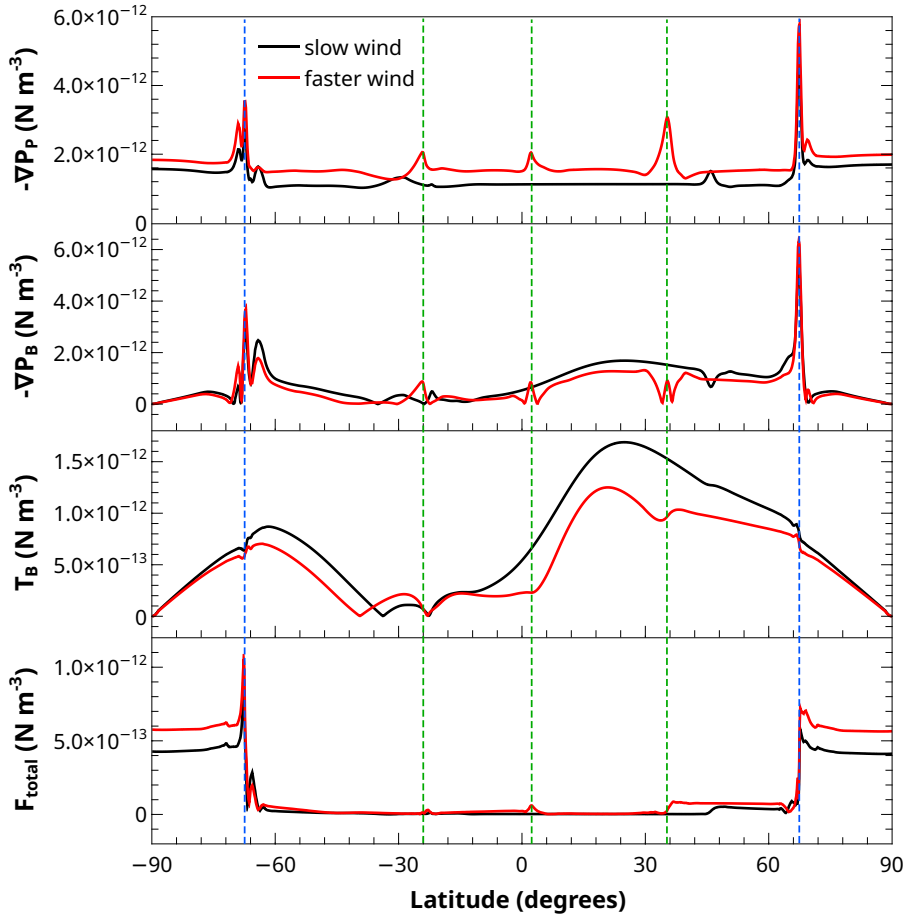


Figure 5.2: Forces extracted from the 1D cut at $1.5 R_{\odot}$ (blue semicircles in Fig. 5.3) in the cases of slow (black line) and faster background solar wind (red line). The force densities (top to bottom) are the following: plasma pressure gradient ($-\nabla P_P$), magnetic pressure gradient ($-\nabla P_B$), magnetic tension (\mathbf{T}_B) and total force (F_{total}). The dashed blue lines indicate the interface between slow and fast wind, here referred to as latitudinal components of the same background wind simulation. The dashed green lines represent peaks in $-\nabla P_P$ in the faster-wind case (here referred to as the separate simulation case), which is identified by the white circles in Fig. 5.3.

5.3. The second panel of Fig. 5.2 shows that there are no significant differences in $-\nabla P_B$ between the two background solar wind configurations, while the total

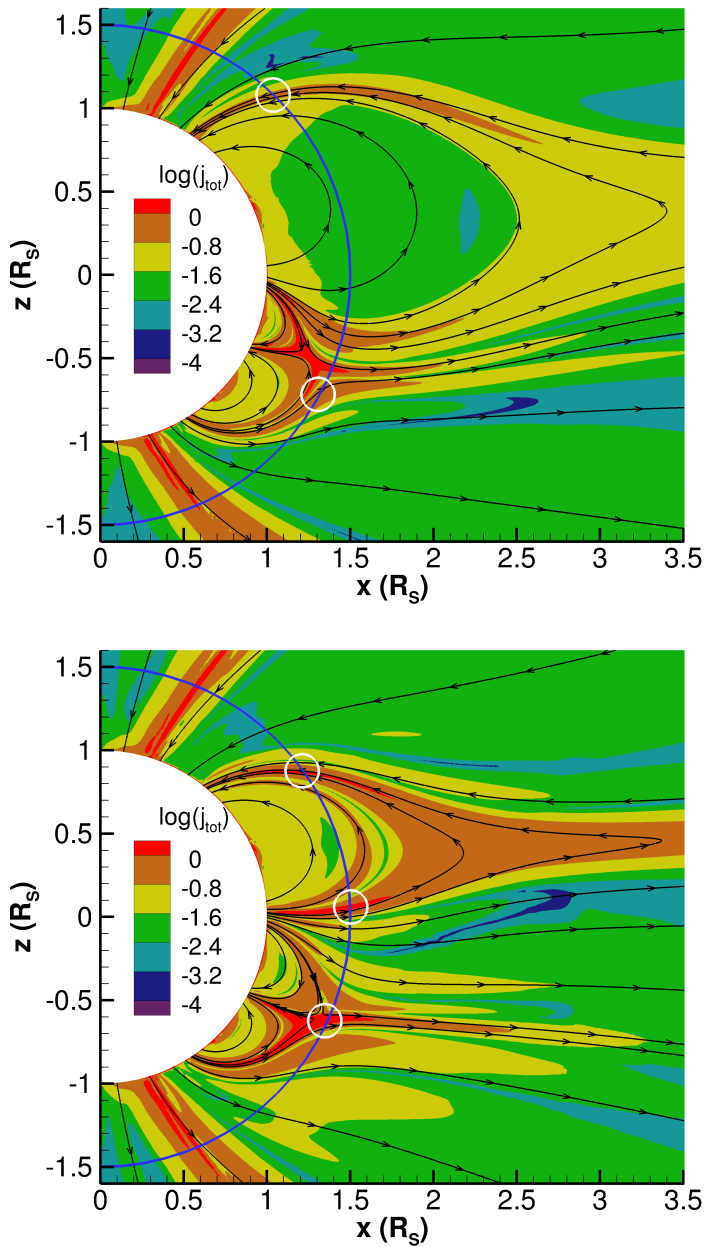


Figure 5.3: Simulation snapshots of the electrical current density (color scale) in the relaxed slow (top panel) and faster (bottom panel) background solar winds. The black lines represent selected magnetic field lines. The blue semicircles at $1.5 R_{\odot}$ are the cuts from where the forces in Fig. 5.2 were extracted. The white circles approximately indicate the locations of the $-\nabla P_P$ peaks in Fig. 5.2.

force in the bottom panel differs mainly in the fast solar wind region due to the faster and denser plasma, from $\approx \pm 67^\circ$ poleward. On the other hand, the magnetic tension in the third panel is much stronger in the slow-wind case than in the faster-wind case. It is also more extended in latitude because the larger northern arcade connects topologically to the other two smaller arcades (Fig. 5.3). As discussed below, this property of the configuration has an impact on the simulated eruptions, as shown in Fig. 5.4, which shows the forces that are present after the first CME is triggered by the applied shearing motions in the southern arcade. The snapshots are taken when the CME front is at $\approx 2 R_\odot$. In both the slow (top panel) and faster (bottom panel) solar wind cases, the CME is deflected towards the equatorial plane by $-\nabla P_B$ and \mathbf{T}_B surrounding the arcade, indicated in Fig. 5.4 by the blue and red vectors, respectively. The magnetic tension is oriented towards the equator in all of the southern part of the arcade, and $-\nabla P_B$ is pushing the CME from above in approximately the same direction. The resultant of these two vectors causes the CME to expand asymmetrically towards the north. In the slow solar wind cases (top panel of Fig. 5.4), this leads to magnetic reconnection between the CME flux rope and the northern arcade, creating large overlying (red) field lines. These give rise to the predominantly sunward magnetic tension (red vectors inside the red field line), which decelerate the eruption. In the faster solar wind case, the bottom panel of Fig. 5.4 clearly shows the magnetic separation between the CME and the northern streamer, as indicated by the red lines, which does not enclose the flux rope, enabling it to erupt more easily. This also facilitates the expansion of the southern arcade, explaining the quicker formation of the flux rope in the faster solar wind cases.

5.3.2 Formation of the stealth ejecta

In this subsection, we explain the formation of the stealth ejecta in the slow-wind case (eruption + stealth scenario). For this purpose, we calculated and analyzed the forces in the region of the current sheet trailing the first CME (CME1) in Fig. 5.5, which shows plasma β , magnetic field lines, and total force vectors at 16 h after the start of shearing. The important elements in this scenario are the first CME triggered by the shearing motions, one flux rope formed through the same mechanism, and another flux rope formed by the reconfiguration of the coronal magnetic field. Consistent with the sunward total force vectors (green), the second flux rope, indicated in Fig. 5.5 by the red circle, falls back to the Sun. The total force vectors also determine the motion of CME1 during its eruption away from the Sun. In this process, two current sheets are formed, one trailing CME1 extending to the second flux rope, and the second between the CME and the compressed northern arcade. Both are clearly depicted in Fig.

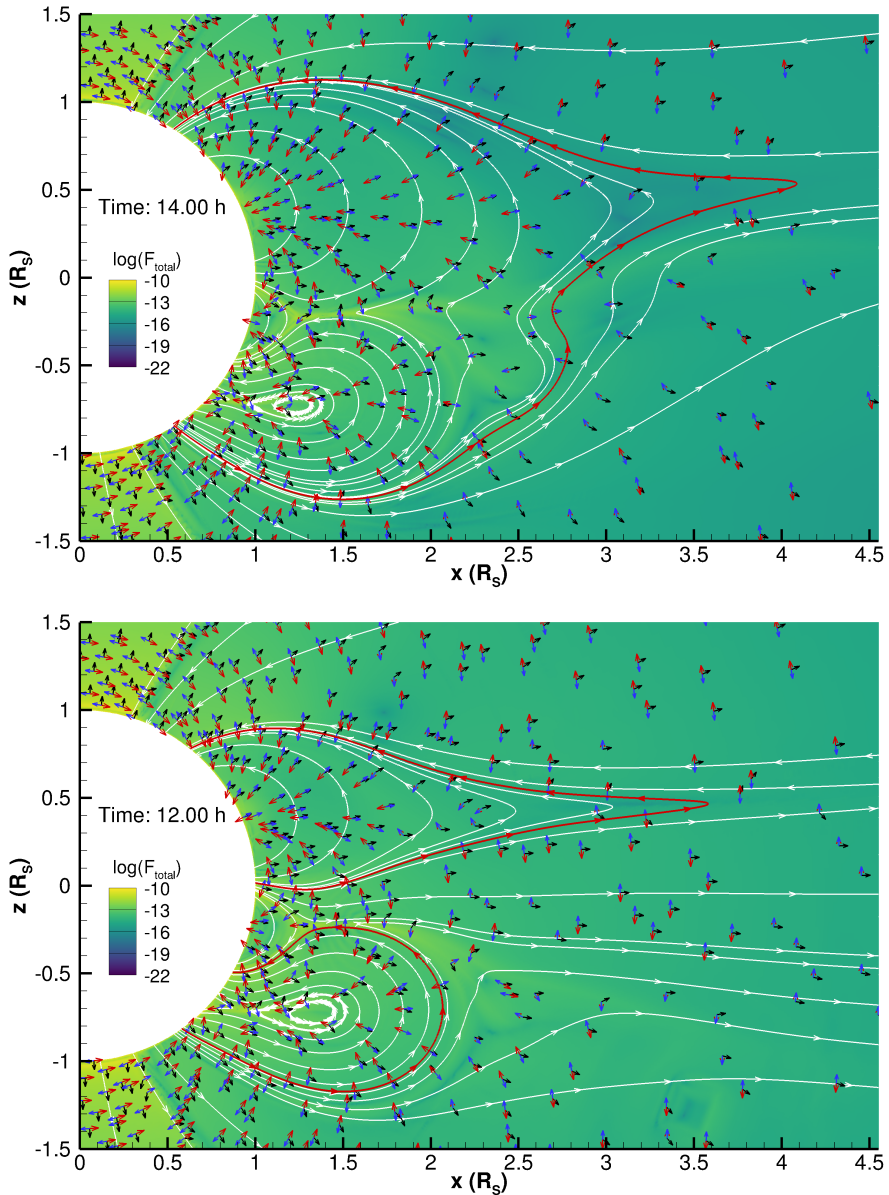


Figure 5.4: Simulation snapshots of the total force (color scale) during the single eruption in the slow-wind (top panel) and faster-wind case (bottom panel). The white and red lines represent selected magnetic field lines. The vectors indicate the following forces: \mathbf{T}_B (red), $-\nabla P_B$ (blue), and $-\nabla P_P$ (black). The snapshots were taken at 14 h (top) and 12 h (bottom) from the start of shearing, such that the front of both CMEs is at $\approx 2 R_\odot$.

5.5 by the high plasma β regions and the anti-parallel magnetic field lines. The two flux ropes moving in opposite directions stretch the current sheet trailing CME1 and create a region in which the total force vectors point in opposite directions at each end of the current sheet.

Figure 5.6 shows how the simulation evolved 18 h after the shearing commences. The $-\nabla P_B$ blue vectors shown in Fig. 5.6 indicate compression of the sides of the current sheet, creating a flux rope highlighted by the green magnetic field lines, which is seen more clearly in the expanded view. Since the height at which the reconnection sets in to form this structure is $\approx 1.4 R_\odot$, high enough to present no clear low-coronal signatures (Robbrecht et al. 2009b), we suggest that this is a ‘stealth’ ejecta. This blob-like ejecta follows the total force vectors and erupts along a similar path as CME1.

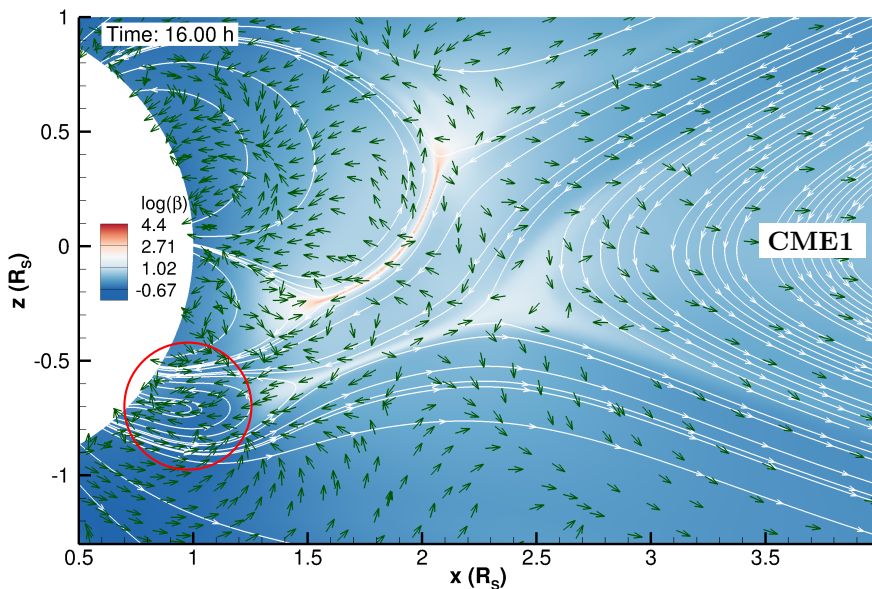


Figure 5.5: Simulation snapshot of the first erupting CME and its trailing current sheet, taken 16 h after the start of shearing. The color scale depicts plasma β values, the white lines are selected magnetic field lines, and the green vectors show the direction of the total force. The red circle highlights the second flux rope, formed from the shearing motions, that falls back to the Sun.

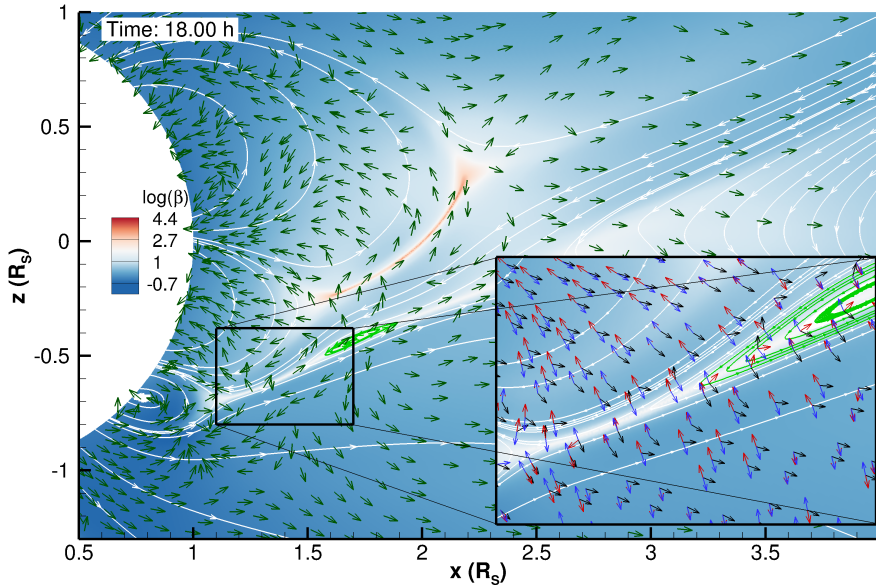


Figure 5.6: Same as Fig. 5.5, but for a larger field of view, taken 18 h after the start of shearing. The green field lines represent the stealth ejecta formed in the current sheet trailing CME1. Bottom right panel: Enlarged view of the black rectangle showing the current sheet in which the stealth ejecta forms; the color scale depicts plasma β , and the vectors are \mathbf{T}_B (red), $-\nabla P_B$ (blue), and $-\nabla P_P$ (black).

5.3.3 Formation of plasma blobs

In this subsection we focus on another type of structure, plasma blobs. They are formed only in the slow solar wind cases by magnetic reconnection in the equatorial current sheet as it rebuilds in the aftermath of the eruptions. For simplicity, the scenario we analyzed is that of the single eruption, but the physical mechanisms and explanations are valid for all three slow-wind simulations.

As discussed in Sec. 5.2.2, all the simulated CMEs experience deflection towards the equatorial plane, but only those ejected into the slow wind magnetically reconnect with the northern arcade during their eruption phase, becoming structurally coupled to it, as in the top panel of Fig. 5.4. In this process, the CMEs compress the arcade, which after the passage of the CME slowly returns to its original size.

Here we address how the blobs are formed and why they are created. After the CME has erupted into the equatorial current sheet, the cusp of the northern arcade elongates (top panel of Fig. 5.7) and pinches off at an X-point indicated in the bottom panel of Fig. 5.7, creating the plasma blob depicted by the red field lines. This mechanism resembles the one described by Wang et al. (2000) in their Fig. 8b. In their study, they called such a structure a detached ‘plasmoid’, although they deemed this scenario unlikely in a realistic 3D geometry in which

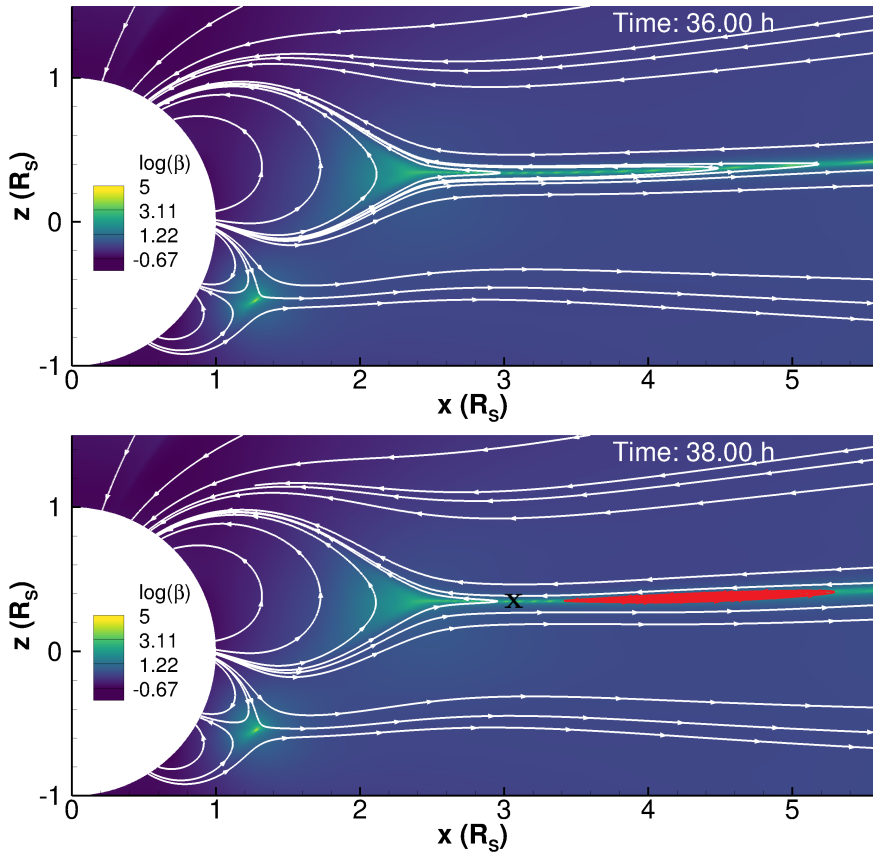


Figure 5.7: Snapshots of the plasma β from the slow wind - single eruption simulations taken at 36 h (top panel) and at 38 h (bottom panel), depicting the formation of a plasma blob (red field lines) from the northern streamer cusp. The X-point created between the blob and the streamer cusp is indicated (X) in the bottom panel.

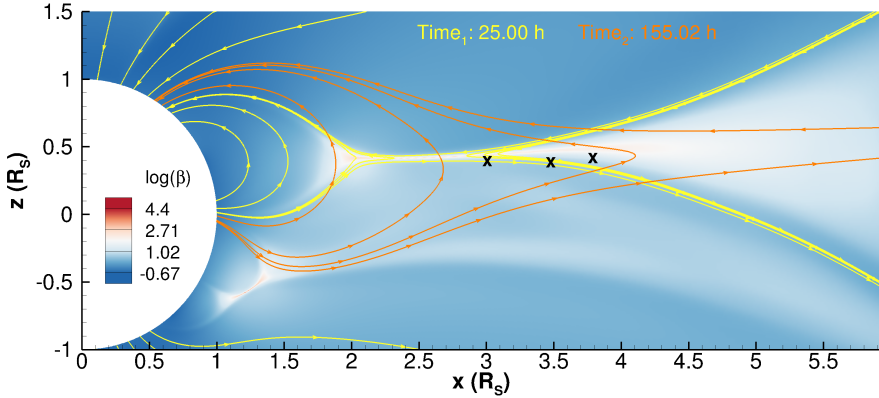


Figure 5.8: Snapshot of the plasma β (color scale) and magnetic field lines (yellow) from the slow wind - single eruption simulation taken 25 h from the start of shearing, showing the compressed arcade and the trailing part of the CME on the right side. The orange field lines show the magnetic configuration of the northern arcade from the same simulation, after it has relaxed to its original state, 155 h from the start of shearing. The X-points form between the streamer cusp and blobs and evolve further from the Sun as time increases.

a helical flux rope still attached to the Sun would form instead. However, this scenario is not entirely impossible since the coronal structure in which they placed this mechanism was a stable streamer, in contrast to our simulations, where the blobs form from the cusp of an expanding streamer. In order to illustrate this dynamic property, in Fig. 5.8 we superpose the orange magnetic field lines of the relaxed streamer 155 h from the start of shearing on those of the perturbed state (yellow field lines) only 25 h from the start of shearing, where the CME is still visible in the right panel of the figure. The recovery of the small compressed arcade to its original size can be tracked via the location of the X-points created between the blobs and the streamer cusp, indicated in Fig. 5.8. The rising streamer cusp is renewed every time a blob detaches. As the arcade evolves, the X-points are placed at higher distances from the Sun, indicating the expansion of the magnetic structure. It would be interesting to investigate this scenario further in a 3D simulation without the limitations of the 2.5D geometry used here.

We calculated the forces in the region trailing the CME, where these blobs are formed. In particular, we extracted their values along a latitudinal arc at constant distance from the Sun in order to study the forces in the direction perpendicular to the current sheet that led to magnetic reconnection. For the slow-wind simulation, we took these values just before the formation of two of

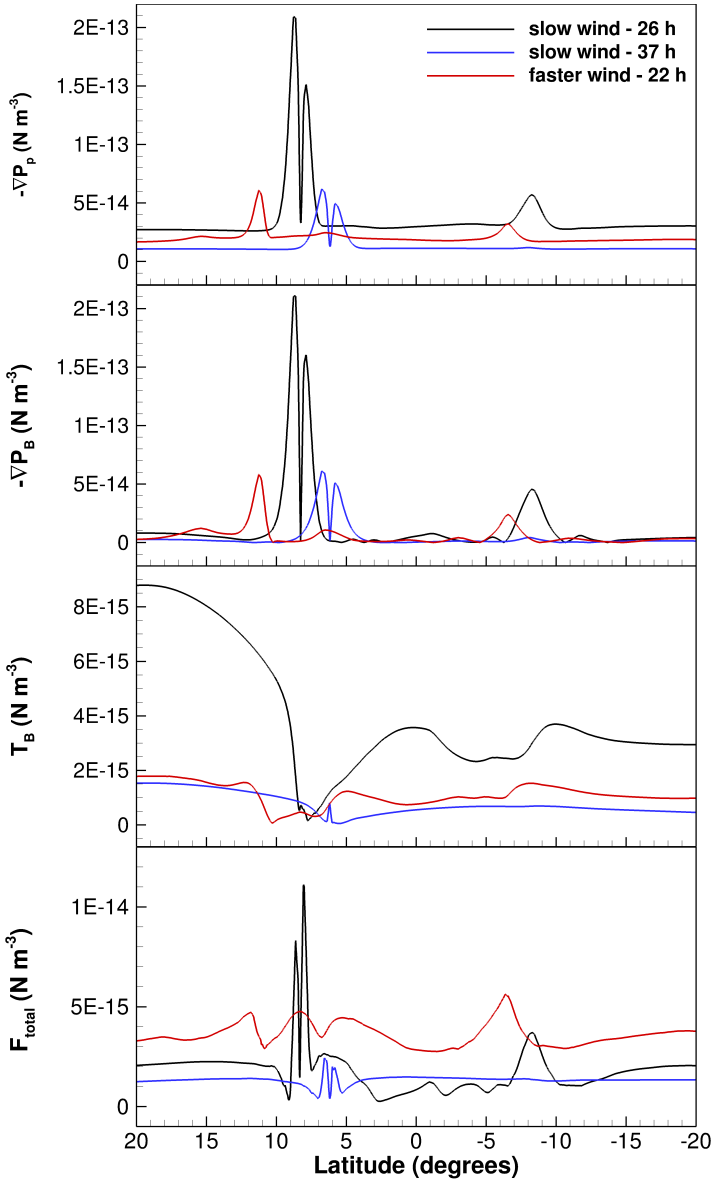


Figure 5.9: Forces extracted from a latitudinal cut through the current sheet occurring in the aftermath of eruptions at different heights and simulation times. The slices were taken through the slow wind - single eruption simulation at $2.62 R_\odot$ and 26 h from the start of shearing (black line), and at $3.2 R_\odot$ and 37 h (blue line), and through the faster wind - single eruption at $3.3 R_\odot$, 22 h from the start of shearing (red line).

the plasma blobs, in the vicinity of the reconnection site (close to the X-points indicated in Fig. 5.8) 26 h and 37 h after the start of shearing. Since the CMEs in the faster-wind cases did not present such blobs, we also took a cut through the current sheet trailing the single eruption in this latter scenario, in order to understand the differences that lead to the formation of the small flux ropes. The values of the extracted forces are plotted as a function of latitude in Fig. 5.9. The first noticeable distinction is between the profiles of $-\nabla P_P$ and $-\nabla P_B$ for the two background solar winds. The current sheet in the aftermath of the single eruption in the slow wind is associated with double-peaked structures in both these parameters, as compared to the single peaks associated with the current sheet in the faster-wind case. Even though the amplitudes of these peaks decrease in time from the formation of one blob to the other (back line versus blue line) due to the strong disturbances being carried away from the Sun, the double-peaked profile is preserved. We interpret the double peaks as the cause of the formation of the blobs, since the current sheet is squeezed from the sides and magnetic reconnection is induced by the perpendicularly-oriented $-\nabla P_B$ vectors, which are shown in the bottom panel of Fig. 5.10 (inside the yellow rectangle). Figure 5.10 shows $\log(-\nabla P_B)$ values in the current sheet formed in the aftermath of the CME in the faster (top panel) and slow (bottom panel) solar wind cases. The squeezing of the current sheet does not occur in the faster-wind case because the plasma and magnetic pressure gradients are strong only on the northern side of the current sheet, preventing the magnetic field from pinching. This is visualized in the yellow rectangle in the top panel of Fig. 5.10. The third panel of Fig. 5.9 depicts the magnetic tension. This is almost two orders of magnitude smaller than the other forces, and therefore the Lorentz force is mainly comprised of the magnetic pressure gradient. This is not surprising since the current sheet contains magnetic field lines that are nearly parallel to each other, so the lack of curvature leads to extremely low values of \mathbf{T}_B .

Other plasma blobs are present much later in the same current sheet as well, after the eruption of the CME. They are not from the streamer cusp, and they occur at larger distances from the Sun. In the slow wind - double eruption case, the second CME catches up with the first CME and compresses it, creating a current sheet between the two flux ropes where plasma blobs also form. All these features are driven by interesting mechanisms, but their analysis is not addressed in this thesis.

5.3.4 Propagation and interaction of CMEs

In this final subsection, we analyze the interaction between CMEs, and the interaction with the background solar wind. We discuss the first topic in the

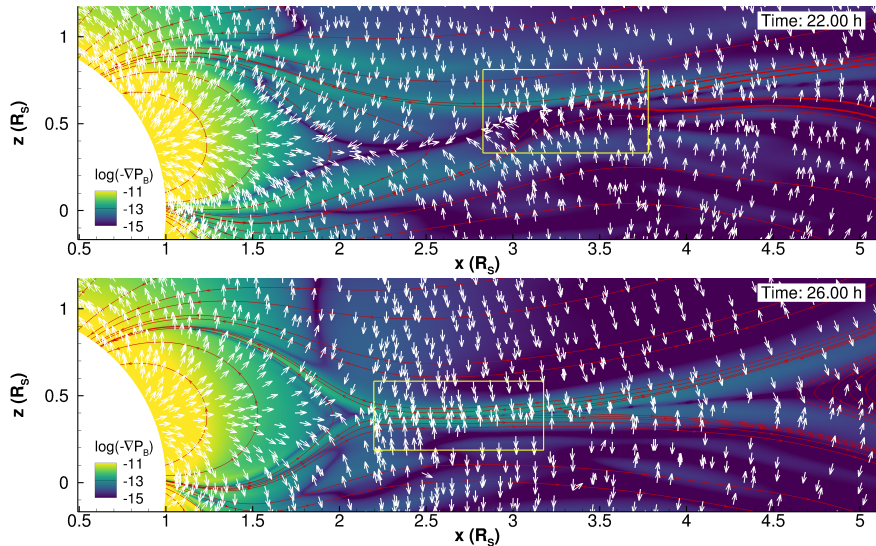


Figure 5.10: Snapshots of the magnetic pressure gradient (color scale) depicting the formation of current sheets in the aftermath of CMEs in the single-eruption case inserted into the faster background wind (top panel) and slow wind (bottom panel). The white vectors represent $-\nabla P_B$, and the red lines are selected magnetic field lines. The yellow rectangles are regions of interest, as discussed in the text.

context of the slow wind - double eruption simulation because it contains two CMEs triggered by the imposed shearing motions, and they are large enough to influence each other during their propagation to 1 AU. We calculated the forces in the entire computational domain, and then extracted the values along the equator, which is shown in the top panel of Fig. 5.11. The time of the simulation chosen to perform these steps is 55 h after the start of shearing, when the front of the first CME is at approximately $85 R_\odot$. At this distance from the Sun, the second CME has not yet merged with the first, but it is close enough to influence it, as is shown in the bottom panel of Fig. 5.11.

Regions indicated by numbers 1 and 1' depict the background solar wind in front of and behind the eruptions, where the plasma β is much higher than 1 and $-\nabla P_P$ (black line) makes the dominant contribution to the total force (green line). The peak indicated by number 2 is present only in $-\nabla P_P$ and is created by the solar wind plasma accumulation in front of the CME, as it compresses the material ahead of it while propagating through interplanetary space. The first flux rope (number 3) is delimited by two peaks in $-\nabla P_P$ and $-\nabla P_B$ and

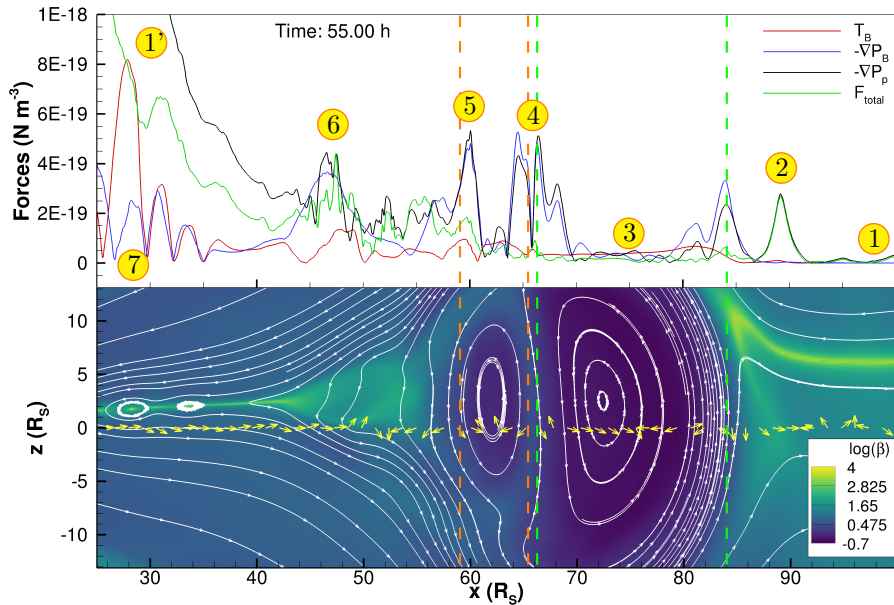


Figure 5.11: Snapshots of the evolution of the CMEs in the slow wind - double eruption case, taken 55 h after the start of shearing. Top: Forces extracted from an equatorial 1D slice through this configuration. Bottom: Snapshot of the plasma β (colour scale) and selected magnetic field lines. The 1D slice in the top panel was extracted from this same configuration. The numbers indicate the following features, described more extensively in the text: 1 and 1' - solar wind in front of or trailing the CMEs; 2 - plasma compression front; 3 - core of CME1; 4 - compression zone between the two CMEs; 5 - end of second flux rope; 6 - tail of the CMEs; and 7 - plasma blobs. The dashed green and orange lines delimit the two flux ropes. The yellow vectors represent the total force along the 1D slice.

by the dashed green lines, while inside, all the forces plateau at low values. The yellow vectors show that the total force is directed oppositely between the front and rear of the CME interior, flattening the flux rope and creating the well-known ‘pancake’ effect. This is caused by the radial expansion of the solar wind and occurs regardless of the CME-CME interaction. We just mention here that this realistic effect is also present in our simulations, but we do not further expand on the topic since it has been extensively studied observationally and by numerical means by many authors (e.g. Riley & Crooker 2004; Savani et al. 2011; Isavnin 2016). The vectors do not change orientation exactly at the center of the flux rope, indicating that the center will be carried towards the front part

of the CME. Number 4 depicts the zone of compression between the two CMEs, and also the beginning of the second flux rope, delimited by the dashed orange lines. The behavior of the total force vectors within the second CME is very similar to that of the first CME, pushing the front and rear towards the center and producing the same pancaking effect. As the two flux ropes approach each other, they magnetically reconnect, and the second flux rope disappears as it fully merges with the first during their propagation. This second process is able to take place because the two flux ropes share the same magnetic orientation, as they originate from the same coronal arcade. This leads to the oppositely directed fields at the trailing edge of the first flux rope and the leading edge of the second flux rope. The overlying magnetic field lines that surround both CMEs are evidence that this merging has already started to take place. The region between the end of the second flux rope (number 5) and the peak at number 6 represents the tail area of the CMEs, where almost all the forces are turbulent and have high values. The magnetic tension does not contribute greatly to the propagation of the eruptions, as compared to the initiation and eruption phases. However, \mathbf{T}_B and $-\nabla P_B$ do show major fluctuations in the region trailing the CMEs. The peaks in the area depicted by number 7 are the cause of magnetic null points either at the center of or between plasma blobs created in the aftermath of the eruptions from the reconfiguration of the current sheet. We note that the 1D slice does not pass directly through the center of the flux ropes or plasma blobs, since they propagate into the equatorial current sheet, which is deflected northward due to the magnetic configuration at the inner boundary.

We now discuss the interaction of the CMEs with the background wind in the cases of the single eruptions inserted into both background solar winds. Because these eruptions are the simplest cases, we can therefore assess the influence of the solar wind alone, excluding effects of CME interaction. The shearing speed applied to obtain these single eruptions is approximately the same for both solar winds, as is their morphology and eruption mechanism. The difference, which we cannot eliminate from the contributing factors, is the presence of plasma blobs trailing the CME in the slow-wind case.

For this part, we performed a similar analysis as in the previously discussed double eruption scenario, but focused on the differences occurring over time due to the effects during propagation. Therefore, we analyze the forces along equatorial cross-sections through the CMEs when the fronts of their flux ropes are at $\approx 35 R_\odot$ (≈ 0.163 AU) and 1 AU. Figure 5.12 shows an overview of the magnetic field configuration of the eruptions at the moment of computation of the forces. The times of the snapshots differ between the two background solar winds because of the higher propagation speed of the CME in the faster-wind case. Figure 5.13 depicts $-\nabla P_P$ values taken at the equator. The top panel

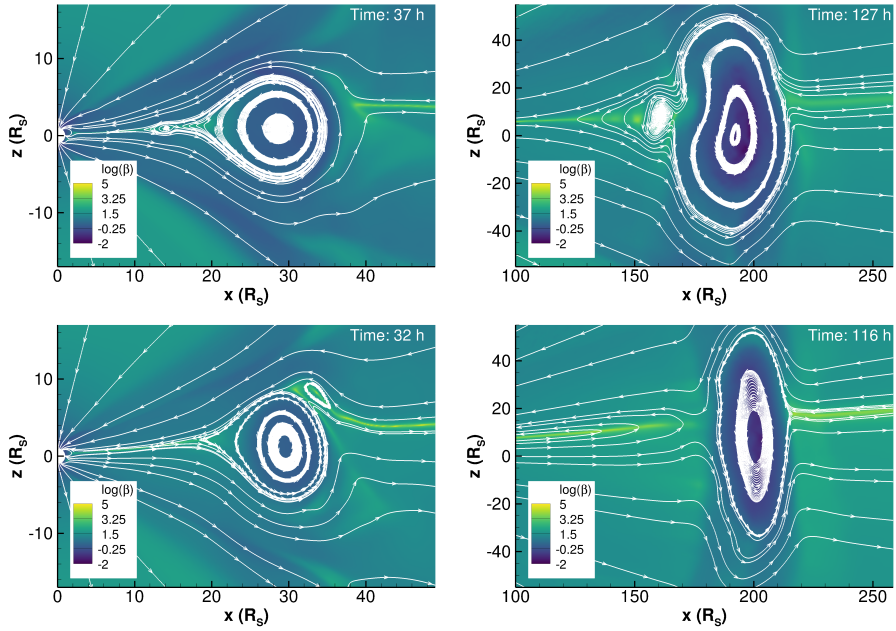


Figure 5.12: Snapshots of the CMEs in the single eruption cases, propagating in the slow (top row) and faster (bottom row) background solar winds. The first column shows the CMEs when the front of the flux ropes are at $\approx 35 R_{\odot}$, and the second column when they reach 1 AU. Each snapshot was taken at the times indicated in the respective panels. The color scale depicts plasma β values, and the white lines represent selected magnetic field lines.

shows that close to the Sun, the eruptions do not differ greatly between the two background winds. The exceptions are the higher values in the faster-wind case below $20 R_{\odot}$ (as expected due to the overall higher density), and the stronger peak in the slow-wind case indicating the trailing edge of the flux rope. To identify the forces in this region more easily, the main flux rope is approximately delineated by the dashed gray and pink lines in the cases of slow and faster solar wind, respectively. During propagation to 1 AU, some interesting differences form in the plasma pressure gradient, and the background level begins to even out between the two cases due to the large distances and density decrease. The plasma accumulation in front of the CME in each simulation creates a peak that is present only in $-\nabla P_P$. We investigated whether this structure is a shock by calculating the MHD wave velocities of the background solar winds. These velocities are shown in Fig. 5.14. The Alfvén and sonic speeds are not shown

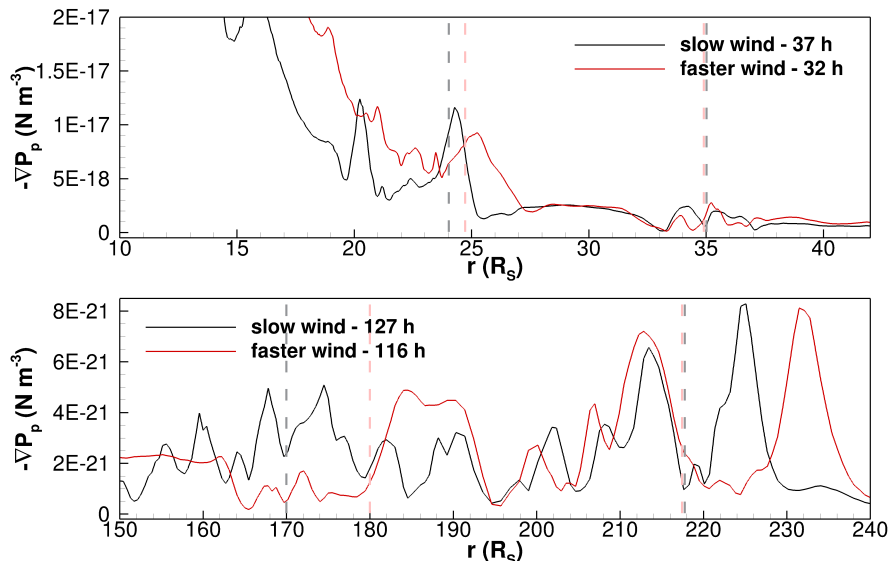


Figure 5.13: Plasma pressure gradient values extracted from the equatorial cross-section through the single eruptions depicted in Fig. 5.12, propagating in the slow background solar wind (black line) and in the faster wind (red line). The panels show results for two distance ranges that include the main flux rope, which is approximately delineated by the dashed gray and pink lines in the slow and faster solar wind, respectively.

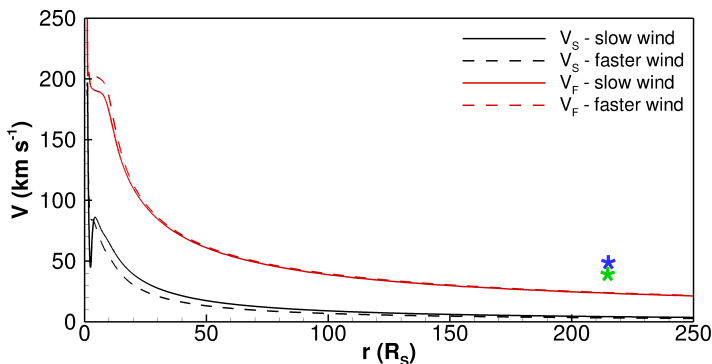


Figure 5.14: MHD wave velocities corresponding to slow (red lines) and fast (black lines) magnetoacoustic waves for the slow (solid lines) and faster (dashed lines) background solar winds. The velocity of the front of the CME at 1AU with respect to the solar wind is indicated by the blue asterisk in the case of the slow background wind and by the green asterisk for the faster wind.

because they become almost identical to the slow and fast magnetoacoustic velocities at the large distances that we are interested in. We then calculated the speed of the structure from the average of four snapshots with the peak around 1 AU, and subtracted the speed of the background wind for each case. The two asterisks in Fig. 5.14 indicate this difference in speed at 1 AU for the two single eruption cases. Interestingly, they are both higher than the slow and fast magnetoacoustic velocities of their respective background winds. This implies that during propagation of the CMEs to Earth, the leading edge of the plasma accumulation became a fast shock, not necessarily because the plasma significantly accelerated, but because of the decrease in the wave velocities. For a quantitative assessment, the speeds of the shock and the respective background wind are 387 km s^{-1} and 339 km s^{-1} (slow wind), and 423 km s^{-1} and 384 km s^{-1} (faster wind). This agrees with observations of slow CMEs producing shocks reported by Liu et al. (2016) and Lugaz et al. (2017a). The plasma pressure gradient in Fig. 5.13 inside the flux rope is similar for both cases, between $\approx 220 R_{\odot}$ and $195 R_{\odot}$. However, the CME in the faster-wind case is more compressed and is followed by a depression in $-\nabla P_P$ and a reconfiguration of the equatorial current sheet below $160 R_{\odot}$. The CME in the slow-wind case is larger and not as well structured in the tail because of the trailing plasma blobs.

The magnetic pressure gradient shown in Fig. 5.15 shows two peaks at the front of the flux rope in both cases. This contrasts with the CME structure simulated and analyzed by Hostenaux et al. (2021), which had only one peak at about the same distance from the Sun (at $\approx 35 R_{\odot}$). The first increase seen in our simulations can be attributed to the overlying magnetic field at the eruption time and to the streamer that is stripped away along with the CME. This would not be present in the case of Hostenaux et al. (2021), who just injected a plasma blob into the solar wind and did not model the eruption. This suggests that different triggering mechanisms can affect the structure of CMEs, including during propagation, and therefore should be taken into consideration when interpreting CME structure. The sunward edge of the flux rope is clearly distinguishable in $-\nabla P_B$ in the faster-wind case both close to the Sun (located at $25 R_{\odot}$) and also at $180 R_{\odot} - 194 R_{\odot}$. On the other hand, the trailing part of the CME in the slow wind is more complex: the flux rope and the trailing region ending at $24 R_{\odot}$ and $20 R_{\odot}$, respectively, are followed by several peaks indicating the plasma blobs. During propagation to Earth, these trailing peaks combine into only two peaks as the structure becomes more similar to that of the faster-wind case.

The magnetic tension shown in Fig. 5.16 makes the smallest contribution to the total force, except in the region of the trailing plasma blobs when close to the Sun. At 1 AU, the blobs merge and create a plateau in \mathbf{T}_B in the aftermath

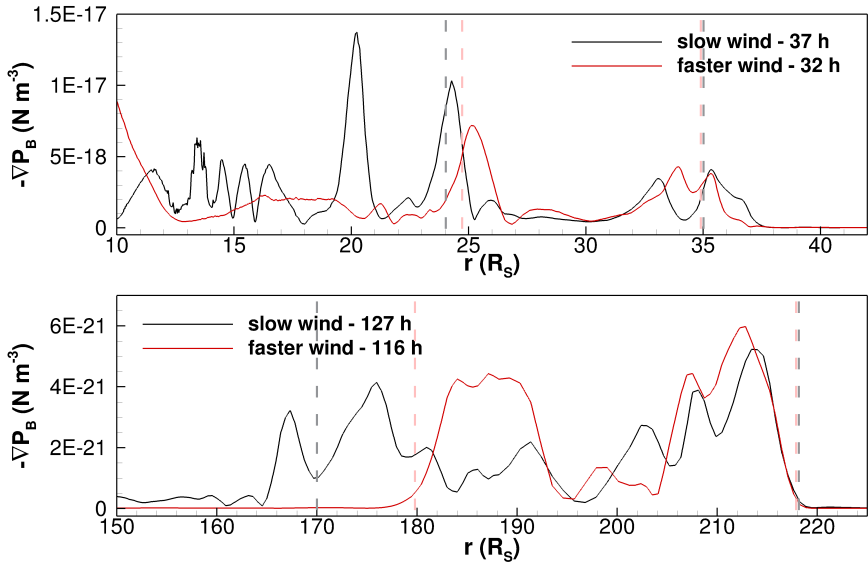


Figure 5.15: Same as Fig. 5.13, but depicting magnetic pressure gradient values.

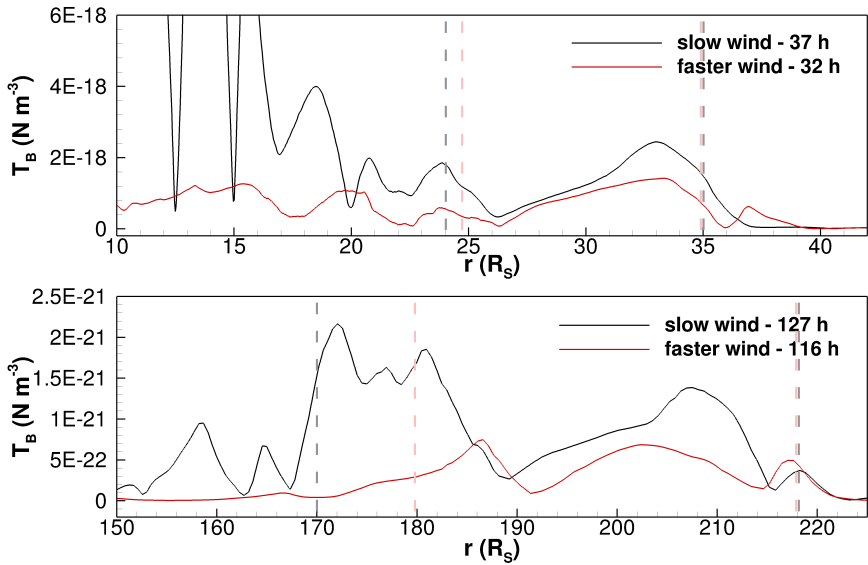


Figure 5.16: Same as Fig. 5.13, but depicting magnetic tension values.

of the CME. An interesting aspect is that \mathbf{T}_B is consistently higher in the slow-wind case than in the faster-wind case throughout the propagation. This also slowed the eruption close to the Sun in the slow-wind case, as previously discussed in Subsection 5.3.1.

5.4 Summary

This Chapter completes the analysis discussed in Chapters 3 and 4, involving numerical MHD simulations of CMEs triggered by boundary shearing motions. We studied here the CMEs generated by five different erupting scenarios by calculating the forces governing their dynamics. Three of the eruptions were propagated into a slow background solar wind, and two into a faster solar wind. We addressed four aspects of the eruptions that mostly arose from the differences in background wind and consequently, in the initial magnetic configuration.

Firstly, we traced the cause of the faster eruption of CMEs in the faster solar wind cases (when the same shearing speed was applied as in the slow-wind cases) to the more closed streamer structure in the slow-wind cases. In our simulations, the CMEs erupt from the southernmost arcade and are deflected towards the equatorial plane. In this process, there is significantly more reconnection between the ejected flux ropes and the large northern arcade in the slow-wind scenarios. Therefore, our conclusion is that in the case of slow CMEs, the adjacent magnetic structures are important because they can decelerate the eruption originating from nearby arcades. This is possible via magnetic reconnection that creates overlying loops and increases the confining downward magnetic tension. This interpretation also accounts for why in the stealth speed case two flux ropes erupt from the shearing velocity, whereas the same shear applied in the slow-wind case results in one CME created by the shearing motions and one from the reconfiguration of the coronal magnetic field.

Secondly, we explained the formation of the stealth ejecta by calculating the forces in the region of the current sheet created in the aftermath of CME1. As CME1 is ejected, the flux rope formed by the imposed shearing motions falls back to the Sun because of the insufficient energy build-up. This process stretches the current sheet and the magnetic pressure gradient pushes the sides of the magnetic field lines, pinching the current sheet. This creates a flux rope (stealth ejecta) that is ejected onto a similar path as CME1.

Thirdly, plasma blobs detaching from the streamer cusp in the aftermath of eruptions are also caused by the different initial magnetic structure. In the slow-wind case, the northern arcade is greatly compressed by the deflected CMEs, and in the process of returning to its original state, it elongates. The

$-\nabla P_B$ forces pressing from both sides of the current sheet then induce magnetic reconnection, which creates the blobs.

Finally, we analyzed the interaction of the two CMEs in the double eruption case and we were able to distinguish the main regions of the two flux ropes. Through the analysis of forces presented, we explained the merging and pancaking of the two flux ropes. Furthermore, we studied the effect of the two background solar winds in the two similar single eruption cases. Surprisingly, even though the CMEs are slow, the plasma accumulated ahead of the CMEs creates a peak in $-\nabla P_P$ that evolves into a fast shock by the time they reach Earth. The double-peak structure of $-\nabla P_B$ in front of the CME could indicate that signatures of the processes triggering CMEs are retained by CMEs as they propagate through the solar wind. This suggests that CME triggering should be taken into consideration when interpreting CME structure from in-situ observations. The magnetic tension ahead of the CME is higher in the slow solar wind cases than in the faster solar wind ones, and it contributes to the initial deceleration of the CME. However, it makes the smallest contribution to the CME dynamics in interplanetary space.

This research concludes the study presented in Chapters 3 and 4, which was initiated by an observed MCME event. In Chapters 3 and 4, we performed and analyzed MHD numerical simulations consistent with the observations, and explored the influence of different shearing motions on the dynamics of the resulting eruptions. We then propagated these eruptions through two different background solar winds, tracked their evolution via in-situ signatures, and computed their geoeffectiveness. In the current Chapter, we explained the formation and dynamics of some particular features present in the simulations by computing the three main forces ($-\nabla P_P$, $-\nabla P_B$ and \mathbf{T}_B). We also assessed their contributions to the overall kinematics of the CMEs. This technique of force vector decomposition has -to our knowledge- been applied extensively to 2.5D MHD simulations for the first time here. This study demonstrates that this technique is a valuable tool for research on CME eruption and propagation through the solar wind.

Chapter 6

Conclusions

*“Home is behind, the world ahead,
And there are many paths to tread
Through shadows to the edge of night,
Until the stars are all alight.”
– Pippin, Lord of the Rings*

Our study aimed to combine observational and numerical methods to investigate stealth CMEs and determine the processes that trigger them, their geomagnetic effects and how they differ from more typical solar eruptions, allowing us to improve the forecasts of their geoeffectiveness. Another important aspect is the interaction of the CMEs with different background solar winds or with other CMEs that can also affect their propagation to Earth. We studied these aspects numerically and by analyzing the forces that contribute to their dynamics.

The basis of this thesis consisted of 2.5D magnetohydrodynamics numerical simulations using the code MPI-AMRVAC. The initial configuration was chosen to be a triple arcade magnetic structure embedded into a bimodal background solar wind, which resembles the magnetic environment prior to a multiple CME event occurring on 21-22 Sept 2009. In order to obtain CMEs, the magnetic stress in the corona was increased by applying shearing motions along the central line of the southernmost arcade of the triple arcade structure. This was achieved by imposing an additional azimuthal component of the speed at the inner boundary for 16 h. In Chapter 3 we made a parameter study on this shearing speed and its effects on the dynamics and evolution of the subsequent CMEs, and obtained three different scenarios with a 1% change in the maximum amplitude:

- Two CMEs resulting from shearing motions ($|v_\phi| = 37.4 \text{ km s}^{-1}$), double eruption case;
- One CME resulting from shearing motions and a failed eruption ($|v_\phi| = 37.2 \text{ km s}^{-1}$);
- One CME resulting from shearing motions and a stealth ejecta arising from coronal magnetic field reconfiguration ($|v_\phi| = 37 \text{ km s}^{-1}$), eruption + stealth case.

We analyzed the dynamics of the simulations and compared them with two observed CMEs, obtaining a good correlation for the double eruption case, even though the secondary observed CME did not present obvious low-coronal signatures. Therefore, the so-called **‘stealth’ CME might still be triggered by the shearing motions at the photosphere, even though we cannot locate any clear signatures**, possibly due to the insufficient resolution or capabilities of the current instrumentation. We also analyzed the observed events to obtain the real propagation directions and speed, using the GCS model. The calculated deprojected speeds were $257 \pm 69 \text{ km s}^{-1}$ for the first CME, and $349 \pm 70 \text{ km s}^{-1}$ for the second CME. We further investigated the evolution of the radial Poynting flux close to the inner boundary, to acquire a global perspective of the electromagnetic energy introduced into the computational domain. The steps in dynamical evolution of the simulated CMEs could be correlated with certain features (maximum, minimum or fluctuations) in the Poynting flux profile, highlighting the surprising similarities between the stealth and failed eruptions, and the sensitive coronal response to stress factors. Another interesting point is that in all the discussed simulations, **plasma blobs arise in the current sheet formed in the aftermath of the eruptions**, which have also been documented observationally.

In Chapter 4, we continued to investigate the previously simulated eruptions and the trailing plasma blobs. We also analyzed the effect of a different background solar wind on the CMEs by increasing the speed of the wind through the temperature. Since the current numerical scheme uses ‘conserved’ variables (such as momentum), the change in temperature affected not only the speed, but also increased the density. These modifications also had an effect onto the initial magnetic configuration, by opening the arcades and separating the two in the south from the major one in the northern hemisphere. It is interesting to note from this new initial condition that **the magnetic configuration changed, even though we did not vary the magnetic field itself**. Our observational interpretation is that **creating a magnetic coronal extrapolation just from a photospheric magnetogram is not enough to give a unique or correct solution**. This inaccuracy has also been noticed when comparing modeled magnetic field using PFSS extrapolations with the observed plasma trapped in magnetic loops.

Once the relaxed state had been achieved with this newly imposed faster solar wind, we again applied shearing motions on the southernmost arcade. The same amplitude that resulted in a stealth CME following a first eruption ('stealth speed') now created two CMEs. Previously in the slow wind case, in order to analyze the effects of the following eruptions on the first CME, we also performed a simulation with a single flux rope formation. In total, we further analyzed five simulations:

- single eruption in the faster wind;
- 'stealth speed' in the faster wind;
- single eruption in the slow wind;
- stealth CME in the slow wind;
- double eruption in the slow wind.

By applying the 'stealth speed' onto the faster solar wind configuration, the first CME presented a larger erupting velocity, probably due to the more open southern magnetic structure. Also, the second CME did not occur anymore from the reconfiguration of the coronal magnetic field, but rather from the shearing motions applied, as did the first eruption. The single eruption simulation, though, kept the same morphology as in the slow wind case and created a single flux rope from the imposed shear. An interesting observation is the lack of plasma blobs in the aftermath of eruptions, making them dependent on the initial magnetic configuration, rather than on the amplitude of the applied shearing speed.

We compared the signatures of all the CMEs from the five aforementioned simulations and noticed that the **negative B_z component of the magnetic field is highly influenced when the CME is ejected into the faster solar wind**. Its absolute value is decreased, possibly due to the change in the initial configuration, and this property is seen throughout the propagation to Earth. The arrival time at 1AU is also influenced by the background solar wind speed and is shifted by approximately half a day earlier in the faster wind case. We then compared two of the slow wind scenarios (double eruption and eruption + stealth) with the previously mentioned observed MCME event from 21-22 Sept 2009. The two CMEs propagated in the direction of Mercury and Earth, which were separated by only a few degrees. We investigated several parameters from the two simulations and in situ data taken by MESSENGER (orbiting around Mercury) and by ACE and WIND (at L1, in front of Earth) spacecraft. Surprisingly, **both scenarios fit well the measured data**, illustrating that it may be difficult to identify signatures in in situ observations that are able to distinguish between different CME triggering mechanisms.

Afterwards, we studied the geoeffectiveness of the simulated interplanetary CMEs, by using a model for the Dst index, which is a function of the speed, B_z component and the dynamic pressure measured in front of Earth. With it, we computed the hypothetical induced geoeffectiveness from simulated parameters. We observed that the least geoeffective ICME is also the one with the smallest absolute B_z component recorded at Earth, which is the eruption inserted into the faster solar wind and created by applying the same shearing speed that resulted in a stealth eruption in the slow wind case. Due to the 2.5D geometry of the simulations, the ICMEs maintain the same magnetic orientation as the solar arcade from which they erupted, and in this case, they arrive at Earth with the positive B_z component in the front. Therefore, the trailing flux ropes decrease the total magnetic flux in the negative B_z part, decreasing the geoeffectiveness.

This led to the computation of the Dst from values of B_z if the initial magnetic configuration was reversed, making the ICMEs arrive with a negative B_z component in the front. We performed this test in order to investigate how much the trailing flux ropes affected the magnetic field in the tail of the CME. In this configuration, the now trailing positive B_z has reconnected with the following flux ropes, leaving the negative B_z frontal part unaffected. **This reversal increased the geoeffectiveness of all the simulated ICMEs**, and shifted the minimum of Dst earlier with probably the time it required the negative part of the magnetic cloud in the slow wind case to reach the investigated point at 1AU. Furthermore, a Dst enhancement of 20 nT is observed for the double eruption case, increasing the geomagnetic impact. Overall, this indicates that a secondary eruption can increase, but also decrease the geoeffectiveness of a prior CME, as long as they exhibit magnetic interaction during their propagation.

In order to understand some of the previously noticed interesting processes in our simulations, we analyzed in Chapter 5 the governing forces. **We calculated the magnetic tension, magnetic pressure gradient, plasma pressure gradient and total force, and tracked their evolution from the formation, onto the eruption, and throughout the propagation of the CMEs.** The topics examined were the following:

- The faster eruption of CMEs in the faster solar wind cases, when the same shearing speed is applied as in the slow wind cases;
- The formation of the stealth ejecta;
- The occurrence of plasma blobs in the aftermath of eruptions, only in the slow wind cases;
- The propagation of CMEs and their interaction with the background wind and with other CMEs.

We used the forces in vectorial form, and explained the stealth and blobs formation by the action of the magnetic pressure gradient onto the different current sheets formed after eruptions. The magnetic pressure gradient pinches the sides of the current sheets and creates the respective flux ropes. **The faster eruption of the first CME in the faster solar wind case was attributed to the less confining magnetic tension in this background wind**, which allowed the CME to erupt without being decelerated by overlying magnetic field lines. This effect of deceleration is observed in the slow wind cases. We also presented the interaction of the CMEs in the double eruption case by taking cuts along the equator and through the forces. We identified the beginning and end of each of the two flux ropes via peaks in plasma and magnetic pressure gradients. The plasma blobs could also be distinguished in the tail of the CMEs in the variation of the magnetic tension and magnetic pressure gradient. During the propagation to Earth, we also showed that the **plasma pile-up in front of the eruptions**, seen as a peak in the plasma pressure gradient, **becomes a fast shock in both solar wind cases. The merging of the two CMEs could also be visualized in the evolution of the magnetic tension**, which develops into a flat plateau in the region of the magnetically reconnecting flux ropes.

To summarize, we simulated the eruption of different CMEs by means of shearing motions in two separate background solar winds. A first result was the extremely sensitive coronal response to very small differences in shearing motions, which we concluded from **obtaining three different eruption scenarios with a 1% change of shearing speed**. The change in background wind modified the initial magnetic configuration, leading to different eruption dynamics, as well as an absence of plasma blobs. This emphasizes the important role of the coronal magnetic field (as compared to just the photospheric conditions) on the initiation and eruption of CMEs. This is important, for instance, for magnetic extrapolations that try to recreate the coronal configuration using data solely from magnetograms. Our opinion is that coronal magnetic fields need to be better constrained with coronal plasma information as well, in order to provide an accurate extrapolation. This conclusion resulted from the clear effects of temperature and density onto the magnetic structure, which can lead to entirely different eruptions, making their forecast difficult. Such coronal changes also influence the aspect of streamers that determine the structure of the solar wind, thus conditioning the eruptions also during their propagation in interplanetary space, and making their geoeffectiveness prediction inaccurate. Therefore, **we need also coronal constraints for accurate CME modeling**.

In order to make the simulations more realistic, we compared two of the scenarios in which the secondary eruption was either a stealth ejecta or a flux rope created by shearing motions, with an event observed in situ. A good correlation between

the simulation results and in situ observations was found in both cases: it was almost impossible to distinguish between the two cases due to the interactions that occur during their journey in the interplanetary space. All the simulated CMEs were propagated to Earth, where their geoeffectiveness was also analyzed. The surprising outcome of this computation was the **lowered geoeffectiveness of the double eruption case** as compared to single eruptions. This reduction was induced by magnetic reconnections between the flux ropes during their propagation to Earth. Thus, **consecutive CMEs can also have reduced to no geomagnetic impact on Earth**, given the right erupting conditions. This provides one of the many explanations for the difficulty in predicting the geoeffectiveness of CMEs, since it can induce false alarms in the forecasting system. On the other hand, we also obtained **a two-step geomagnetic ‘storm’ created just from the arrival of one flux rope at Earth** in the stealth speed case (faster wind). This highlights the importance of all the contributing factors and of p_{dyn} in particular to the resulting geomagnetic impact, and not just that of B_z .

As a final step, we provided physical interpretation for some interesting features and aspects present in the simulations, by extensively analyzing the three important forces acting on the flux ropes. We highlight and demonstrate the importance of this method in explaining physical observed phenomena, for a deeper understanding of the processes involved. An interesting implementation of this method would be in a statistical manner, and to evaluate whether these mechanisms occur in all similar eruptions, or if any other processes or trends can be extracted from it. We believe this approach could have many applications and can lead to a deeper understanding of solar eruptions.

This study contributes to our knowledge of CME initiation, propagation and effects on Earth. It would be interesting to investigate these processes in a 3D setup and possibly with a more realistic background solar wind. Since this would be much more computationally demanding, a single case could be simulated and analyzed. This study could also be expanded by a further analysis on how the variations in density, temperature, magnetic field, or other parameters contribute to the resulting eruptions, and to the occurrence of the stealth ejecta and plasma blobs. The background solar wind could also be improved by assuming a non-constant adiabatic index (γ) in the computational domain. Numerically, it would also be interesting to test the influence (if any) on the simulations of different numerical schemes, limiters, CFL numbers, or methods of keeping $\nabla \cdot \mathbf{B} = 0$. However, I leave those tasks to a future PhD student, providing a solid groundwork from which to start :)

Bibliography

- Alfvén, H. 1942, *Nature*, 150, 405
- Alzate, N. & Morgan, H. 2017, *The Astrophysical Journal*, 840, 103
- Anderson, B. J., Acuña, M. H., Lohr, D. A., et al. 2007, *Space Sci. Rev.*, 131, 417
- Antiochos, S. K., DeVore, C. R., & Klimchuk, J. A. 1999, *ApJ*, 510, 485
- Athay, R. G., Gurman, J. B., Shine, R. A., & Henze, W. 1982, *ApJ*, 261, 684
- Athay, R. G., Jones, H. P., & Zirin, H. 1985, *ApJ*, 288, 363
- Bame, S. J., McComas, D. J., Barraclough, B. L., et al. 1992, *A&AS*, 92, 237
- Barnes, C. W. & Sturrock, P. A. 1972, *ApJ*, 174, 659
- Bemporad, A., Zuccarello, F. P., Jacobs, C., Mierla, M., & Poedts, S. 2012, *Sol. Phys.*, 281, 223
- Biermann, L. 1952, in *Liege International Astrophysical Colloquia*, Vol. 4, *Liege International Astrophysical Colloquia*, ed. P. Swings, 251–262
- Biermann, L. 1955, in *Gas Dynamics of Cosmic Clouds*, Vol. 2, 212
- Biesecker, D. A., Myers, D. C., Thompson, B. J., Hammer, D. M., & Vourlidas, A. 2002, *ApJ*, 569, 1009
- Bolduc, L. 2002, *Journal of Atmospheric and Solar-Terrestrial Physics*, 64, 1793
- Bonetti, A., Bridge, H. S., Lazarus, A. J., Rossi, B., & Scherb, F. 1963, *J. Geophys. Res.*, 68, 4017
- Brueckner, G. E., Howard, R. A., Koomen, M. J., et al. 1995, *Sol. Phys.*, 162, 357

- Burlaga, L. F. 1988, *J. Geophys. Res.*, 93, 7217
- Burlaga, L. F., Behannon, K. W., & Klein, L. W. 1987, *J. Geophys. Res.*, 92, 5725
- Burlaga, L. F., Klein, L., Sheeley, N. R., J., et al. 1982, *Geophys. Res. Lett.*, 9, 1317
- Burton, R. K., McPherron, R. L., & Russell, C. T. 1975, *J. Geophys. Res.*, 80, 4204
- Cargill, P. J. 2004, *Sol. Phys.*, 221, 135
- Cargill, P. J., Chen, J., Spicer, D. S., & Zalesak, S. T. 1995, *Geophys. Res. Lett.*, 22, 647
- Cargill, P. J. & Schmidt, J. M. 2002, *Annales Geophysicae*, 20, 879
- Carmichael, H. 1964, in *NASA Special Publication*, Vol. 50, 451
- Chae, J., Wang, H., Qiu, J., Goode, P. R., & Wilhelm, K. 2000, *The Astrophysical Journal*, 533, 535
- Chané, E., Poedts, S., & van der Holst, B. 2008, *A&A*, 492, L29
- Chané, E., Raeder, J., Saur, J., et al. 2015, *Journal of Geophysical Research (Space Physics)*, 120, 8517
- Chané, E., van der Holst, B., Jacobs, C., Poedts, S., & Kimpe, D. 2006, *A&A*, 447, 727
- Chen, C., Liu, Y. D., Wang, R., et al. 2019, *ApJ*, 884, 90
- Chen, J. 1996, *J. Geophys. Res.*, 101, 27499
- Chen, J. & Garren, D. A. 1993, *Geophys. Res. Lett.*, 20, 2319
- Chen, P. F. 2008, *Journal of Astrophysics and Astronomy*, 29, 179
- Chen, P. F. 2011, *Living Reviews in Solar Physics*, 8, 1
- Chen, P. F. & Shibata, K. 2000, *ApJ*, 545, 524
- Clette, F. & Lefèvre, L. 2016, *Sol. Phys.*, 291, 2629
- Cocconi, G., Greisen, K., Morrison, P., Gold, T., & Hayakawa, S. 1958, *Il Nuovo Cimento*, 8, 161
- Cohen, O. 2011, *MNRAS*, 417, 2592

- Cox, A. N. 2002, *Allen's Astrophysical Quantities* (New York: Springer-Verlag)
- Cranmer, S. R. 2009, *Living Reviews in Solar Physics*, 6, 3
- Cranmer, S. R., Gibson, S. E., & Riley, P. 2017, *Space Sci. Rev.*, 212, 1345
- Cranmer, S. R. & Winebarger, A. R. 2019, *ARA&A*, 57, 157
- Cremades, H., Bothmer, V., & Tripathi, D. 2006, *Advances in Space Research*, 38, 461
- Curto, J. J., Araki, T., & Alberca, L. F. 2007, *Earth, Planets, and Space*, 59, i
- Daglis, I. A., Thorne, R. M., Baumjohann, W., & Orsini, S. 1999, *Reviews of Geophysics*, 37, 407
- Dasso, S., Mandrini, C. H., Démoulin, P., & Luoni, M. L. 2006, *A&A*, 455, 349
- Dedner, A., Kemm, F., Kröner, D., et al. 2002, *Journal of Computational Physics*, 175, 645
- Delaboudinière, J. P., Artzner, G. E., Brunaud, J., et al. 1995, *Sol. Phys.*, 162, 291
- Démoulin, P. 2008, *Annales Geophysicae*, 26, 3113
- DeVore, C. R. & Antiochos, S. K. 2000, *The Astrophysical Journal*, 539, 954
- D'Huys, E., Seaton, D. B., Poedts, S., & Berghmans, D. 2014, *ApJ*, 795, 49
- Dissauer, K., Veronig, A. M., Temmer, M., Podladchikova, T., & Vanninathan, K. 2018, *ApJ*, 855, 137
- Dodson, H. W. & Hedeman, E. R. 1964, *Planet. Space Sci.*, 12, 393
- Dodson, H. W., Hedeman, E. R., & Mohler, O. C. 1974, *Reviews of Geophysics and Space Physics*, 12, 329
- Dodson, H. W., Hedeman, E. R., & Mohler, O. C. 1979, in *NOAA Solar-Terrestrial Predictions Proceedings. Volume 1*, ed. R. F. Donnelly, Vol. 1, 385–397
- Dodson-Prince, H. W., Hedeman, E. R., & Mohler, O. C. 1978, *Study of geomagnetic storms and solar in the years of increasing solar activity, cycles 19 and 20, 1955-1957, 1965-1968*, NASA STI/Recon Technical Report N
- Dominique, M., Hochedez, J. F., Schmutz, W., et al. 2013, *Sol. Phys.*, 286, 21
- Dumbović, M., Devos, A., Vršnak, B., et al. 2015, *Sol. Phys.*, 290, 579

- Dungey, J. W. 1961, *Phys. Rev. Lett.*, 6, 47
- Fenrich, F. R. & Luhmann, J. G. 1998, *Geophys. Res. Lett.*, 25, 2999
- Feynman, J. & Martin, S. F. 1995, *J. Geophys. Res.*, 100, 3355
- Forbes, T. G. 2000, *Journal of Geophysical Research: Space Physics*, 105, 23153
- Forbush, S. E. 1937, *Physical Review*, 51, 1108
- Fox, N. J., Velli, M. C., Bale, S. D., et al. 2016, *Space Sci. Rev.*, 204, 7
- Gary, G. A. 2001, *Sol. Phys.*, 203, 71
- Gibson, S. E. 2018, *Living Reviews in Solar Physics*, 15, 7
- Gibson, S. E. & Low, B. C. 1998, *ApJ*, 493, 460
- Goedbloed, H. & Poedts, S. 2004, *Principles of Magnetohydrodynamics* (New York: Cambridge University Press)
- Gonzalez, W. D., Joselyn, J. A., Kamide, Y., et al. 1994, *J. Geophys. Res.*, 99, 5771
- Goossens, M. 2003, *An introduction to plasma astrophysics and magnetohydrodynamics*, Vol. 294 (Dordrecht: Kluwer Academic Publishers)
- Gopalswamy, N., Mäkelä, P., Xie, H., Akiyama, S., & Yashiro, S. 2009, *Journal of Geophysical Research (Space Physics)*, 114, A00A22
- Gopalswamy, N., Xie, H., Akiyama, S., et al. 2015, *ApJ*, 804, L23
- Gopalswamy, N., Yashiro, S., & Akiyama, S. 2007, *Journal of Geophysical Research (Space Physics)*, 112, A06112
- Gosling, J. T. 1990, *Washington DC American Geophysical Union Geophysical Monograph Series*, 58, 343
- Gosling, J. T., Asbridge, J. R., Bame, S. J., et al. 1982, *J. Geophys. Res.*, 87, 239
- Gosling, J. T., Baker, D. N., Bame, S. J., et al. 1987, *J. Geophys. Res.*, 92, 8519
- Gosling, J. T., Hildner, E., MacQueen, R. M., et al. 1976, *Sol. Phys.*, 48, 389
- Gosling, J. T., McComas, D. J., Phillips, J. L., & Bame, S. J. 1991, *J. Geophys. Res.*, 96, 7831
- Gosling, J. T., Pizzo, V., & Bame, S. J. 1973, *J. Geophys. Res.*, 78, 2001

- Groth, C. P. T., De Zeeuw, D. L., Gombosi, T. I., & Powell, K. G. 2000, *J. Geophys. Res.*, 105, 25053
- Hale, G. E. 1931, *ApJ*, 73, 379
- He, W., Liu, Y. D., Hu, H., Wang, R., & Zhao, X. 2018, *ApJ*, 860, 78
- Heppner, J. P., Ness, N. F., Scarce, C. S., & Skillman, T. L. 1963, *J. Geophys. Res.*, 68, 1
- Hewins, I. M., Gibson, S. E., Webb, D. F., et al. 2020, *Sol. Phys.*, 295, 161
- Hewish, A., Scott, P. F., & Wills, D. 1964, *Nature*, 203, 1214
- Higgins, P. 2012, *Schematic of the Solar Dynamo*
- Hirayama, T. 1974, *Sol. Phys.*, 34, 323
- Hirshberg, J., Alksne, A., Colburn, D. S., Bame, S. J., & Hundhausen, A. J. 1970, *J. Geophys. Res.*, 75, 1
- Hosteaux, S., Chané, E., Decraemer, B., Talpeanu, D. C., & Poedts, S. 2018, *A&A*, 620, A57
- Hosteaux, S., Chané, E., & Poedts, S. 2019, *A&A*, 632, A89
- Hosteaux, S., Chané, E., & Poedts, S. 2021, *Geosciences*, 11, 314
- Howard, R. A., Moses, J. D., Vourlidas, A., et al. 2008, *Space Sci. Rev.*, 136, 67
- Howard, T. A. & Harrison, R. A. 2013, *Sol. Phys.*, 285, 269
- Hudson, H. S., Acton, L. W., & Freeland, S. L. 1996, *ApJ*, 470, 629
- Hundhausen, A. J., Sawyer, C. B., House, L., Illing, R. M. E., & Wagner, W. J. 1984, *J. Geophys. Res.*, 89, 2639
- Illing, R. M. E. & Hundhausen, A. J. 1985, *J. Geophys. Res.*, 90, 275
- Isavnin, A. 2016, *ApJ*, 833, 267
- Jacobs, C., Poedts, S., & van der Holst, B. 2006, *A&A*, 450, 793
- Jacobs, C., Poedts, S., Van der Holst, B., & Chané, E. 2005, *A&A*, 430, 1099
- Judge, P., Casini, R., & Paraschiv, A. R. 2021, *ApJ*, 912, 18
- Kaiser, M. L., Kucera, T. A., Davila, J. M., et al. 2008, *Space Sci. Rev.*, 136, 5
- Kallenrode, M.-B. 2004, *Space Physics: An Introduction to Plasmas and Particles in the Heliosphere and Magnetospheres* (Berlin: Springer-Verlag)

- Karpen, J. T., Antiochos, S. K., & DeVore, C. R. 2012, *ApJ*, 760, 81
- Kasran, F. A. M., Jusoh, M. H., Rahim, S. A. E. A., & Abdullah, N. 2018, in 2018 IEEE 8th International Conference on System Engineering and Technology (ICSET), 112–117
- Kay, C. & Nieves-Chinchilla, T. 2021, *Journal of Geophysical Research (Space Physics)*, 126, 2020JA028911
- Keppens, R., Meliani, Z., van Marle, A., et al. 2012, *Journal of Computational Physics*, 231, 718 , special Issue: Computational Plasma Physics
- Kilpua, E., Koskinen, H. E. J., & Pulkkinen, T. I. 2017, *Living Reviews in Solar Physics*, 14, 5
- Kilpua, E. K. J., Mierla, M., Zhukov, A. N., et al. 2014, *Sol. Phys.*, 289, 3773
- Klein, K.-L. & Dalla, S. 2017, *Space Sci. Rev.*, 212, 1107
- Ko, Y.-K., Raymond, J. C., Lin, J., et al. 2003, *ApJ*, 594, 1068
- Kojima, M. & Kakinuma, T. 1990, *Space Sci. Rev.*, 53, 173
- Kopp, R. A. & Pneuman, G. W. 1976, *Sol. Phys.*, 50, 85
- Lemen, J. R., Title, A. M., Akin, D. J., et al. 2012, *Sol. Phys.*, 275, 17
- Lepping, R. P., Acuña, M. H., Burlaga, L. F., et al. 1995, *Space Sci. Rev.*, 71, 207
- Lepping, R. P., Berdichevsky, D. B., Wu, C.-C., et al. 2006, *Annales Geophysicae*, 24, 215
- Lepping, R. P., Jones, J. A., & Burlaga, L. F. 1990, *J. Geophys. Res.*, 95, 11957
- Li, G., Jin, M., Ding, Z., et al. 2021, *ApJ*, 919, 146
- Li, T., Sun, X., Hou, Y., et al. 2022, *ApJ*, 926, L14
- Lin, J. 2004, *Sol. Phys.*, 219, 169
- Lin, J., Murphy, N. A., Shen, C., et al. 2015, *Space Sci. Rev.*, 194, 237
- Lindemann, F. A. 1919, *The London, Edinburgh, and Dublin Philosophical Magazine and Journal of Science*, 38, 669
- Linker, J. A. & Mikic, Z. 1995, *ApJ*, 438, L45
- Liu, Y. D., Hu, H., Wang, C., et al. 2016, *ApJS*, 222, 23

- Liu, Y. D., Yang, Z., Wang, R., et al. 2014, *ApJ*, 793, L41
- Loewe, C. A. & Prölss, G. W. 1997, *J. Geophys. Res.*, 102, 14209
- Longcope, D. W. & Beveridge, C. 2007, *ApJ*, 669, 621
- Low, B. C. 1977, *ApJ*, 212, 234
- Lugaz, N., Farrugia, C. J., Winslow, R. M., et al. 2017a, *ApJ*, 848, 75
- Lugaz, N., Temmer, M., Wang, Y., & Farrugia, C. J. 2017b, *Sol. Phys.*, 292, 64
- Lynch, B. J., Antiochos, S. K., Li, Y., Luhmann, J. G., & DeVore, C. R. 2009, *ApJ*, 697, 1918
- Lynch, B. J., Masson, S., Li, Y., et al. 2016, *Journal of Geophysical Research: Space Physics*, 121, 10,677
- Lyot, B. 1939, *MNRAS*, 99, 580
- Ma, S., Attrill, G. D. R., Golub, L., & Lin, J. 2010, *The Astrophysical Journal*, 722, 289
- Malherbe, J. M., Schmieder, B., Ribes, E., & Mein, P. 1983, *A&A*, 119, 197
- Manchester, Ward B., I., Vourlidas, A., Tóth, G., et al. 2008, *ApJ*, 684, 1448
- Manchester, W., Kilpua, E. K. J., Liu, Y. D., et al. 2017, *Space Sci. Rev.*, 212, 1159
- Manchester, W. I. 2007, *The Astrophysical Journal*, 666, 532
- Manchester IV, W. B., Gombosi, T. I., Roussev, I., et al. 2004, *Journal of Geophysical Research: Space Physics*, 109
- Mayaud, P. N. 1975, *J. Geophys. Res.*, 80, 111
- Mays, M. L., Taktakishvili, A., Pulkkinen, A., et al. 2015, *Sol. Phys.*, 290, 1775
- McComas, D. J., Bame, S. J., Barraclough, B. L., et al. 1998, *Geophys. Res. Lett.*, 25, 1
- McComas, D. J., Ebert, R. W., Elliott, H. A., et al. 2008, *Geophys. Res. Lett.*, 35, L18103
- McComas, D. J., Elliott, H. A., Schwadron, N. A., et al. 2003, *Geophys. Res. Lett.*, 30, 1517
- Medford, L. V., Lanzerotti, L. J., Kraus, J. S., & MacLennan, C. G. 1989, *Geophys. Res. Lett.*, 16, 1145

- Mikic, Z. & Linker, J. A. 1994, *ApJ*, 430, 898
- Milan, S. E., Clausen, L. B. N., Coxon, J. C., et al. 2017, *Space Sci. Rev.*, 206, 547
- Morrison, P. 1956, *Physical Review*, 101, 1397
- Müller, D., Marsden, R. G., St. Cyr, O. C., & Gilbert, H. R. 2013, *Sol. Phys.*, 285, 25
- Müller, D., Nicula, B., Felix, S., et al. 2017, *A&A*, 606, A10
- Neugebauer, M. 1997, *J. Geophys. Res.*, 102, 26887
- Newton, H. W. 1943, *MNRAS*, 103, 244
- Nieves-Chinchilla, T., Hidalgo, M. A., & Sequeiros, J. 2005, *Sol. Phys.*, 232, 105
- Nitta, N. V. & Mulligan, T. 2017, *Solar Physics*, 292, 125
- Nitta, N. V., Mulligan, T., Kilpua, E. K. J., et al. 2021, *Space Sci. Rev.*, 217, 82
- O'Brien, T. P. & McPherron, R. L. 2000, *J. Geophys. Res.*, 105, 7707
- Odstrčil, D. & Pizzo, V. J. 1999, *J. Geophys. Res.*, 104, 493
- Ogilvie, K. W., Chornay, D. J., Fritzenreiter, R. J., et al. 1995, *Space Sci. Rev.*, 71, 55
- Owens, M. J. 2020, *Solar-Wind Structure*
- Palmerio, E., Nieves-Chinchilla, T., Kilpua, E. K. J., et al. 2021, *Journal of Geophysical Research (Space Physics)*, 126, e2021JA029770
- Palmerio, E., Nitta, N. V., Mulligan, T., et al. 2021, *Frontiers in Astronomy and Space Sciences*, 8, 109
- Paraschiv, A. R. & Judge, P. G. 2021, in. prep
- Parker, E. N. 1955, *ApJ*, 121, 491
- Parker, E. N. 1958, *ApJ*, 128, 664
- Pesnell, W. D., Thompson, B. J., & Chamberlin, P. C. 2012, *Sol. Phys.*, 275, 3
- Pevtsov, A. A., Panasenco, O., & Martin, S. F. 2012, *Solar Physics*, 277, 185
- Piddington, J. H. 1958, *Physical Review*, 112, 589
- Plunkett, S. P., Thompson, B. J., Howard, R. A., et al. 1998, *Geophys. Res. Lett.*, 25, 2477

- Porth, O., Xia, C., Hendrix, T., Moschou, S. P., & Keppens, R. 2014, *The Astrophysical Journal Supplement Series*, 214, 4
- Priest, E. 2014, *Magnetohydrodynamics of the Sun* (Cambridge University Press)
- Pulkkinen, T. 2007, *Living Reviews in Solar Physics*, 4, 1
- Rachmeler, L. A., Platten, S. J., Bethge, C., Seaton, D. B., & Yeates, A. R. 2014, *ApJ*, 787, L3
- Richardson, I. G. & Cane, H. V. 1995, *J. Geophys. Res.*, 100, 23397
- Richardson, I. G. & Cane, H. V. 1995, *Journal of Geophysical Research: Space Physics*, 100, 23397
- Richardson, I. G. & Cane, H. V. 2004, *Journal of Geophysical Research (Space Physics)*, 109, A09104
- Richardson, I. G. & Cane, H. V. 2010, *Sol. Phys.*, 264, 189
- Richardson, I. G. & Cane, H. V. 2011, *Sol. Phys.*, 270, 609
- Rickett, B. J. & Coles, W. A. 1991, *J. Geophys. Res.*, 96, 1717
- Riley, P. & Crooker, N. U. 2004, *ApJ*, 600, 1035
- Riley, P., Linker, J. A., Mikić, Z., & Odstreil, D. 2004, *IEEE Transactions on Plasma Science*, 32, 1415
- Riley, P., Lionello, R., Mikić, Z., et al. 2007, *ApJ*, 655, 591
- Rimmele, T. R., Warner, M., Keil, S. L., et al. 2020, *Sol. Phys.*, 295, 172
- Robbrecht, E., Berghmans, D., & Van der Linden, R. A. M. 2009a, *ApJ*, 691, 1222
- Robbrecht, E., Patsourakos, S., & Vourlidas, A. 2009b, *ApJ*, 701, 283
- Ruffenach, A., Lavraud, B., Farrugia, C. J., et al. 2015, *Journal of Geophysical Research (Space Physics)*, 120, 43
- Ryan, J. M., Lockwood, J. A., & Debrunner, H. 2000, *Space Sci. Rev.*, 93, 35
- Savani, N. P., Owens, M. J., Rouillard, A. P., et al. 2011, *ApJ*, 731, 109
- Schatten, K. H., Wilcox, J. M., & Ness, N. F. 1969, *Sol. Phys.*, 6, 442
- Schmieder, B., Démoulin, P., & Aulanier, G. 2013, *Advances in Space Research*, 51, 1967

- Schou, J., Scherrer, P. H., Bush, R. I., et al. 2012, *Sol. Phys.*, 275, 229
- Schrijver, C. J., Kauristie, K., Aylward, A. D., et al. 2015, *Advances in Space Research*, 55, 2745
- Schwadron, N. A., Gorby, M., Török, T., et al. 2014, *Space Weather*, 12, 323
- Schwenn, R. 2006, *Living Reviews in Solar Physics*, 3, 2
- Seaton, D. B., Berghmans, D., Nicula, B., et al. 2013, *Sol. Phys.*, 286, 43
- Shen, F., Wang, Y., Shen, C., & Feng, X. 2017, *Sol. Phys.*, 292, 104
- Shen, F., Wu, S. T., Feng, X., & Wu, C.-C. 2012, *Journal of Geophysical Research (Space Physics)*, 117, A11101
- Smith, E. J. 2001, *J. Geophys. Res.*, 106, 15819
- Snyder, C. W., Neugebauer, M., & Rao, U. R. 1963, *J. Geophys. Res.*, 68, 6361
- Sonett, C. P., Colburn, D. S., Davis, L., Smith, E. J., & Coleman, P. J. 1964, *Phys. Rev. Lett.*, 13, 153
- Srivastava, N. & Venkatakrishnan, P. 2004, *Journal of Geophysical Research (Space Physics)*, 109, A10103
- Sterling, A. C. & Hudson, H. S. 1997, *ApJ*, 491, L55
- Stix, M. 2002, *The Sun* (Berlin: Springer-Verlag)
- Stone, E. C., Frandsen, A. M., Mewaldt, R. A., et al. 1998, *Space Sci. Rev.*, 86, 1
- Sturrock, P. A. 1966, *Nature*, 211, 695
- Sugiura, M. & Kamei, T. 1991, Office, Saint-Maur-des-Fosses, France
- Sweet, P. A. 1958, *Il Nuovo Cimento*, 8, 188
- Temerin, M. & Li, X. 2002, *Journal of Geophysical Research (Space Physics)*, 107, 1472
- Temerin, M. & Li, X. 2006, *Journal of Geophysical Research (Space Physics)*, 111, A04221
- Temmer, M. 2021, *Living Reviews in Solar Physics*, 18, 4
- Temmer, M., Veronig, A. M., Peinhart, V., & Vršnak, B. 2014, *ApJ*, 785, 85
- Temmer, M., Vršnak, B., Rollett, T., et al. 2012, *ApJ*, 749, 57

- Thalmann, J. K., Su, Y., Temmer, M., & Veronig, A. M. 2015, *ApJ*, 801, L23
- Thernisien, A. 2011, *The Astrophysical Journal Supplement Series*, 194, 33
- Thernisien, A., Vourlidas, A., & Howard, R. A. 2009, *Sol. Phys.*, 256, 111
- Thernisien, A. F. R., Howard, R. A., & Vourlidas, A. 2006, *ApJ*, 652, 763
- Thompson, B. J., Plunkett, S. P., Gurman, J. B., et al. 1998, *Geophys. Res. Lett.*, 25, 2465
- Thompson, W., Davila, J., R. Fisher, R., et al. 2003, *Proc SPIE*, 1
- Thompson, W. T. 2006a, *A&A*, 449, 791
- Thompson, W. T. 2006b, *A&A*, 449, 791
- Thompson, W. T., Kliem, B., & Török, T. 2012, *Sol. Phys.*, 276, 241
- Török, T., Panasenco, O., Titov, V. S., et al. 2011, *ApJ*, 739, L63
- Tsurutani, B. T., Gonzalez, W. D., Tang, F., Akasofu, S. I., & Smith, E. J. 1988, *Journal of Geophysical Research: Space Physics*, 93, 8519
- Ugarte-Urra, I., Warren, H. P., & Winebarger, A. R. 2007, *ApJ*, 662, 1293
- van Ballegoijen, A. A. & Martens, P. C. H. 1989, *ApJ*, 343, 971
- Van der Holst, B., Jacobs, C., & Poedts, S. 2007, *The Astrophysical Journal*, 671, L77
- van der Holst, B., Manchester, W. B., I., Frazin, R. A., et al. 2010, *ApJ*, 725, 1373
- Van der Holst, B., Poedts, S., Chané, E., et al. 2006, *Space Science Reviews*, 121, 91
- van Driel-Gesztelyi, L. & Green, L. M. 2015, *Living Reviews in Solar Physics*, 12, 1
- Vaquero, J. M. & Malville, J. M. 2014, *Mediterranean Archaeology and Archaeometry*, 14, 189
- Velli, M., Harra, L. K., Vourlidas, A., et al. 2020, *A&A*, 642, A4
- Vernazza, J. E., Avrett, E. H., & Loeser, R. 1981, *ApJS*, 45, 635
- Vourlidas, A., Colaninno, R., Nieves-Chinchilla, T., & Stenborg, G. 2011, *ApJ*, 733, L23

- Vourlidas, A., Lynch, B. J., Howard, R. A., & Li, Y. 2013, *Sol. Phys.*, 284, 179
- Wang, R., Liu, Y. D., Hoeksema, J. T., Zimovets, I. V., & Liu, Y. 2018, *ApJ*, 869, 90
- Wang, Y. M., Sheeley, N. R., Socker, D. G., Howard, R. A., & Rich, N. B. 2000, *J. Geophys. Res.*, 105, 25133
- Webb, D. F. & Cliver, E. W. 1995, *J. Geophys. Res.*, 100, 5853
- Webb, D. F. & Howard, T. A. 2012, *Living Reviews in Solar Physics*, 9, 3
- Webb, D. F., Möstl, C., Jackson, B. V., et al. 2013, *Sol. Phys.*, 285, 317
- Webb, D. F. & Vourlidas, A. 2016, *Solar Physics*, 291, 3725
- Weber, E. J. & Davis, Leverett, J. 1967, *ApJ*, 148, 217
- Wijzen, N., Samara, E., Aran, À., et al. 2021, *ApJ*, 908, L26
- Winslow, R. M., Lugaz, N., Schwadron, N. A., et al. 2016, *Journal of Geophysical Research (Space Physics)*, 121, 6092
- Wolf, R. 1848, *Nachrichten von der Sternwarte in Bern*
- Wood, B. E., Tun-Beltran, S., Kooi, J. E., Polisensky, E. J., & Nieves-Chinchilla, T. 2020, *ApJ*, 896, 99
- Wuelser, J.-P., Lemen, J. R., Tarbell, T. D., et al. 2004, in *Proc. SPIE*, Vol. 5171, *Telescopes and Instrumentation for Solar Astrophysics*, ed. S. Fineschi & M. A. Gummin, 111–122
- Xia, C., Teunissen, J., Mellah, I. E., Chané, E., & Keppens, R. 2018, *The Astrophysical Journal Supplement Series*, 234, 30
- Yashiro, S., Akiyama, S., Gopalswamy, N., & Howard, R. A. 2006, *ApJ*, 650, L143
- Yashiro, S., Gopalswamy, N., Michalek, G., et al. 2004, *Journal of Geophysical Research (Space Physics)*, 109, A07105
- Zhang, J., Dere, K. P., Howard, R. A., Kundu, M. R., & White, S. M. 2001, *ApJ*, 559, 452
- Zhang, J., Richardson, I. G., Webb, D. F., et al. 2007, *Journal of Geophysical Research (Space Physics)*, 112, A10102
- Zhang, M., Golub, L., DeLuca, E., & Burkepile, J. 2002, *ApJ*, 574, L97

- Zuccarello, F. P., Bemporad, A., Jacobs, C., et al. 2012, *ApJ*, 744, 66
- Zurbuchen, T. H., Fisk, L. A., Gloeckler, G., & von Steiger, R. 2002, *Geophys. Res. Lett.*, 29, 1352
- Zurbuchen, T. H. & Richardson, I. G. 2006, *Space Sci. Rev.*, 123, 31

Curriculum Vitae



Personal Information

Name and Surname	Dana-Camelia Talpeanu
Date of Birth	12 February 1992
Nationality	Romanian
E-mail address	dana.talpeanu@observatory.be (work) dana.talpeanu@yahoo.com (private)



Research Interests

I studied the factors contributing to the initiation and propagation of stealth coronal mass ejections (CMEs) by means of numerical simulations, but also through observations from different spacecraft. I am also interested in how they can influence the geoeffectiveness of previous eruptions during sympathetic events, and what is the contribution of the background solar wind. In parallel, I am fascinated by coronal fans and wish to study how they fit in the complete picture of the solar corona. Previously, I statistically analyzed the relationship between CMEs, interplanetary CMEs and geomagnetic storms by observational means, and performed a quantitative study on the topic.



Education

2016 - 2022	Ph.D. Centre for mathematical Plasma-Astrophysics (CmPA), KU Leuven, Belgium Solar Influences Data analysis Center (SIDC), Royal Observatory of Belgium, Belgium Dissertation: <i>"Numerical and Observational Study of Stealth and Consecutive Coronal Mass Ejections"</i> Main Supervisor: Prof. Dr. Stefaan Poedts
----------------	--

- 2014 - MS Faculty of Physics, University of Bucharest, Romania
 2016 The department of *Atomic and Nuclear Physics, Elementary Particles, Astrophysics and Applications*
 Thesis: *"Investigating Coronal Fans"*
 Supervisor: Dr. Laurel Rachmeler
- 2011 - BS Faculty of Physics, University of Bucharest, Romania
 2014 The department of *Physics*
 Thesis: *"Linking Coronal Mass Ejections - Interplanetary Coronal Mass Ejections - Geomagnetic Storms during 1996 - 2012"*
 Supervisor: Dr. Marilena Mierla

Work Experience

- Febr. 2022 Instrument Scientist at the Royal Observatory of Belgium
 - present I am currently working on a variety of topics, including detector testing and calibration, data analysis and spacecraft operations.
- 2017 International Space Science Institute (ISSI) Team led by N. Nitta & T. Mulligan
 I was a member of the ISSI team on "Understanding the Origins of Problem Geomagnetic Storms".
 Our main goal was to find out if the mechanisms and processes during the eruptions responsible for problem geomagnetic storms are distinct from those associated with more typical CMEs. The work of the team materialized in a review paper which was published in Space Science Reviews.
- Oct. 2015 - Research assistant at the Institute of Geodynamics "Sabba S.
 Oct. 2016 Stefanescu" of the Romanian Academy (IGAR)
 I worked under the supervision of Mrs. Georgeta Maris Muntean (senior researcher II) and Dr. Diana Besliu-Ionescu (senior researcher III). My responsibilities at IGAR included:
- running and developing software to analyze solar high speed streams;
 - participating in studies of strong geomagnetic storms ($Dst < -100nT$);
 - contributing with studies concerning solar jets to scientific reports submitted by my group to the leading authority - Romanian Academy.



Research Grants

- Oct. 2019 - Oct. 2021 PhD Grant (no. 1118920N) for the last 2 years from Fonds Wetenschappelijk Onderzoek – Vlaanderen (FWO), Belgium
Consists in the current, more advanced PhD work on numerical simulations of stealth and consecutive coronal mass ejections.
- Oct. 2017 - Sept. 2019 PhD Grant (no. 1118918N) for the first 2 years from Fonds Wetenschappelijk Onderzoek – Vlaanderen (FWO), Belgium
The infant PhD research work carried out during the first year at ROB was submitted for continuation and development to FWO and received funding.
- Oct. 2016 - Sept. 2017 PhD Grant (1 year) from the Royal Observatory of Belgium, Brussels, Belgium
The PhD proposal was submitted and accepted to the then newly introduced call for PhD applicants in collaboration with KU Leuven, with the project entitled “Numerical and Observational Study of Stealth Coronal Mass Ejections”.
- 13 Jul. - 12 Aug. 2015 ASBL - VZW Research Grant at the Royal Observatory of Belgium, Brussels, Belgium
I was involved in the project entitled “Investigating Coronal Fans”, under the supervision of Dr. Laurel Rachmeler. I worked on developing a program in IDL that helped me process SWAP images, magnetograms, H α and AIA images, in order to analyze coronal fans and their associations with other solar features. This project has become my master thesis.
- 5 Aug. - 3 Sept. 2013 ASBL - VZW Research Grant at the Royal Observatory of Belgium, Brussels, Belgium
I was involved in two projects, “Catalog of CMEs directed towards the Earth in the period 1996-2012” and “Linking the CMEs - ICMEs - GS (1996-2012)”, under the supervision of Dr. Marilena Mierla. I studied the relationship between coronal mass ejections, interplanetary coronal mass ejections and geomagnetic storms. This work was presented in my bachelor thesis.



Skills

Programming	C++, IDL, Linux/Ubuntu, LaTeX MPI-AMRVAC Basic knowledge of Fortran and HTML
Visualization	Tecplot, VisIt
Databases	QtiPlot, Microsoft Office and Libre Office
Languages	Romanian - Native speaker English - Advanced level French - Beginner level



Selected list of presentations

- 26 Oct. 2021 *Study of the propagation and geoeffectiveness of simulated consecutive CMEs and Interaction with the solar wind* (oral presentation)
"17th European Space Weather Week", Glasgow, UK
- 31 Jan. 2021 *Numerical Modelling of Consecutive Solar Eruptions Inserted in Different Solar Wind Speeds and Comparison of In-situ Signatures at 1AU and their Geoeffectiveness* (online pre-recorded talk)
"43rd COSPAR Scientific Assembly", Sydney, Australia
- 04 Jul. 2019 *Stealth CME Initiation and In-Situ Signatures: What Can We Learn from Modelling?* (oral presentation)
"Towards Future Research on Space Weather Drivers (FReSWeD)", San Juan, Argentina
- 29 Oct. 2018 *Initiation of Stealth CMEs: Clues from Numerical Modelling and In-Situ Comparisons* (oral presentation)
"SDO Science Workshop", Ghent, Belgium
- 26 Mar. 2018 *Numerical Modelling of Stealth Solar Eruptions; Simulated and In-Situ Signatures at 1AU* (oral presentation)
"BAMC - UK Magnetohydrodynamics Meeting", St. Andrews, United Kingdom
- 28 Nov. 2017 *Observational Analysis of Coronal Fans* (oral presentation)
PROBA2 SWT 15 meeting during "The 14th European Space Weather Week", Ostend, Belgium
- 16 Aug. 2017 *Numerical Modelling of Stealth Solar Eruptions* (oral presentation)

- "Numerical Techniques in MHD Simulations" conference and workshop, Cologne, Germany
- 29 Nov. 2016 *Investigating coronal fans* (webex presentation)
- "Coronal Fans Workshop", Madrid, Spain

Education & Public outreach activities

- Oct. 2017 - Teaching assistant for the exercise sessions of the Calculus and Analysis course at KU Leuven, taught to Bachelor students
- Sept. 2021
- 21 Sept. 2019 "Open Doors" event at the Royal Observatory of Belgium - assisted to the general organization of the event
- 29-30 Sept. 2019 "Open Doors" event at the Royal Observatory of Belgium - assisted to the general organization of the event
- 07-10 Aug. 2014 "Evaluating professor" at the Observational Exam of the International Olympiad on Astronomy and Astrophysics (IOAA), Gura Humorului, Suceava, Romania
- 2012 "School Differently (Scoala Altfel)" - contributed to the public observations and presentations about the Sun (approx. 30 minutes per group of participants) at the National Children's Palace (PNC), Bucharest, Romania
- 2011 "Big, Small, Beyond the Sun" - co-organized this event, Faculty of Physics, University of Bucharest, Romania
- 17-24 Oct. 2009 "Galilean Week" - made public telescope observations - organized by Urania Astronomical Association, Bucharest, Romania
- Mar. 2009 "Sun – Earth Days" - made public telescope observations - organized by Urania Astronomical Association, Bucharest, Romania
- 2009 "100 Hours of Astronomy" - made public telescope observations and co-organized the event at the occasion of the International Year of Astronomy 2009 - organized by Urania Astronomical Association, Bucharest, Romania
- 2009 Participated at the Cultural Institute Night, event organized by the British Council and Urania Astronomical Association, Bucharest, Romania

List of publications

1. *Prominence eruption observed in He II 304 Å up to $>6 R_{\odot}$ by EUI/FSI aboard Solar Orbiter*
Mierla, M.; Zhukov, A.N.; Berghmans, D.; Parenti, S.; Auchere, F.; Heinzel, P.; Seaton, D.B.; Palmerio, E.; Jecic, S.; Janssens, J.; Kraaikamp, E.; Nicula, B.; Long, D.M.; Hayes, L.A.; Jebaraj, I.C.; **Talpeanu, D.-C.**; et al.
Astronomy & Astrophysics Letters (accepted)
2. *Force analysis of coronal mass ejections - solar wind interactions*
Talpeanu, D.-C.; Poedts, S.; D’Huys, E.; Mierla, M.; Richardson, I.G.
Astronomy & Astrophysics (accepted)
3. *A Coronal Mass Ejection followed by a prominence eruption and a plasma blob as observed by Solar Orbiter*
Bemporad, A.; Andretta, V.; Landini, F.; Romoli, M.; Susino, R.; Mancuso, S.; Spadaro, D.; Sasso, C.; Mierla, M.; Berghmans, D.; D’Huys, E.; Zhukov, A.N.; **Talpeanu, D.-C.**; Colaninno, R.; Hess, P.; Koza, J.; Jejič, S.; Heinzel, P.
Astronomy & Astrophysics (accepted)
4. *Study of the propagation, in-situ signatures and geoeffectiveness of shear-induced coronal mass ejections in different solar winds*
Talpeanu, D.-C.; Poedts, S.; D’Huys, E.; Mierla, M.
Astronomy & Astrophysics, Volume 658, id.A56, 14 pp. (2022)
5. *The first Coronal Mass Ejection observed in both visible-light and UV Hi Ly- α channels of the Metis Coronagraph on board Solar Orbiter*
Andretta, V.; Bemporad, A.; De Leo, Y.; Jerse, G.; Landini, F.; Mierla, M.; Naletto, G.; Romoli, M.; Sasso, C.; Slemmer, A.; Spadaro, D.; Susino, R.; **Talpeanu, D.-C.**; et al.
Astronomy & Astrophysics Letters, 656, L14 (2021)

6. *Understanding the Origins of Problem Geomagnetic Storms Associated With "Stealth" Coronal Mass Ejections*
Nitta, N.V.; Mulligan, T.; Kilpua, E.K.J.; Lynch, B.J.; Mierla, M.; O'Kane, J.; Pagano, P.; Palmerio, E.; Pomoell, J.; Richardson, I.G.; Rodriguez, L.; Rouillard, A.P.; Sinha, S.; Srivastava, N.; **Talpeanu, D.-C.**; Yardley, S.L.; Zhukov, A.N.
Space Science Reviews, 217, 82 (2021)
7. *Investigation of the middle corona with SWAP and a data-driven non-potential coronal magnetic field model*
Meyer, K.A.; Mackay, D.H.; **Talpeanu, D.-C.**; Upton, L.A.; West, M.J.
Solar Physics, Volume 295, Issue 7, id.101 (2020)
8. *Numerical Simulations of Shear-Induced Consecutive Coronal Mass Ejections*
Talpeanu, D.-C.; Chané, E.; Poedts, S.; D'Huys, E.; Mierla, M.; Roussev, I.; Hosteaux, S.
Astronomy & Astrophysics, Vol. 637, A77, 10 pp. (2020)
9. *On the prediction of geoeffectiveness of CMEs during the ascending phase of SC24 using a logistic regression method*
Besliu-Ionescu, D.; **Talpeanu, D. -C.**; Mierla, M.; Muntean, G. Maris
Journal of Atmospheric and Solar-Terrestrial Physics, Volume 193, ID 105036 (2019)
10. *Ultrahigh-resolution model of a breakout CME embedded in the solar wind*
Hosteaux, S.; Chané, E.; Decraemer, B.; **Talpeanu, D. -C.**; Poedts, S.
Astronomy & Astrophysics, Vol. 620, A57, 9 pp. (2018)
11. *Coronal jet contribution to the slow Solar wind flux: preliminary results*
Paraschiv, A. R.; Dragomirescu, D.; Stan, L.; **Talpeanu, D. C.**; Ivan, C.; Radu, S.; Lacatus, D. A.; Mierla, M.
Advances in Astronomy and Space Physics, Vol. 2, p. 161-163 (2012)

FACULTY OF SCIENCE
DEPARTMENT OF MATHEMATICS
CENTRE FOR MATHEMATICAL PLASMA-ASTROPHYSICS
Celestijnenlaan 200B
B-3001 Leuven
dana.talpeanu@observatory.be

